BVRI CCD Photometry of the Peculiar Galaxies NGC 5605 and NGC 5665

B. P. Artamonov[1], Yu. Yu. Badan[1], and A. S. Gusev[1, 2]

[1]*Sternberg Astronomical Institute, Universitetskii pr. 13, Moscow, 119899 Russia*
[2]*Institute of Solid-State Physics, Russian Academy of Sciences, Chernogolovka, Moscow oblast, 142432 Russia*

Received September 6, 1999

Abstract—The paper presents the results of *BVRI* CCD photometry of the late-type peculiar galaxies NGC 5605 and NGC 5665 obtained on the 1.5-m telescope of the Maĭdanak Observatory (Uzbekistan). Regions of star formation are identified and studied. The compositions of the stellar populations in various regions of NGC 5605 and NGC 5665 are estimated using two-color diagrams. The ages of blue condensations (stellar aggregates) in the spiral arms of the galaxies are determined. It is concluded that NGC 5665 underwent an interaction with another galaxy 5×10^8 yr ago. © *2000 MAIK "Nauka/Interperiodica"*.

1. GENERAL INFORMATION

The problems of galactic evolution are closely related to studies of the composition of stellar populations. Investigations of peculiar galaxies, in which the processes of star formation occur more vigorously than in ordinary galaxies, are of special interest. Young objects can form unusual spatial structures in their galaxy.

We set ourselves the task of investigating the photometric properties of the peculiar galaxies NGC 5605 and NGC 5665. In particular, we were interested in the stellar populations in various regions of the galaxies and in determining the parameters of star-formation regions in the galactic disks. This could shed light on the origins of the distorted shapes of these two galaxies. NGC 5605 (Fig. 1a) and NGC 5665 (Fig. 1b) are relatively poorly studied peculiar galaxies with complex morphologies, having local regions of enhanced brightness and signs of a bar. The main characteristics of the galaxies are presented in Table 1.

NGC 5605. *BV* surface photometry was conducted by Gamal el din *et al.* [2, 3], who determined the integrated photometric parameters of the galaxy (color, luminosity, inclination, position angle) and noted the complex dependence of the elliptical isophotes on distance from the galactic center. *BV* aperture photometry was carried out by Peterson [4] using fairly large (relative to the size of NGC 5605) apertures; the resulting integrated $B - V$ value differs from that of [2, 3] by 0.15^m (0.69^m as compared to 0.55^m).

Observations at 12–100 μm [5] do not reveal signs of activity in NGC 5605 and show it to be a relatively "quiet" galaxy at infrared wavelengths. According to the classification scheme of [6], the nucleus of NGC 5605 has type CB: there is a small disk or bulge at the center of the galaxy (i.e., the nucleus is not starlike). According to 21-cm observations, the mass of neutral hydrogen in NGC 5605 is $3.4 \times 10^9\ M_\odot$ [7].

NGC 5665. The morphological type of this galaxy remains unclear: various researchers have classified it as Sa/Sc, Sc, SABc, Sc pec, SABc pec, and even SBm pec [8–13]. According to the spiral-branch classification proposed in [14], NGC 5665 is a type IV galaxy: it has a single main spiral and fragments of several other branches. NGC 5665 is included in the catalog of peculiar galaxies of Arp (Arp 49) and in the catalog of interacting galaxies of Vorontsov–Vel'yaminov (VV 412).

Surface photometry has been carried out in the *R* [15], *H* [13], and *K* [13] filters. The data of [13] suggest the possible presence of a small bar (with radius 7″) oriented along the major axis of NGC 5665. Numerous infrared studies have been carried out at 10–100 μm [5, 8–10, 16]. According to its IR properties, NGC 5665 is a normal galaxy with signs of outbursts of star formation [16]. The radio data of [17] at 4.85 GHz also suggest the presence of powerful bursts of star formation. Giuricin *et al.* [9] classify NGC 5665 as an interacting galaxy. At the same time, NGC 5665 is not a

Table 1. Main characteristics of the galaxies

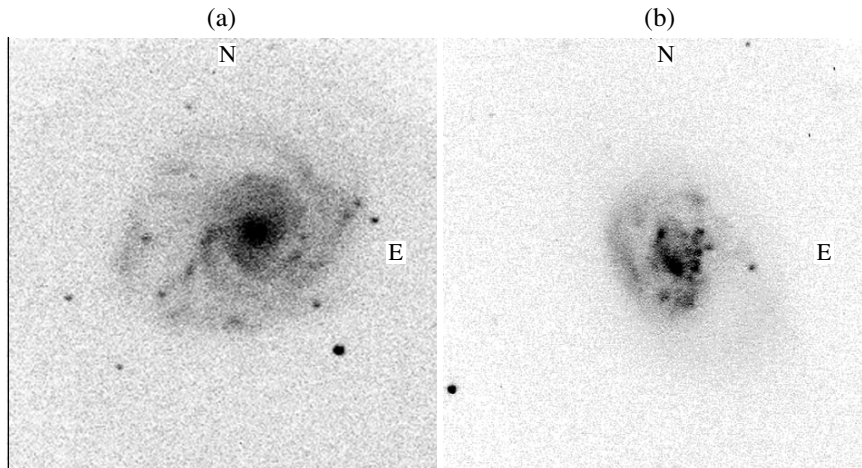| Characteristics	NGC 5605	NGC 5665
Type	SABcp [1]	SABcp [1]
m_B	12.53 [1]	12.50 [1]
$M_B^{0,\,i}$	–20.72	–20.10
V_0, km/s	3363 [1]	2271 [1]
R, Mpc ($H_0 = 75$ km/s Mpc)	44.8	32.8
D_{25}, arcmin	1.74 [1]	1.9 [1]
d_{25}, kpc	22.4	18.7
Inclination, deg	33.5 [1]	44.5 [1]
Position angle, deg	74 [2,3]	145 [1]

Fig. 1. CCD image of (a) NGC 5605 and (b) NGC 5665 in the *V* filter. The size of the image is $2.1' \times 2.1'$.

member of the Virgo cluster of galaxies [11] and is not perturbed by any nearby companions [18].

Spectroscopic observations of the central region of NGC 5665 at 4700–7100 Å [19] indicate that the galaxy occupies an intermediate position between LINERs (i.e., galaxies having a region of low-ionization nuclear emission) and galaxies with an abundance of HII regions (i.e., having a large number of young, hot stars). The nuclear emission type of NGC 5665 is 3.5. The galaxy is rich in gas and dust: for the total mass of NGC 5665 of $6 \times 10^{10}\ M_\odot$ derived in [12] based on 21-cm line observations, the mass of HI is about $1 \times 10^9\ M_\odot$ [10–12, 20] and the mass of dust is $M_{\mathrm{dust}} = 1.4 \times 10^7\ M_\odot$ [10].

2. OBSERVATIONS AND REDUCTION

Our observations of the two galaxies were carried out on July 6 and 7, 1997, on the 1.5-m telescope of the Sternberg Astronomical Institute (focal length 12 m) of the Maĭdanak Observatory (Uzbekistan), using the Pittsburgh University TI-800 CCD camera. The CCD camera had characteristics standard for its class. The size of the field imaged (for the 12-m focus) was 3.6′. The camera was liquid-nitrogen cooled.

Together with the receiver system, the filters used formed bands close to those of the Johnson–Cousins *BVRI* system. Information about the filters is published in [21].

We obtained CCD images of NGC 5605 and NGC 5665 in the *B*, *V*, *R*, and *I* bands (two images of each galaxy in each filter). The exposures for the *V*, *R*, and *I* filters were 2 min; the exposures for the *B* filter were 3 min, except for the second image of NGC 5605, for which the exposure was 4 min. The scale of the images during the observations was 0.25″/pixel, and the seeing was 0.7″–0.9″.

Subsequent reduction of the data was carried out on a personal computer at the Sternberg Astronomical Institute using standard procedures in the ESO–MIDAS and IRAF packages. The main stages of data reduction included:

(a) correction of the data for the amplification shift of the array and the flat field;

(b) subtraction of the sky background from each image;

(c) superposition of the galaxy images using reference stars;

(d) merging of images made in the same filters;

(e) translation of the measurements to a logarithmic scale (mag/arcsec^2);

(f) translation of the measurements from the instrumental system to the Johnson–Cousins system in accordance with color equations derived earlier in [21, 22].

The photometric ties in the *B*, *V*, *R*, and *I* filters were based on the Landolt standard stars SA110 and PG1657 + 078 [23]. The accuracy of the photometric tie was 0.07^m.

To construct the two-color diagrams, we corrected the data for Galactic absorption using the standard procedure adopted in the RC3 catalog [1]. Corrected quantities are denoted with a subscript "0."

Taking into account the known distances to the galaxies, the scales of the images were 54 pc/pixel for NGC 5605 and 36 pc/pixel for NGC 5665.

3. ANALYSIS OF RESULTS

3.1. Photometric Profiles and Morphologies of the Galaxies

NGC 5605. Figures 2a and 2b present *B*, *V*, *R*, and *I* photometric sections along the major axis of NGC 5605 (position angle 57°) passing through the galaxy's center; Figure 2c shows an isophote map in the *R* filter. The galaxy has a nucleus 1.7 kpc (8″) in diameter, which makes a smooth transition to the bulge (Figs. 2a, 2b). The diameter of the bulge is about 3 kpc (14″). At large dis-

tances from the center, the emission is dominated by the contribution of the disk.

The photometric nucleus and bulge are poorly distinguished: the photometric profile of the nucleus resembles that of the bulge, as was also noted in [6]. The maximum surface brightness at the center of the nucleus (m_B/arcsec^2 = 20.0, m_R/arcsec^2 = 18.4) is lower than the standard brightness for the nuclei of normal galaxies. This also indicates that the photometric characteristics of the nucleus of NGC 5605 are not starlike.

In the inner part of the disk, there is a nearly rectangular region 5.4×4.1 kpc ($25'' \times 19''$) in size, resembling a very short bar (Fig. 2c). The mean surface brightness of this region is constant along its major axis and is 21.4 ± 0.1 m_V/arcsec^2; this value is typical of bars [24].

NGC 5605 is characterized by a rather unusual spiral pattern: the spiral arms come out from the bar at its eastern and southern ends. Each of the arms divides into two branches about 4 kpc ($18''$) from the center of the galaxy: one long and tightly wound and the other short and loosely wound. One or two weak spiral arms also come out of the northern end of the bar. We cannot say anything definite about the emergence of the branches from the eastern part of the bar: if a weak spiral also comes out of this region, it is superposed with the bright arm coming out of the southern part of the bar (Fig. 2c). The branches are wound into a ring 12 kpc ($55''$) in diameter; the center of the ring is shifted toward the west by 1.2 kpc ($5''$) relative to the center (nucleus) of NGC 5605 (Fig. 1a).

The unusual dependence for the ellipticity and position angle of the isophotes on distance from the center is of special interest (Figs. 3a, 3b). The circum-nuclear region has nearly circular isophotes ($e = 0.05 \pm 0.02$) oriented in position angle $75° \pm 4°$. The short bar ($e = 0.13 \pm 0.01$) is elongated in position angle $30°–40°$. The bright, short branches emanating from the bar "turn" the galaxy $50°$ toward the east: the position angle 3.3 kpc ($15''$) from the center is $95° \pm 5°$. Further variations in the position angle (and, in part, the ellipticity) of the isophotes are associated with the fact that the center of the bright ring does not coincide with the center of the galaxy's nucleus. At distances $r > 30''$ from the center, the position angle of the isophotes is $76° \pm 2°$, and their ellipticity is 0.34 ± 0.04, increasing from the *B* to *I* images.

The eastern part of the galaxy is brighter than the western part by 0.6^m/arcsec^2 in the *V* band (21.4 ± 0.1^m/arcsec^2 as opposed to 22.0 ± 0.1^m/arcsec^2). The size of the galaxy within the 22.5^m/arcsec^2 isophotes in the *R* band is 19×16 kpc ($88'' \times 74''$).

NGC 5665. Figures 4a and 4b present *B*, *V*, *R*, and *I* photometric sections along the major axis of NGC 5665 (position angle $138°$) passing through the galaxy's center; Figure 4c presents an *R* isophote map. The galaxy is distinguished by the asymmetry of its central region along the major axis. Examining the variations of the surface brightness along the major axis toward
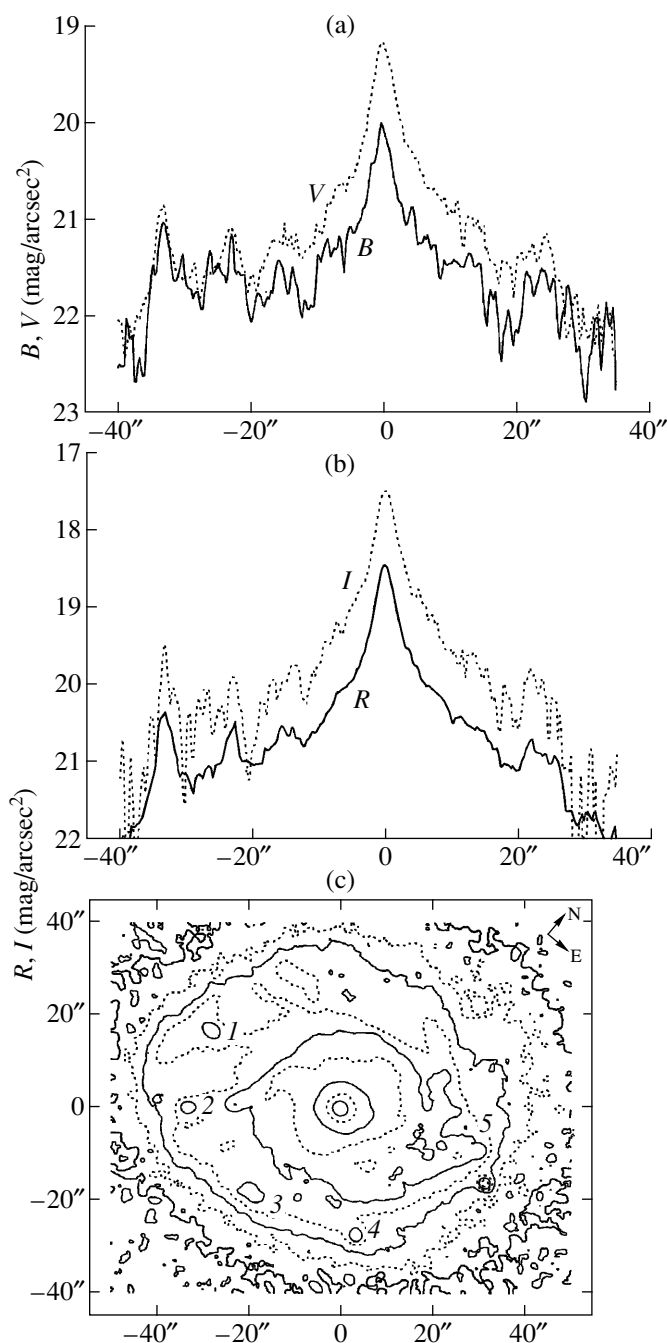
Fig. 2. Photometric profiles (mag/arcsec^2) along the major axis of NGC 5605 in the (a) *B* (solid) and *V* (dotted) and (b) *R* (solid) and *I* (dotted) filters. Panel (c) shows a contour image of the galaxy in the *R* filter (the isophotes are 19.0, 19.5, 20.0, 20.5, 21.0, 21.5, 22.0, 22.5, and 23.0). The numbers in panel (c) identify various stellar aggregates.

the southeast from the center, we can make out a starlike nucleus with radius 0.43 kpc ($3''$) and a short bar with radius 0.85 kpc ($6''$), with an exponential brightness decrease along the major axis (with $\alpha^{-1} = 1.7$ kpc). The surface brightness of the bar is m_V/arcsec^2 = 20.0 ± 0.2. The radius of the nucleus along the galaxy's
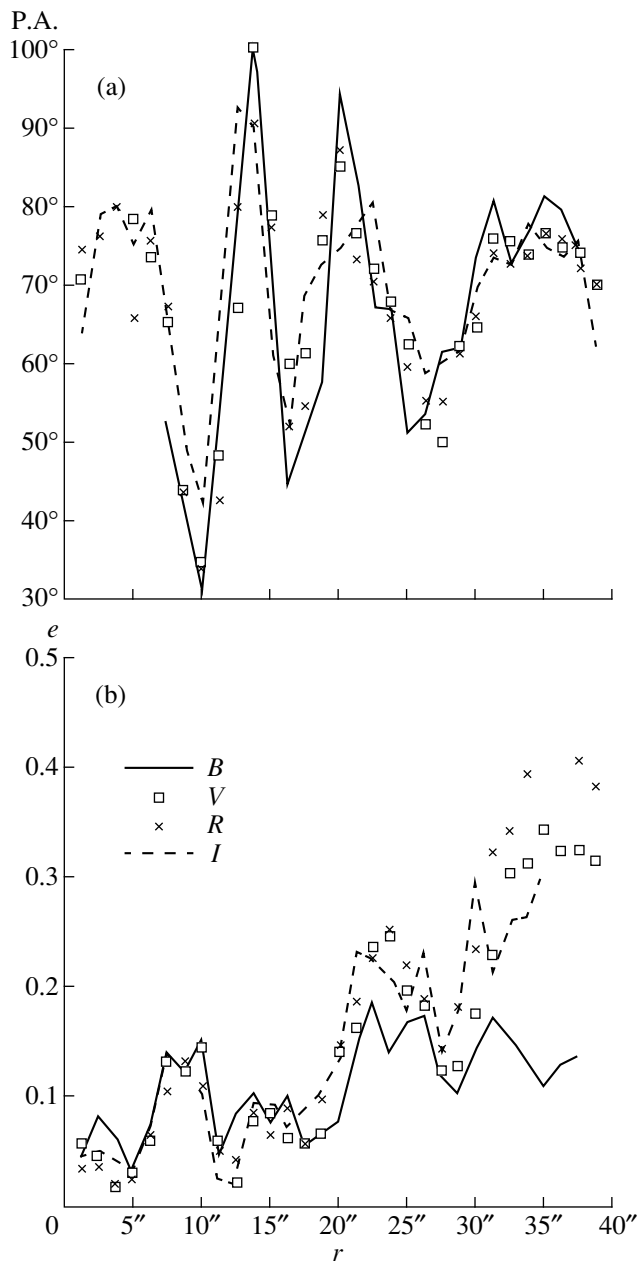
Fig. 3. Dependence of (a) position angle and (b) isophote ellipticity $e = 1 - b/a$ on distance r from the center of NGC 5605 in the B (solid), V (squares), R (asterisks), and I (dashed) filters.

Fig. 4. Same as Fig. 2 for NGC 5665.

minor axis is also 0.43 kpc (3″; Fig. 4c). However, photometric profiles along the major axis toward the northwest from the center provide a somewhat different picture (see the left panels of Figs. 4a, 4b): the brightness fall-off within 3″ of the center corresponds not to a starlike nucleus but to a bulge. The asymmetry of the brightness distribution in the nuclear region of NGC 5665 is most clearly visible in the bluest filters (B and V). We can distinguish a bar (its northwest part) 0.58– 1.15 kpc (4″–8″) from the center of the galaxy, whose
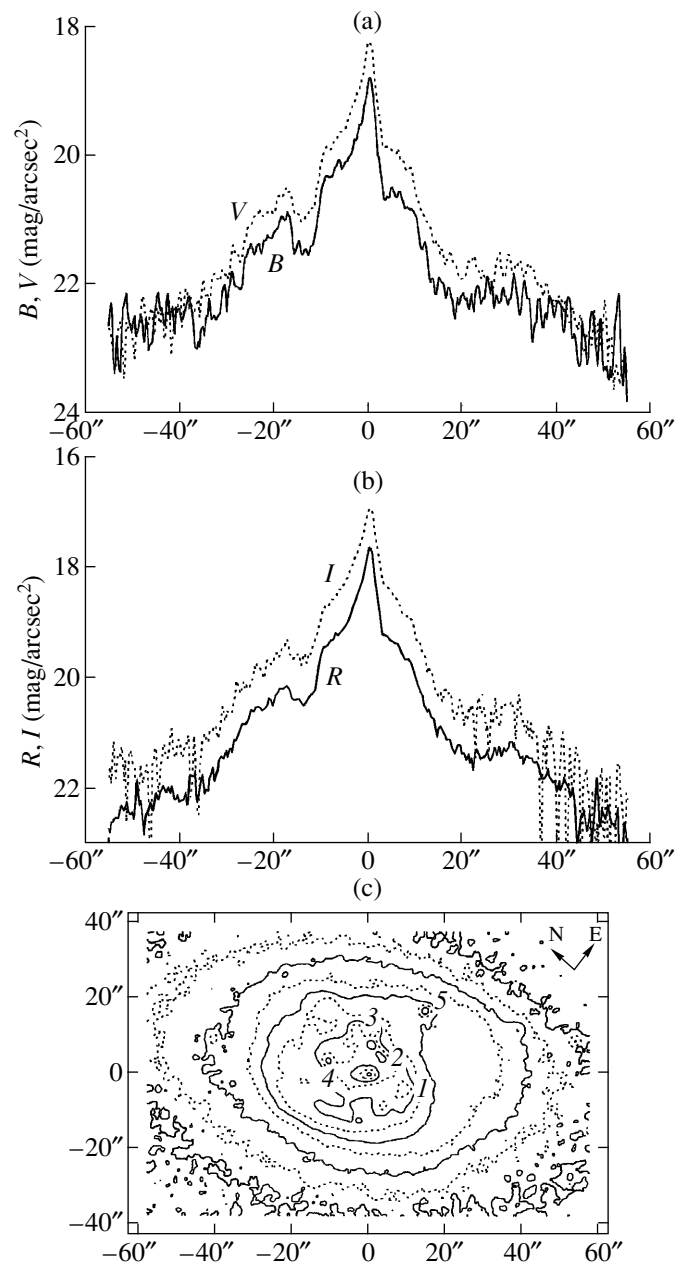
R and I photometric parameters are similar to those of the southeast part of the bar.

The asymmetry of the photometric profiles in the inner regions of NGC 5665 (where the main contribution to the emission is made by the disk) is due to the fact that the sections along the major axis intersect the galaxy's spiral arms. The spiral arms are placed asymmetrically relative to the center of the galaxy and have different surface brightnesses.

The spiral pattern of NGC 5665 is extremely interesting (Figs. 1b, 4c): in addition to the two spiral branches emanating from the ends of the bar, we can see a bright, straight arm going from south to north, passing through the southeastern end of the bar. Several regions of enhanced brightness are observed in this straight arm, 250–400 pc (2″–3″) in size and with surface brightness reaching 19.1 ± 0.1^m/arcsec^2 in the V band. The surface brightness of the spiral arms is lower—on average, $21.0 \pm 0.15\ m_V$/arcsec^2 and reaching $19.8 \pm 0.05\ m_V$/arcsec^2 only in isolated places.

The position angle of NGC 5665 is $147° \pm 2°$, and the ellipticity of the isophotes is $e = 0.38 \pm 0.03$ (Figs. 5a, 5b). Based on the variation of the position angle and isophote ellipticity with distance from the galactic center, we can distinguish three regions: the central region (P.A. $= 120° \pm 16°$, $e = 0.20 \pm 0.04$), the inner-disk region (P.A. $= 2° \pm 2°$, e varies from 0.42 in the B image to 0.34 in the I image), and the outer region. The size of NGC 5665 within the 22.5^m/arcsec^2 R isophotes is 15.5×9.2 kpc ($107″ \times 64″$).

3.2. Color Indices

The data presented in this section have not been corrected for Galactic and internal absorption. However, we have calculated corrections associated with Galactic absorption (E) and the reduction of the galaxy to a "face-on" position ($E(i)$), calculated from RC3 data listed in Table 2.

NGC 5605. Figure 6a shows the $B - V$, $V - R$, and $R - I$ color indices along the major axis of NGC 5605, while Figures 6b–6d show color-index maps. On the whole, the galaxy becomes bluer with distance from the center, most strongly in $B - V$ (Fig. 6a). $B - V$ varies from $1.15^m \pm 0.02^m$ in the nucleus to $0.4^m \pm 0.2^m$ at the periphery of the galaxy; the corresponding indices for $V - R$ are $0.65^m \pm 0.05^m$ and $0.3^m \pm 0.2^m$ and for $R - I$ are $0.7^m \pm 0.05^m$ and $0.3^m \pm 0.4^m$, respectively.

The color indices in the bar are $B - V = 0.85^m \pm 0.15^m$, $V - R = 0.55^m \pm 0.08^m$, and $R - I = 0.65^m \pm 0.10^m$. The eastern part of the galaxy is somewhat redder than the western part. $B - V$, $V - R$, and $R - I$ in the eastern part of the disk are $0.6^m \pm 0.3^m$, $0.5^m \pm 0.1^m$, and $0.4^m \pm 0.3^m$, while, in the western part of the disk, they are $0.5^m \pm 0.3^m$, $0.4^m \pm 0.2^m$, and $0.3^m \pm 0.1^m$, respectively.

NGC 5665. Figure 7a shows the $B - V$, $V - R$, and $R - I$ color indices along the major axis of NGC 5665, while Figures 7b–7d show color-index maps. The variation of the color indices along the major axis is weak (Fig. 7a). With distance from the center, the galaxy becomes bluer in $B - V$ and $V - R$: $B - V$ varies from $0.85^m \pm 0.10^m$ in the central region to $0.55^m \pm 0.25^m$ at its periphery, and $V - R$ varies from $0.55^m \pm 0.03^m$ to $0.4^m \pm 0.15^m$ from the center to the periphery. $R - I$ remains constant along the major axis and is equal to $0.55^m \pm 0.15^m$. In the southeastern end of the bar, $B - V = 0.8^m \pm 0.1^m$, $V - R = 0.5^m \pm 0.02^m$, and $R - I = 0.6^m \pm$
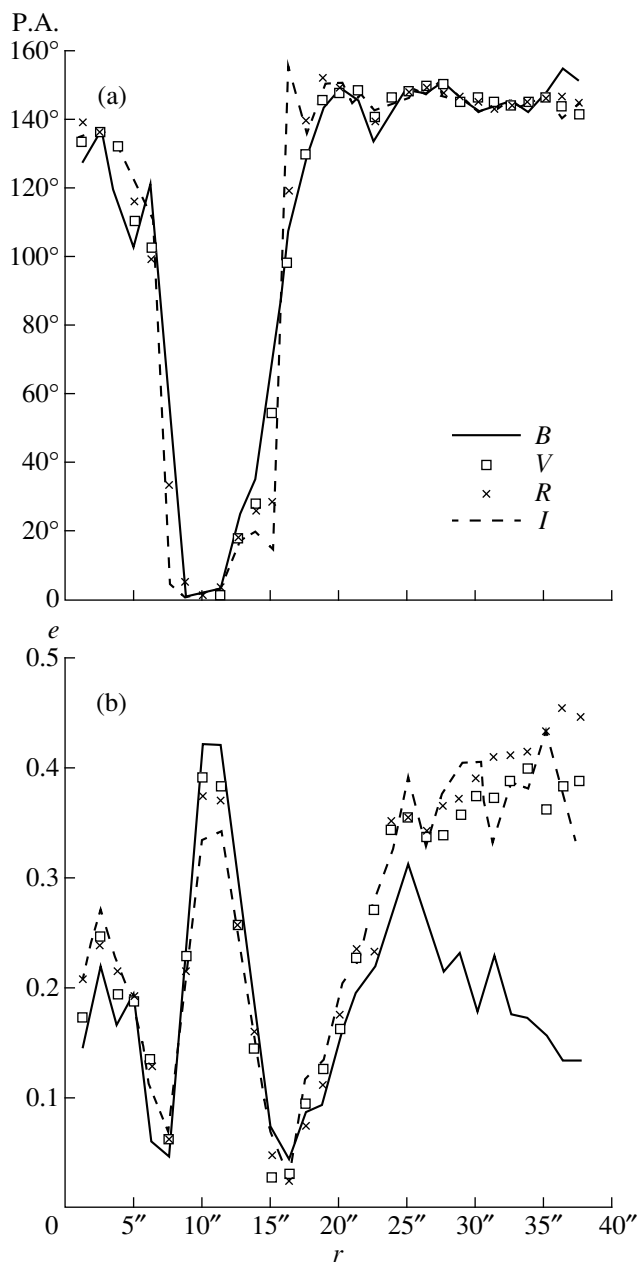

Fig. 5. Same as Fig. 3 for NGC 5665.

0.05^m; and in the northwestern end of the bar, $B - V = 0.75^m \pm 0.03^m$, $V - R = 0.5^m \pm 0.05^m$, and $R - I = 0.55^m \pm 0.05^m$.

Overall, the distribution of colors in NGC 5665 is fairly ordinary: a red central region, blue disk between spiral arms, and still bluer spiral branches (in the branches, $B - V = 0.6^m \pm 0.1^m$, $V - R = 0.4^m \pm 0.1^m$, $R - I = 0.5^m \pm 0.1^m$). The only exception is the color distribution in the central part of NGC 5665: the region to the southeast of the nucleus is redder than the region to the northwest of the nucleus and is the reddest region in the galaxy (Figs. 7b–7d).
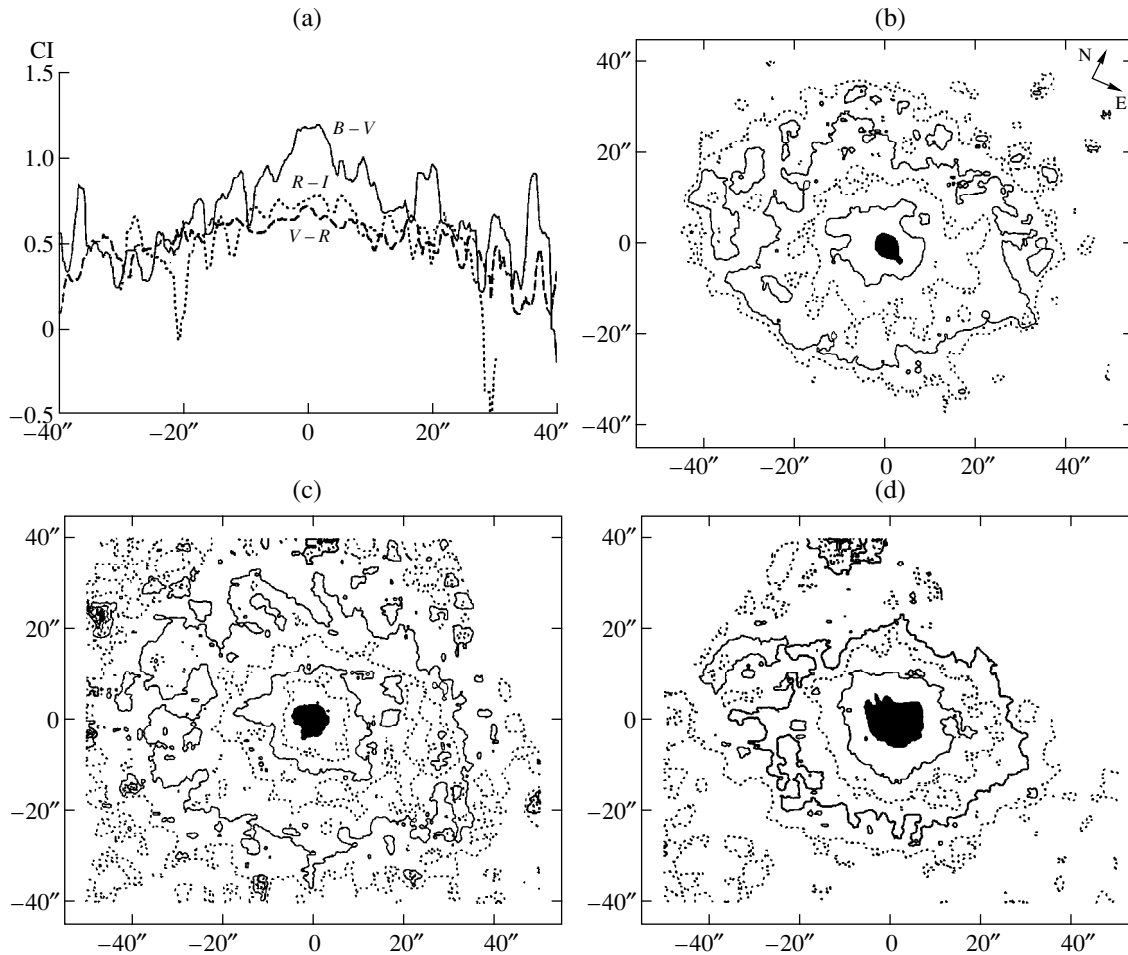
Fig. 6. (a) $B - V$ (solid), $V - R$ (dashed), and $R - I$ (dotted) color indices along the major axis of NGC 5605 and maps of (b) $B - V$, (c) $V - R$, and (d) $R - I$. The $B - V$ contours are at 0.3, 0.5, 0.7, 0.9, and 1.1, with the region with $B - V > 1.1$ shaded; the $V - R$ contours are at 0.2, 0.4, 0.5, 0.55, 0.6, and 0.65, with the region with $V - R > 0.65$ shaded. The $R - I$ contours are 0.0, 0.3, 0.5, 0.6, and 0.7, with the region with $R - I > 0.7$ shaded.

3.3. Two-Color Diagrams

NGC 5605. Figures 8a and 8b show $(B - V)_0$–$(V - R)_0$ and $(B - V)_0$–$(V - I)_0$ two-color diagrams with all data corrected for Galactic absorption using the method proposed in RC3. The numbers in the figure indicate the colors of the (*1*) nucleus, (*2*) bulge, (*3*) disk (outside spiral branches), (*4*) spiral branches, and (*5, 6*) bar at distances 1.7 and 2.6 kpc (8″ and 12″, respectively) from

Table 2. Taking account of Galactic and internal absorption of the galaxies

Galaxy	$E(B - V)$	$E(V - R)$	$E(R - I)$
	$E_{B - V}(i)$	$E_{V - R}(i)$	$E_{R - I}(i)$
NGC 5605	0.07	0.07	0.06
	0.025	0.025	0.02
NGC 5665	0.01	0.01	0.01
	0.045	0.045	0.04

the nucleus. The squares mark the colors of five regions of enhanced brightness.

The averaging errors are $\Delta(B - V)_0 = 0.12^m$, $\Delta(V - R)_0 = 0.05^m$, and $\Delta(V - I)_0 = 0.14^m$. Most of the points in the two-color diagrams lie along the normal color sequence (NCS) for galaxies, testifying to the quiet character of the star formation in NGC 5605. An exception is certain regions of the disk and spiral branches: points *3* and *4* in Fig. 8a are shifted from the NCS. These bursts of star formation in the spiral branches and disk (between the spiral branches) are roughly equally powerful: points *3* and *4* occupy equivalent positions in the two-color diagrams within the errors. Regions of enhanced brightness in the spiral branches are not distinguished from the disk in terms of their color indices either. The characteristic size of these regions—sites of star formation—is about 450 pc (2″), corresponding to the size of stellar aggregates according to the classification of star-formation regions of Efremov [26]. Judging from its color indices, the brightest region of enhanced brightness, to the east of the center of
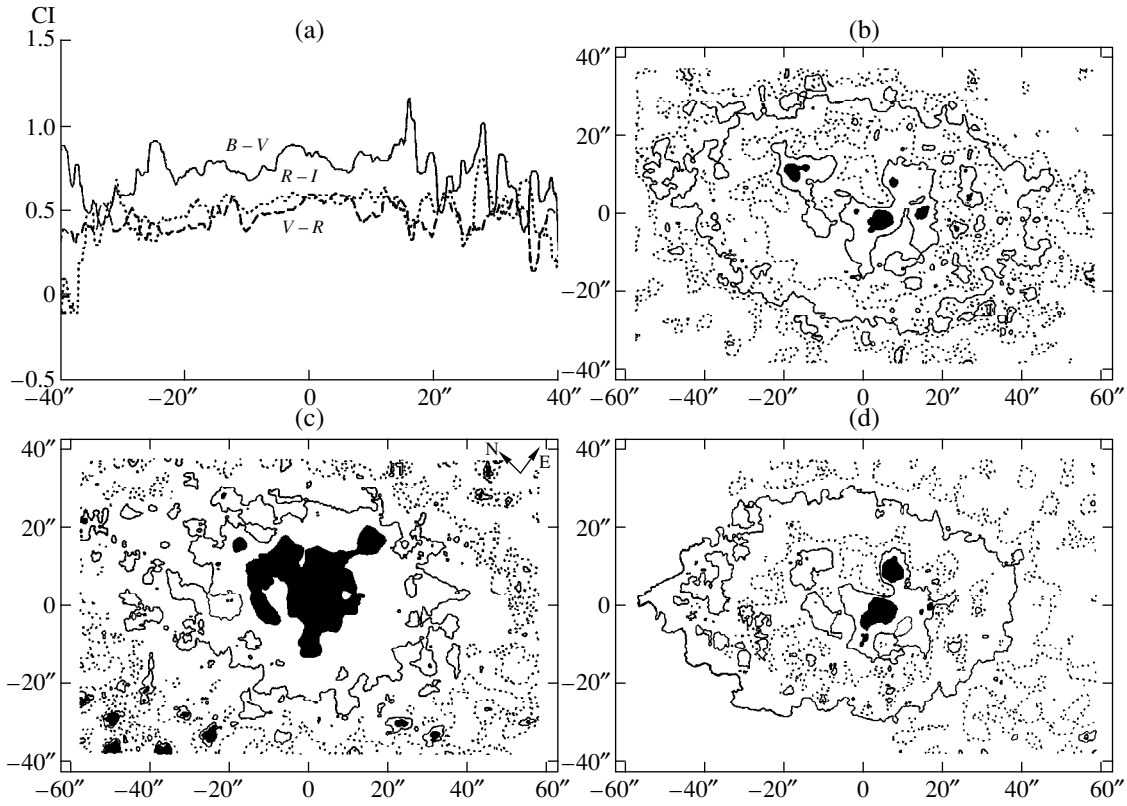
Fig. 7. (a) $B - V$ (solid), $V - R$ (dashed), and $R - I$ (dotted) color indices along the major axis of NGC 5665 and maps of (b) $B - V$, (c) $V - R$, and (d) $R - I$. The $B - V$ contours are at 0.3, 0.5, 0.7, 0.8, and 0.9, with the region with $B - V > 0.9$ shaded; the $V - R$ contours are at 0.2, 0.4, and 0.5, with the region with $V - R > 0.5$ shaded. The $R - I$ contours are 0.0, 0.3, 0.5, 0.55, and 0.6, with the region with $R - I > 0.6$ shaded.
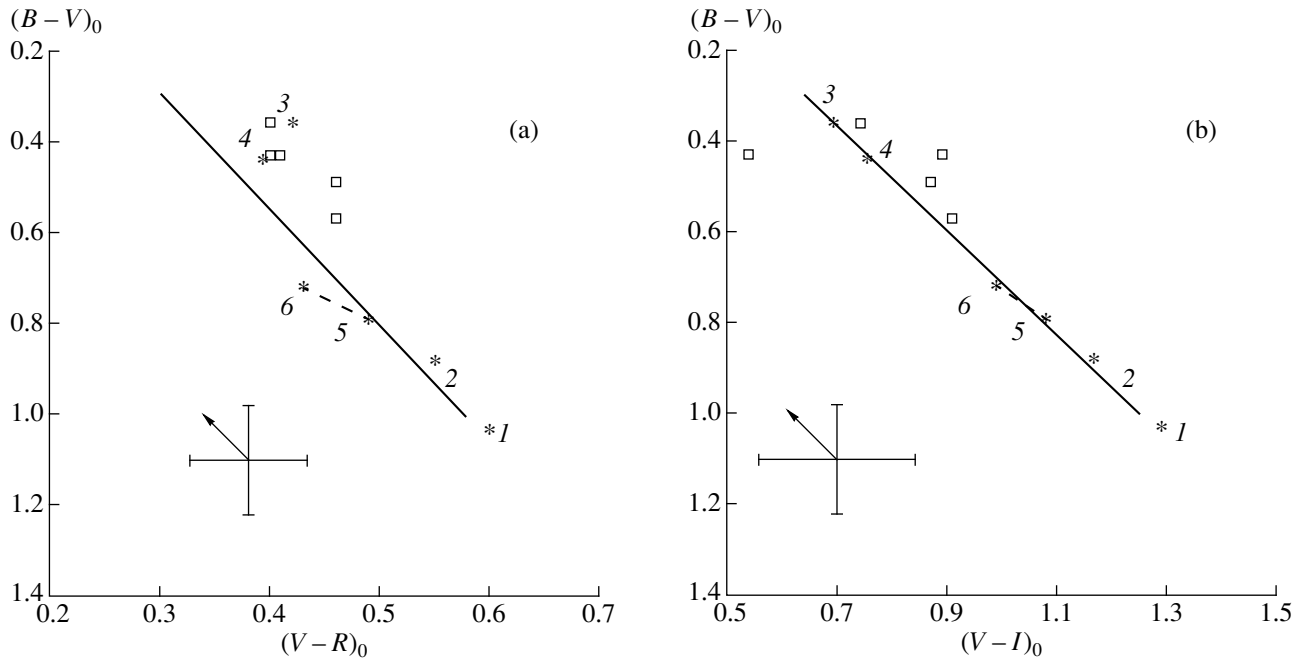

Fig. 8. (a) $(B - V)_0$–$(V - R)_0$ and (b) $(B - V)_0$–$(V - I)_0$ two-color diagrams for NGC 5605. The straight line shows the normal color sequence for galaxies from [25]. The measurement errors are indicated. The arrows show how points are shifted if internal absorption is taken into account. For other notation, see the text.
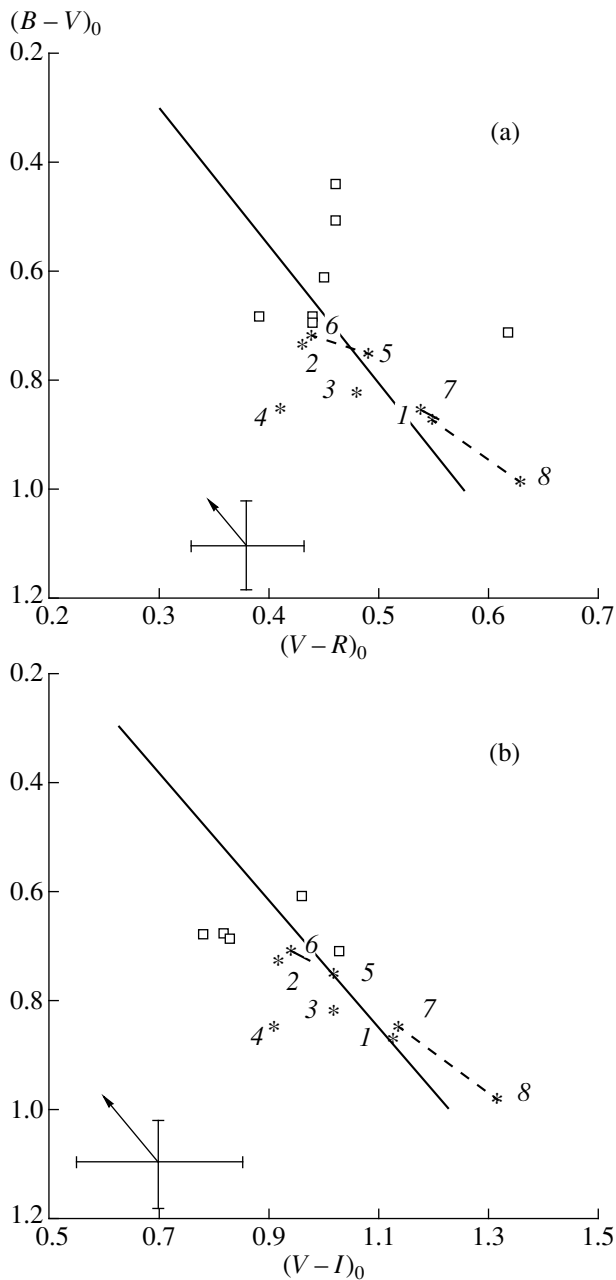
Fig. 9. Same as Fig. 8 for NGC 5665.

NGC 5665. Figures 9a and 9b show $(B - V)_0$–$(V - R)_0$ and $(B - V)_0$–$(V - I)_0$ two-color diagrams with all data corrected for Galactic absorption using the method proposed in RC3. The numbers in the figure indicate the colors of the (*1*) nucleus, (*2*) northeast spiral branch, (*3*) disk, (*4*) southwest spiral branch, (*5, 6*) northwest part of the bar at distances 5.0 and 8.5 kpc (3.5″ and 6″, respectively) from the center, and (*7, 8*) southeast part of the bar at distances 8.5 and 11.5 kpc (6″ and 8″, respectively) from the center. The squares mark the colors of five regions of enhanced brightness.

The averaging errors are $\Delta(B - V)_0 = 0.08^m$, $\Delta(V - R)_0 = 0.05^m$, and $\Delta(V - I)_0 = 0.15^m$. The points for the color indices in the central regions of NGC 5665 (the nucleus and bar) lie along the NCS, indicating that the stellar populations in these regions are standard. The positions of points *2* and *3* characterizing the northern and eastern parts of the disk (including spiral branches) correspond to a young stellar population with an age on the order of 5×10^9 yr. The color of the southwestern spiral branch (point *4*) indicates a still younger stellar component. All these factors, and also the peculiar morphology of the galaxy, suggest that NGC 5665 may have undergone a strong interaction with other galaxies in the past. The reddest region of NGC 5665 is the beginning of the visible southeastern part of the bar. The difference in the positions of the southeastern and northwestern parts of the bar in the two-color diagrams could be associated with differences in absorption by dust in these regions.

The regions of enhanced brightness in the spiral branches are the bluest regions in NGC 5665. The deviation of these regions from the NCS in the two-color diagrams (Figs. 9a, 9b) suggests the presence of outbursts of star formation. According to the classification of Efremov [26], the characteristic sizes of these sites of star formation (see Section 3.1) correspond to those of young stellar aggregates visible against the background of a relatively old disk population. We found the star-formation rate calculated using IR data to be 5.8 ± 0.4 $M_\odot$/yr, with a high star-formation efficiency of 3.9×10^{-9} yr^{-1}.

3.4. Sites of Star Formation

Using the simulations of the color indices of stellar systems obtained in [22, 24], we determined the ages of the brightest sites of star formation/stellar aggregates in NGC 5605 and NGC 5665. In all, we studied ten such sites, five in each galaxy (Figs. 2c, 4c). Table 3 presents the main characteristics of the stellar aggregates. In contrast to the previous section and Figs. 8a, 8b, 9a, and 9b, we consider here "intrinsic" colors. We obtained the "intrinsic" intensities of the stellar aggregates by subtracting the background intensity of the spiral branches from the integrated intensity of the regions occupied by the aggregates. The first column of Table 3 gives the name of the galaxy, the second numbers identifying the aggregates, and the third to the fifth $(B - V)_{0, i}$, $(V - R)_{0, i}$, and $(V - I)_{0, i}$ color indices corrected for Galactic

the galaxy (Fig. 2c), is a late F–early G star projected onto this area (the star is not shown on the two-color diagrams).

We found the star-formation rate calculated using the IR observations of [5] to be 3.3 ± 0.2 $M_\odot$/yr and the upper limit to the star-formation efficiency to be 1×10^{-9} yr^{-1}. It is not possible to accurately determine the star-formation efficiency, since data on the mass of H_2 in the galaxy are lacking. Thus, in spite of its standard optical and IR characteristics for its morphological type, NGC 5605 is an example of a galaxy that has undergone bursts of star formation in its disk.

absorption and internal absorption due to the inclination of the galaxy. The sixth column presents the characteristic sizes of the stellar aggregates (in pc), the seventh column gives the ages of the aggregates derived from the $(B-V)_0$–$(V-R)_0$ and $(B-V)_0$–$(V-I)_0$ two-color diagrams using the data of [24]. Note that taking into account possible additional internal absorption in the disk (not associated with the galaxy's inclination) could decrease the age of the aggregates, so that the ages in Table 3 should be considered upper limits.

The characteristic distance between the stellar aggregates in NGC 5605, taking into consideration the inclination of the disk, is 6.0 ± 0.5 kpc. The uniform distribution of the aggregates along the spiral branches is in good agreement with the theory of [26]: when protocomplexes form in the gaseous disk of a galaxy under the action of large-scale gravitational instability, the instability in the rotating gaseous disk, and especially in the spiral arms, develops most rapidly for perturbations with certain wavelengths. These wavelengths correspond to the characteristic distances between neighboring complexes (aggregates).

The stellar aggregates in NGC 5665 all have essentially the same age (except for aggregate *3*). This provides evidence for a powerful simultaneous burst of star formation in this galaxy 5×10^8 yrs ago.

4. DISCUSSION

NGC 5605. According to its photometric characteristics, this is a completely ordinary object: the central region is populated with old stars, and evidence of weak bursts of star formation is observed in the disk and spiral branches of the galaxy. The youngest regions in NGC 5605 are sites of star formation with diameters of about 450 pc—stellar aggregates with ages on the order of 10^8–10^9 yrs. The peculiarity of the galaxy is manifest only in its morphology: an asymmetric ring and the absence of a starlike nucleus. Further studies of the galaxy are required—first and foremost a map of the radial-velocity distribution. This will make it possible to determine the origin of the complex, nonstandard morphological structure of NGC 5605.

NGC 5665. A whole series of facts indicates that NGC 5665 is undergoing interaction. Its one-armed shape makes NGC 5665 resemble galaxies such as the LMC. According to [27], a one-armed structure develops when the dynamical center of the galaxy does not coincide with its center of mass. In turn, this is possible when the galaxy experiences a perturbation from another massive object. At the same time, NGC 5665 resembles Vorontsov–Vel'yaminov γ-shaped galaxies. Such γ shapes cannot form in isolated single galaxies.

The asymmetry of the brightness and colors in the circum-nuclear region of NGC 5665 (Figs. 4a–4c, 7a–7d) could also be a consequence of complex, noncentrally symmetric motions in the central regions of the galaxy. The active star formation observed in the spiral branches

Table 3. Characteristics of stellar aggregates

NGC	No.	$(B-V)_{0,\,i}$	$(V-R)_{0,\,i}$	$(V-I)_{0,\,i}$	d, pc	τ, 10^8 yr
5605	1	0.72	0.38	1.06	430	7–10
	2	0.39	0.39	0.87	430	4.5–5.5
	3	0.29	0.34	0.80	430	1–2
	4	0.65	0.43	1.15	430	7–10
	5	0.46	0.23	1.02	540	3–6
5665	1	0.52	0.33	0.86	240	4.5–5.5
	2	0.56	0.23	0.73	360	4–5
	3	0.77	0.67	0.88	430	9–15
	4	0.56	0.29	0.68	400	4–5
	5	0.68	0.32	0.64	290	5–6

and the presence of a large number of sites of star formation are also characteristic of interacting galaxies. It is striking that, in single galaxies with bursts of star formation, as a rule, the sites of star formation are observed in the spiral arms in the outer parts of the disk and have a substantial range of ages (as is the case, for example, in NGC 5605); in contrast, the burst of star formation in NGC 5665 occurred in the inner eastern part of the disk, and the galaxy's stellar aggregates all have the same age (5×10^8 yrs).

Thus, overall, our photometric studies confirm the hypothesis expressed in [9]: NGC 5665 is a galaxy undergoing interaction. The absence of nearby neighbors of NGC 5665 suggests that we may be dealing with a galaxy that has swallowed a small companion. Kinematic studies of NGC 5665 are required to further test this hypothesis.

5. CONCLUSIONS

(1) We have identified a modestly powerful burst of star formation in the disk and spiral branches of NGC 5605. The inner region of the galaxy has a standard-age stellar population.

(2) A burst of star formation occurred in the disk of NGC 5665 5×10^8 yrs ago. It was more powerful in the southeast part of the disk than in the northwest part.

(3) The photometric characteristics of NGC 5665 suggest that this galaxy is undergoing an interaction with another galaxy.

(4) We have identified sites of star formation with sizes characteristic of stellar aggregates with ages $(1–10) \times 10^8$ yrs in NGC 5605 and $(4–5) \times 10^8$ yrs in NGC 5665.

REFERENCES

1. G. de Vaucouleurs, A. de Vaucouleurs, H. G. Corwin, *et al.*, in *Third Reference Catalogue of Bright Galaxies* (Springer, New York, 1991).
2. A. I. Gamal El Din, I. A. Issa, A. M. I. Osman, and K. Y. Kamal, Astrophys. Space Sci. **190**, 67 (1992).
3. A. I. Gamal El Din, I. A. Issa, A. M. I. Osman, and K. Y. Kamal, Astrophys. Space Sci. **190**, 89 (1992).
4. C. J. Peterson, Publ. Astron. Soc. Pac. **94** (559), 404 (1982).
5. B. Rush, M. Malkan, and L. Spinoglio, Astrophys. J., Suppl. Ser. **89**, 1 (1993).
6. S. van den Bergh, Astron. J. **110**, 613 (1995).
7. G. Theureau, L. Bottinelli, N. Goudreau-Durand, *et al.*, Astron. Astrophys., Suppl. Ser. **130**, 333 (1998).
8. N. Devereux, Astrophys. J. **323**, 91 (1987).
9. G. Giuricin, L. Tamburini, F. Mardirossian, *et al.*, Astrophys. J. **427**, 202 (1994).
10. C. Magri, Astron. J. **108**, 896 (1994).
11. C. Giovanardi, G. Helou, E. E. Salpeter, and N. Krumm, Astrophys. J. **267**, 35 (1983).
12. D. A. Hunter, J. S. Gallagher, and D. Rautenkranz, Astrophys. J., Suppl. Ser. **49**, 53 (1982).
13. S. N. Pompea and G. H. Rieke, Astrophys. J. **356**, 416 (1990).
14. D. M. Elmegreen and B. G. Elmegreen, Astrophys. J. **314**, 3 (1987).
15. P. J. Grosbol, Astron. Astrophys., Suppl. Ser. **60**, 261 (1985).
16. M. Rowan-Robinson and J. Crawford, Mon. Not. R. Astron. Soc. **238**, 523 (1989).
17. J. J. Condon, E. Anderson, and J. J. Broderick, Astron. J. **109**, 2318 (1995).
18. D. Zaritsky, R. Smith, C. Frenk, and S. D. M. White, Astrophys. J. **405**, 464 (1993).
19. O. Dahari, Astrophys. J., Suppl. Ser. **57** (4), 643 (1985).
20. T. E. Nordgren, J. N. Chengalur, E. E. Salpeter, and Y. Terzian, Astrophys. J., Suppl. Ser. **115**, 43 (1998).
21. B. P. Artamonov, Yu. Yu. Badan, V. V. Bruevich, and A. S. Gusev, Astron. Zh. **76**, 438 (1999) [Astron. Rep. **43**, 377 (1999)].
22. A. S. Gusev, Candidate's Dissertation in Physical and Mathematical Science (Moscow, 1999).
23. A. U. Landolt, Astron. J. **104**, 340 (1992).
24. A. S. Gusev, Astron. Zh. (2000) (in press).
25. R. Buta and K. L. Williams, Astron. J. **109**, 543 (1995).
26. Yu. N. Efremov, *Sites of Star Formation in Galaxies* (FM, Moscow, 1989).
27. J. Colin and E. Athanassoula, Astron. Astrophys. **214**, 99 (1989).

Translated by D. Gabuzda

Photometric Properties of Bars in Galaxies

A. S. Gusev

Sternberg Astronomical Institute, Universitetskiĭ pr. 13, Moscow, 119899 Russia
Institute of Solid-State Physics, Russian Academy of Sciences, Chernogolovka, Moscow oblast, 142432 Russia

Abstract—We have used surface photometry data for 100 barred galaxies to determine the *UBVRIJHK* surface brightnesses and color indices for the bars. Two peaks are observed in the distribution of the average bar *B* brightnesses: at $21.0^m/\text{arcsec}^2$ and $22.2^m/\text{arcsec}^2$, characteristic of late- and early-type galaxies, respectively. The average surface-brightness difference between the bar and the galaxy (within the $25.0^m/\text{arcsec}^2$ isophote) increases from $1.1^m/\text{arcsec}^2$ for SB0 galaxies to $2.3^m/\text{arcsec}^2$ for SBc–IBm galaxies. In $(U-B)_0$–$(B-V)_0$, $(B-V)_0$–$(V-R)_0$, and $(B-V)_0$–$(V-I)_0$ two-color diagrams, for all morphological types, the bars are shifted leftward from normal color sequence for galaxies. This deviation is more pronounced for the outer than for the inner regions of the bars. Using evolutionary models, we show that this deviation is due to the scarcity of intermediate-age $[(1–9) \times 10^9$ yrs] stars in bars. Possible origins for this anomalous composition of the stellar population are discussed. © *2000 MAIK "Nauka/Interperiodica".*

1. INTRODUCTION

A statistical study of the photometric properties of galactic bars was initiated by Kalloglian [1], who determined the average surface brightnesses for nine galaxies and found the bar surface brightnesses to be roughly the same as for most galaxies: $20.90 \pm 0.2^m/\text{arcsec}^2$ in the *B* band. In the same study, he showed that about 75% of the bars had similar brightnesses, whereas the bar surface brightnesses in the remaining 25% of the galaxies were approximately 1^m fainter.

Elmegreen and Elmegreen [2] divided bars into two types, depending on the morphological type of their parent galaxy. The bars in early-type spirals (SB0–SBb) have flat brightness profiles along their major axes and are longer than the bars in late-type galaxies. In bars with flat photometric profiles, there is a continuous increase in the ellipticity of the isophotes along the bar [3]. The bars in late-type galaxies (SBc–IBm) are characterized by an exponential brightness decrease along their major axes. The ellipticity of the isophotes in such bars does not vary with distance from the center.

In contrast to bars with exponential brightness decreases, those with flat photometric profiles contain a relatively small amount of gas. This is evidently due to the fact that the gas content in early-type galaxies is, on average, lower than in late-type galaxies. OB associations are not uncommon at the ends of bars [4, 5]. Dust lanes along the leading edges of bars are also observed [6]. The bars in early-type galaxies are, on average, redder than those in late-type galaxies [7]. This is probably due to the fact that, on the whole, early-type galaxies are redder than late-type galaxies, due to the small contribution of the young stellar population to the total luminosity.

On the basis of photometric data, it was shown in [8] that there is no appreciable star formation in the bars of SBb galaxies, in contrast to SBc galaxies, in which there can be fairly intense star formation. Similar conclusions can be drawn from the study of Pronik [9], who considered the locations of bars of SBc galaxies in the two-color diagram.

Elmegreen *et al.* [10] explain the flat profiles of bars in early-type galaxies as a consequence of an excess of stars of all ages (both old and young) at the bar ends. Based on the *UBVR* colors of the SBbc galaxy NGC 151, whose bar has an exponential brightness decrease, it was concluded that intermediate-age stars are scarce in this bar [11].

The differences in the shapes of bars in early- and late-type galaxies could reflect the action of different mechanisms for bar formation in galaxies of different morphological types. It is generally believed that, in galaxies with rapidly rotating disks (when the disk rotation rate is much higher than the radial dispersion of the stellar velocities), bars are formed due to instability of the dynamically cold disk. The bars in such galaxies extend to the corotation region, since, at distances larger than the corotation radius, the main stable orbits become perpendicular to the major axis of the bar [12, 13]. The Lynden-Bell mechanism acts in galaxies with slowly rotating disks [14, 15]. Essentially, when stars are located in adjacent extended orbits, their orbits precess and approach each other due to gravitational instability, forming a bar. In this case, the radius of the bar cannot exceed the radius of the inner Lindblad resonance.

2. THE SAMPLE OF GALAXIES

Surface photometry has been performed for a large number of barred galaxies; however, these data have not been systematized. After surveying data published

Table 1. Average surface brightness and color indices of bars

	SB0 galaxies	N	SB0/Ba–SBbc galaxies	N	SBc–Ibm galaxies	N	All galaxies	N
$\langle B_0 \rangle$	22.04 ± 0.52	13	21.57 ± 0.56	32	20.93 ± 0.35	20		
$\langle V_0 \rangle$	21.36 ± 0.28	8	20.62 ± 0.38	24	20.47 ± 0.47	17		
$\langle (U-B)_0 \rangle$			0.13 ± 0.23	5	0.11 ± 0.27	10	0.12 ± 0.24	15
$\langle (B-V)_0 \rangle$	0.83 ± 0.18	8	0.82 ± 0.14	24	0.60 ± 0.23	16		
$\langle (V-R)_0 \rangle$	0.43 ± 0.08	6	0.43 ± 0.14	14	0.33 ± 0.12	9	0.40 ± 0.13	27
$\langle (R-I)_0 \rangle$	0.62 ± 0.15	7	0.70 ± 0.13	12	0.43 ± 0.06	3		
$\langle (I-J)_0 \rangle$							0.83 ± 0.16	3
$\langle (J-H)_0 \rangle$							0.66 ± 0.14	8
$\langle (H-K)_0 \rangle$							0.30 ± 0.07	6

over the last 40 years, we collected *UBVRIJHK* data for 100 barred galaxies. We sometimes used the average measured bar surface brightnesses directly. In most cases, however, we had to derive the average surface brightnesses and color indices from photometric profiles along the major axes of the bars. For "flat" bars, we used the brightness or color index averaged over the bar, while, for "exponential" bars, we used the values at half the length of the bar semimajor axis. In several cases, we used published isophote maps. The data were then corrected for Galactic absorption and absorption due to the inclination of the disk, in accordance with the technique proposed in the RC3 [16]. All the data were reduced to the Johnson–Cousins *UBVRI* and Elias *JHK* systems [17].

The resulting estimates of the surface brightnesses and color indices are summarized in an electronic table, which can be found in the Strasbourg CDS database and at the Internet site *http://lnfml.sai.msu.ru/~gusev/catalog/readme.html.* The columns of the table present (1) the NGC or IC numbers of the galaxies, (2) the morphological type of the galaxies according to the RC3, (3) the average surface brightnesses corrected for Galactic absorption and absorption due to the disk inclination in one of two indicated filters, (4)–(10) the bar color indices, and (11) the accuracy of the average bar surface brightnesses and color indices (the errors of the average values are presented). References to the initial sources are also given.

3. ANALYSIS OF THE PHOTOMETRIC DATA

3.1. Average Bar Surface Brightnesses

We divided all the galaxies into three groups according to morphological type: the first group includes 14 SB0 galaxies; the second, 47 SB0/Ba–SBbc galaxies; and the third, 39 SBc–IBm galaxies. For each of the three groups, we calculated the bars' average B_0 and V_0 surface brightnesses and the $(U-B)_0$, $(B-V)_0$, $(V-R)_0$, $(R-I)_0$, $(I-J)_0$, $(J-H)_0$, and $(H-K)_0$ color indices. These data are presented in Table 1, which also indi-

cates the number of galaxies considered. We can see a pronounced correlation between the galaxy type and the average bar surface brightness: on average, the bars in late-type galaxies are brighter.

Figure 1 presents histograms of the average B surface-brightness distributions for the bars and their parent galaxies. The magnitudes corrected for absorption B_0^T, major axes D_0, and axis ratios R_{25} used to derive the values in the histogram in Fig. 1b were taken from the RC3. The two histograms differ considerably: the galaxy distribution is normal (Gaussian), with a maximum at $23.1^m/\text{arcsec}^2$ and rms deviation $0.4^m/\text{arcsec}^2$, while the bar distribution is bimodal and has a relatively large dispersion. A χ^2 test shows that the distribution in Fig. 1a is inconsistent with a normal distribution at the 0.91 significance level.

Two peaks can be seen in the brightness distribution for the bars (see the histogram in Fig. 1a): one at $21.0^m/\text{arcsec}^2$ and a second, weaker, peak at $1.2^m/\text{arcsec}^2$. This is in fairly good agreement with earlier studies (see, for example, [1]); however, there is no distinct division between these two maxima in our sample. The relative numbers of bright and weak bars (taking the boundary between them to be $21.67^m/\text{arcsec}^2$, the local minimum in the histogram in Fig. 1a) also differ from those found earlier: $60 \pm 10\%$ bright bars and $40 \pm 10\%$ weak bars (as opposed to 75 and 25%, as found by Kalloglian [1]).

Note also the distribution for the second group of galaxies (SB0/Ba–SBbc): while the maximum for SB0 galaxies virtually coincides with the weak peak (in brightness) for the bars and the maximum for SBc–IBm galaxies coincides with the bright peak (Fig. 1a and Table 1), the distribution for SB0/Ba–SBbc galaxies is rather uniform over a wide range. These galaxies make up about half the galaxies contributing to both peaks (Fig. 1a), and their mean surface brightness (Table 1) lies between the two maxima in the histogram.

Thus, the bars can be divided into two photometric types according to parent galaxy type: early- and late-type

bars. SB0/Ba–SBbc galaxies possess bars of both types. This is in agreement with the results of Elmegreen and Elmegreen [2], who divided bars into two types according to their photometric profiles and relative lengths (see Section 1).

The difference between the average surface brightness of the bar and of the galaxy as a whole, $B_{0,bar} - \mu(B_0)_{gal}$, increases from $1.1 \pm 0.4^m/\text{arcsec}^2$ for SB0 galaxies and $1.5 \pm 0.4^m/\text{arcsec}^2$ for SB0/Ba–SBbc galaxies to $2.3 \pm 0.4^m/\text{arcsec}^2$ for SBc–IBm galaxies; i.e., bars in late-type galaxies are photometrically more distinct against the disk background than those in early-type galaxies.

3.2. Integrated Bar Color Indices

The average color indices of the bars are essentially independent of the morphological type of the parent galaxy. The only exceptions are the color indices $(B - V)_0$ and $(R - I)_0$ (Table 1). Estimates of U brightnesses and $(U - B)_0$ are too scarce for us to derive reliable average values. Late-type galaxies have appreciably lower $(B - V)_0$ and $(R - I)_0$ values than do SB0–SBbc galaxies. Precisely these low $(B - V)_0$ values are responsible for the relatively higher brightness of the bars in late-type galaxies at blue wavelengths.

The bars in all galaxies display the same infrared color indices; their average surface brightnesses, however, are different and depend on the morphological type of the galaxy (see the electronic table and Table 1). The infrared data for SB0 galaxies are untrustworthy due to their poor statistics.

The distribution of the $(B - V)_0$ color indices of the bars is of special interest. The corresponding histogram is presented in Fig. 2a, while, for comparison, Fig. 2b shows the distribution of the integrated $(B - V)_0$ values from the RC3 catalog. While the integrated color indices of the galaxies are well correlated with their morphological types (Fig. 2b), there is a pronounced peak in the bar distribution at $(B - V)_0 = 0.8^m$. The bars in SB0 and SB0/Ba–SBbc galaxies have essentially the same colors (Table 1); only in extremely late-type galaxies are the bars, on average, 0.2^m bluer. Thus, the influence of galactic morphological type on bar color is weaker than its influence on the average bar surface brightness.

We can interpret the data in Fig. 2a and Table 1 as follows. In the bars of late-type galaxies (SBc–IBm), star formation is more active and the contribution of the young stellar population to the total luminosity larger than in bars in early-type galaxies (SB0–SBbc). Therefore, $(B - V)_0$ and $(R - I)_0$, which are sensitive to star formation, are lower in the bars of late-type galaxies than in those of SB0–SBbc galaxies. The lack of such a dependence for $(U - B)_0$ is probably due to the poor statistics for bars in early-type galaxies (Table 1). This may also be related to the fact that the stellar populations in galaxies of different morphological types have different age distributions (a displacement from the normal color
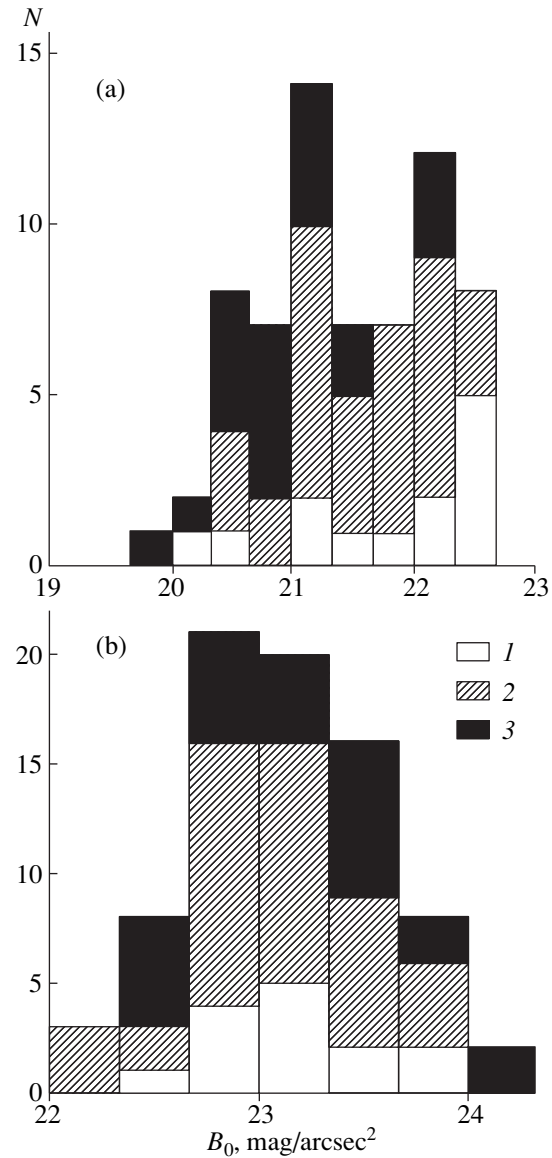

Fig. 1. Distributions of the number of galaxies as a function of (a) average bar surface brightness and (b) intrinsic average surface brightness. 1—SB0 galaxies, 2—SB0/Ba–SBbc galaxies, 3—SBc–IBm galaxies.

sequence for galaxies in the $(U - B)_0$–$(B - V)_0$ two-color diagram).

3.3. Location of the Bars in Two-Color Diagrams

Of the 100 galaxies in our sample (see Section 2), 42 have data for two or more UBVRI color indices for their bars. We studied the locations of the bars in three two-color diagrams: $(U - B)_0$–$(B - V)_0$, $(B - V)_0$–$(V - R)_0$, and $(B - V)_0$–$(V - I)_0$ (Figs. 3a, 3b, and 3c, respectively). The straight line in the diagrams indicates the normal sequence for the integrated colors of galaxies (NCS), taken from the study of Buta and Williams [18], who used the color indices for 501 galaxies
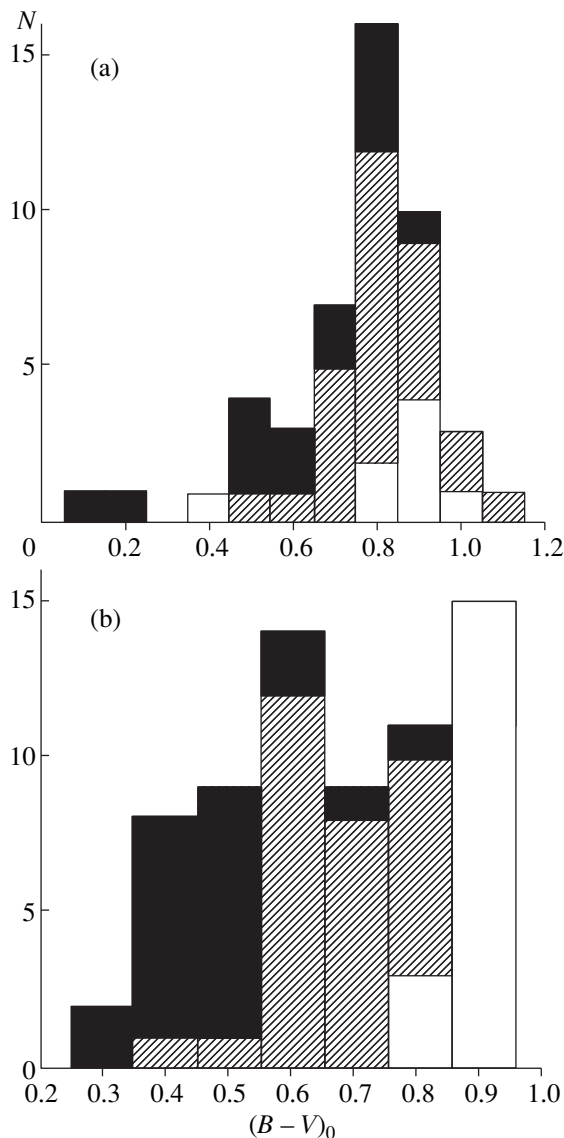
Fig. 2. Distributions of the number of galaxies as a function of (a) $(B - V)_0$ for their bars and (b) intrinsic $(B - V)_0$. The types of galaxies are denoted as in Fig. 1.

from the RC3 [16]. The sequences derived by Buta and Williams [18] are consistent with those obtained in previous studies, based on both observations and simulations of galaxy colors. For comparison, Fig. 4 presents two-color diagrams with the locations for the galaxies in our sample indicated (we used the integrated color indices from [16] and [18]).

As we can see in Fig. 3, most of the bars are located to the left of the NCS, most noticeably in the $(B - V)_0$–$(V - R)_0$ diagram. The $(U - B)_0$–$(B - V)_0$ two-color diagram is of special interest. Here, in most cases, only the bars of late-type galaxies, starting with type SBc, are located to the left of the NCS. However, the poor statistics for early-type galaxies with known $(U - B)_0$ values prevent us from determining whether the bars of

early- and late-type galaxies diverge. In most cases, the errors in the brightnesses and colors of the bars in our sample are 0.1^m (see the electronic table). For a sample of bars in galaxies without an intense burst of star formation with more accurately determined color indices, the number of bars located to the right of the NCS in two-color diagrams (including $(U - B)_0$–$(B - V)_0$) becomes essentially zero (see, for example, Fig. 5a).

Galaxies of different morphological types are clearly separated in the two-color diagrams: late-type galaxies are located to the left of and above early-type galaxies (Fig. 4). The location of bars in the two-color diagrams depends on the parent galaxy type much more weakly (Fig. 3). This is consistent with the result described in Section 3.2: the color indices of bars depend only weakly on the morphological type of the parent galaxy.

The integrated color indices for a few of the late-type galaxies in our sample are displaced to the right of the NCS (Figs. 4b, 4c). This probably reflects the presence of starburst galaxies in the sample. At the same time, there are no appreciable differences in the positions of barred and unbarred galaxies in the two-color diagrams [18].

We will consider below a possible explanation for the displacement of the bar color indices to the left of the normal color sequence for galaxies.

3.4. Color Variations along the Bar Major Axis

In a number of studies (Table 2), variations of colors along bars as a function of distance from the center can be traced. The results are presented in Fig. 5. To reduce the number of figures, we present a $(U - V)_0$–$(V - R)_0$ diagram instead of the commonly used $(B - V)_0$–$(V - R)_0$ diagram (see Table 2). In total, ten galaxies were studied in this way. With only one exception (NGC 1620), we can clearly see a deviation of the bar color indices in the two-color diagram toward the left; i.e., the bars become bluer with increased distance from the galaxy nucleus.

The bars of all galaxies lie to the left of the NCS in the two-color diagrams. The two exceptions are the bars in the peculiar galaxy NGC 5665 and the starburst galaxy NGC 6217. The bars of these galaxies lie to the right of the NCS (Fig. 5; the opposite parts of the bars in NGC 5665 and NGC 6217 are displayed separately). This reflects the known fact that a burst of star formation in an old stellar system displaces the points in two-color diagrams toward the right [18].

3.5. A Possible Origin for the Anomalous Color Indices of Bars

An anomalously low bar $(V - R)_0$ color index compared to the integrated disk color was first noted in the $(B - V)_0$–$(V - R)_0$ two-color diagram for the galaxy NGC 4027 by Pence and de Vaucouleurs [24]. They explained the displacement of the integrated bar color-
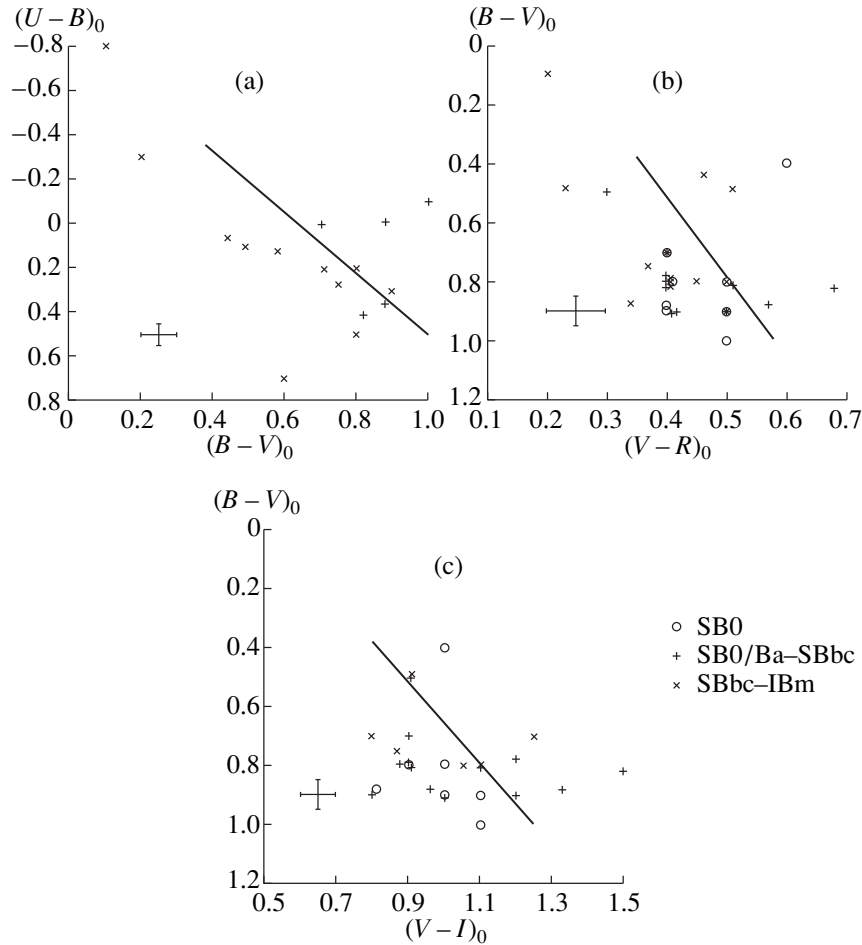
Fig. 3. (a) $(U-B)_0$–$(B-V)_0$, (b) $(B-V)_0$–$(V-R)_0$, and (c) $(B-V)_0$–$(V-I)_0$ two-color diagrams for the bars. The different symbols denote galaxies of different morphological types. The straight lines represent the NCS of galaxies. The observational errors for the bar color indices are indicated.

index points to the left of the NCS as a consequence of the relatively low H_α flux from the area occupied by the bar. However, this is not a plausible explanation for the displacement of the bar color indices in the $(U-B)_0$–$(B-V)_0$ diagram.

Odewahn [4] also detected a displacement of the color indices of the bar of NGC 4618 to the left of the NCS in $(B-V)_0$–$(V-I)_0$ and $(B-V)_0$–$(B-I)_0$ diagrams. He explains the anomalously blue $(V-I)_0$ of the bar relative to the integrated disk colors as the effect of enhanced formation of massive stars in the bar. The initial mass function (IMF) of stars can, indeed, differ from the classical function in the regions of intense shock waves observed in bars: in these areas, relatively large numbers of massive stars can form. However, the excess of massive, young stars should have an even greater effect on the bar's $(B-V)_0$, which is not seen for NGC 4618, whose bar and disk have the same $(B-V)_0$.

Using the $(U-B)_0$–$(B-V)_0$ diagram, Esipov *et al.* [11] considered variations in the color indices of the bar of NGC 151 along the bar's major axis as a function of distance from the center. They attribute the bluer color of the outer areas of the bar to an increase in the contribution of young stars (with ages less than 10^9 yrs) at the peripheral zones of the bar. At the same time, they suggest that the displacement of the bar color-index points to the left of the NCS reflects a scarcity of intermediate-age stars ($\sim10^9$ yrs) in the bar. This situation can arise if stars formed in the bar leave it shortly thereafter.

The displacement of the color indices of a stellar system to the right or left of the NCS in two-color diagrams can, indeed, be explained by an absence of intermediate-age stars in the system (or an excess of both old and young stars at the same time); the presence of stars with ages of the order of 10^9 yrs, with no old and young stars; or an IMF such that a relative excess of massive stars is formed. Model calculations for the color indices of such stellar systems have not been carried out previously.

Neither the presence of dust nor the occurrence of a burst of star formation in a stellar system can displace a galaxy's color indices to the left of the NCS in two-
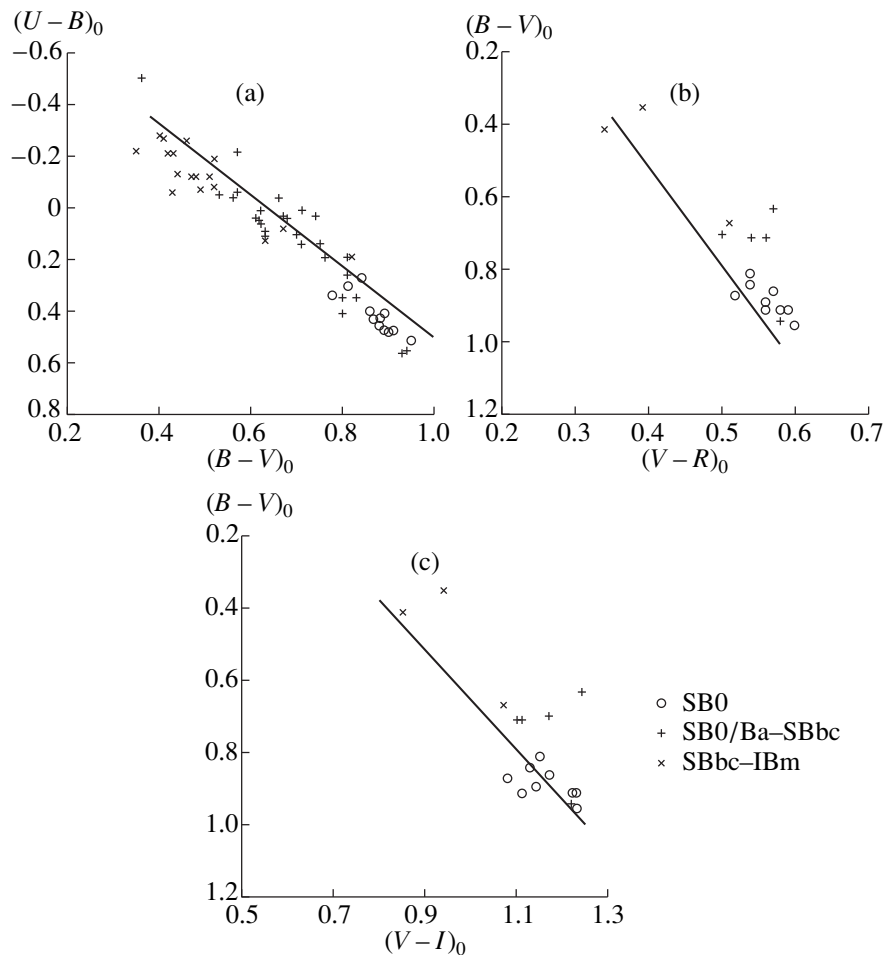
Fig. 4. (a) $(U-B)_0$–$(B-V)_0$, (b) $(B-V)_0$–$(V-R)_0$, and (c) $(B-V)_0$–$(V-I)_0$ two-color diagrams for the integrated colors of barred galaxies. The different symbols denote galaxies of different morphological types. Smaller symbols denote galaxies from our sample that are not included in the list of Buta and Williams [18]. The straight lines represent the NCS of galaxies (according to [18]).

color diagrams. A burst of star formation will displace points toward the right; stable, intense star formation (for example, with a constant star-formation rate) will displace them upward and to the left along the NCS [25]; the presence of strong absorption will shift them downward and to the right along the NCS [18]. Systems with stellar populations indicating an increased heavy-element abundance deviate from the NCS only in the $(U-B)_0 - (B-V)_0$ diagram (in other diagrams, the displacement is along the NCS). Therefore, in our modeling of the population in a stellar system, we considered only the three cases mentioned above: (a) a deficit of intermediate age stars, (b) the presence only of intermediate age stars, and (c) an excess of massive stars.

4. MODELING THE STELLAR POPULATIONS OF GALACTIC BARS

4.1. Method and Initial Parameters

We used an evolution modeling technique to investigate the stellar populations of galactic bars. We adopted the PEGASE code developed in the Paris Insti-

tute for Astrophysics by M. Fioc and B. Rocca-Volmerange [26] and also the code developed by G. Worthey [27]. In the simulation with the PEGASE code, we used the Padua stellar library of evolutionary tracks for stars with $Z = 0.02$ [28]. The IMF suggested by Kennicutt [29] was adopted, which, in our opinion, is best suited to studies of the stellar populations of galaxies (see, for example, the discussion on different IMFs in [30]). In the modeling with Worthey's code [27], we used the Lick stellar library of evolutionary tracks and a Salpeter IMF.

One important feature of our modeling of the color indices of stellar systems is that, unlike the models acquired with the PEGASE code [26], Worthey's code [27] takes into account the evolution of the chemical composition of the system. We took the $Z(t)$ dependence for galaxies of various morphological types from the results obtained using the PEGASE code. When, in the course of evolution of the stellar system, the value $Z = 0.02$ was reached at some time t_Z, it was assumed that the stars formed from that point on possess solar chemical composition.

Table 2. Color variations along the bar major axis

NGC	Type	Two-color diagrams	References	Notes
151	SBbc	$(U-B)_0$–$(B-V)_0$	[8]	–
523	pec	$(U-B)_0$–$(B-V)_0$	[19]	–
1620	SBc	$(U-B)_0$–$(B-V)_0$	[20]	–
5605	SABcp	$(B-V)_0$–$(V-R)_0$	[21]	–
		$(B-V)_0$–$(V-I)_0$		
5665	SABcp	$(B-V)_0$–$(V-R)_0$	[21]	Northwestern and southeastern parts of the bar were considered separately
		$(B-V)_0$–$(V-I)_0$		
6217	SBbc	$(U-B)_0$–$(B-V)_0$	[22]	Northern and southern parts of the bar were considered separately
		$(B-V)_0$–$(V-R)_0$		
		$(B-V)_0$–$(V-I)_0$		
7292	Irr	$(U-V)_0$–$(V-R)_0$	[20]	–
7479	SBc	$(U-B)_0$–$(B-V)_0$	[23]	–
7678	SABc	$(U-B)_0$–$(B-V)_0$	[19]	–
7743	SB0/Ba	$(U-B)_0$–$(B-R)_0$	[20]	The bar $(B-V)_0$ values obtained in [18] were used to represent the galaxies in Figs. 5b and 5c

Unfortunately, when using the Lick stellar library of evolutionary tracks, Worthey's code [27] enables modeling only of old stellar systems (with ages of the stars $\geq 1 \times 10^9$ yrs). To take into account the contribution of young stars (with ages less than 1×10^9 yrs), we used the PEGASE code [26] with a Salpeter IMF.

The age of the galaxies T was taken to be 1.2×10^{10} yrs. The parameter describing the time dependence of the star-formation rate (SFR) was a variable. Let us consider this dependence in more detail. Sandage [31] proposed simple empirical laws to describe the time dependence of the SFRs for galaxies of various types. In elliptical galaxies, the SFR decreases exponentially as a function of time (on a shorter time scale than in spiral galaxies); in S0–Sc galaxies, the SFR is, in general, proportional to the mass of the gas in the galaxy at that time (i.e., the star-formation efficiency is constant with time, while the SFR decreases exponentially); in Sd galaxies, the SFR is constant. Following Sandage, we used these three time dependences for the SFRs.

Corresponding formulas are presented in Table 3; M is the total mass of the galactic disk. We took the time dependence of the SFR for elliptical galaxies from [32]; the analogous dependences for spiral galaxies were chosen based on standard SFRs and star-formation efficiencies for early- and late-type galaxies derived from observations. For brevity, we will call the SFR time dependences in Table 3 "normal."

In modeling stellar systems without intermediate-age stars (we denote the ends of the age interval t_{min} and t_{max}), we used the following procedure to tie the NCS obtained from color-index simulations to the NCS derived observationally (in the diagrams, the model and observed NCSs coincide to within 0.1^m). Initially, the

$UBVRI$ luminosities for systems with normal SFR time dependences were determined. Then, the data were tied to the NCS used in Section 3.3 (adopting the values for L_B and $(B-V)_0$ as "zero points"). Further, we determined the $UBVRI$ luminosities for a system with no star formation from 1.2×10^{10} yrs ago to t_{max} and from t_{min} to the present time, and with the normal SFR time dependence during the time from t_{max} to t_{min} (the input parameters were normalized accordingly). Finally, the $UBVRI$ luminosities obtained in the first and second cases were subtracted. In this way, we obtained luminosities in these bands for systems with no stars with ages from t_{min} to t_{max}. In total, we considered 11 models for each of the three types of galaxies: nine models using the PEGASE code [26] (systems without stars with ages 0.5–1, 0.5–3, 0.5–5, 0.5–9, 1–3, 1–5, 1–9, 3–5, and $(5–9) \times 10^9$ yrs) and two using Worthey's code [27] (systems with no stars with ages 1–9 and $(1–11) \times 10^9$ yrs).

We modeled stellar systems populated exclusively by intermediate-age stars using the PEGASE code. We assumed that, over some time interval, all the matter in the system would be converted to stars at some constant SFR. We considered five models: systems in which all stars are formed during intervals of 10^6, 10^7, 10^8, 10^9, and 3×10^9 yrs.

When modeling stellar systems with an excess of massive stars, we used the PEGASE code and varied the IMF. We considered the following two cases.

(1) The IMF corresponds to Kennicutt's [29] IMF for stars with masses $0.1–1 M_\odot$ ($f(M) \sim M^{-1.4}$) and differs from it for stars with masses $1–120 M_\odot$ ($f(M) \sim M^{-2.5}$ is the standard Kennicutt IMF [29], and we used $f(M) \sim M^{-\alpha}$ for the models). We considered six models for each of
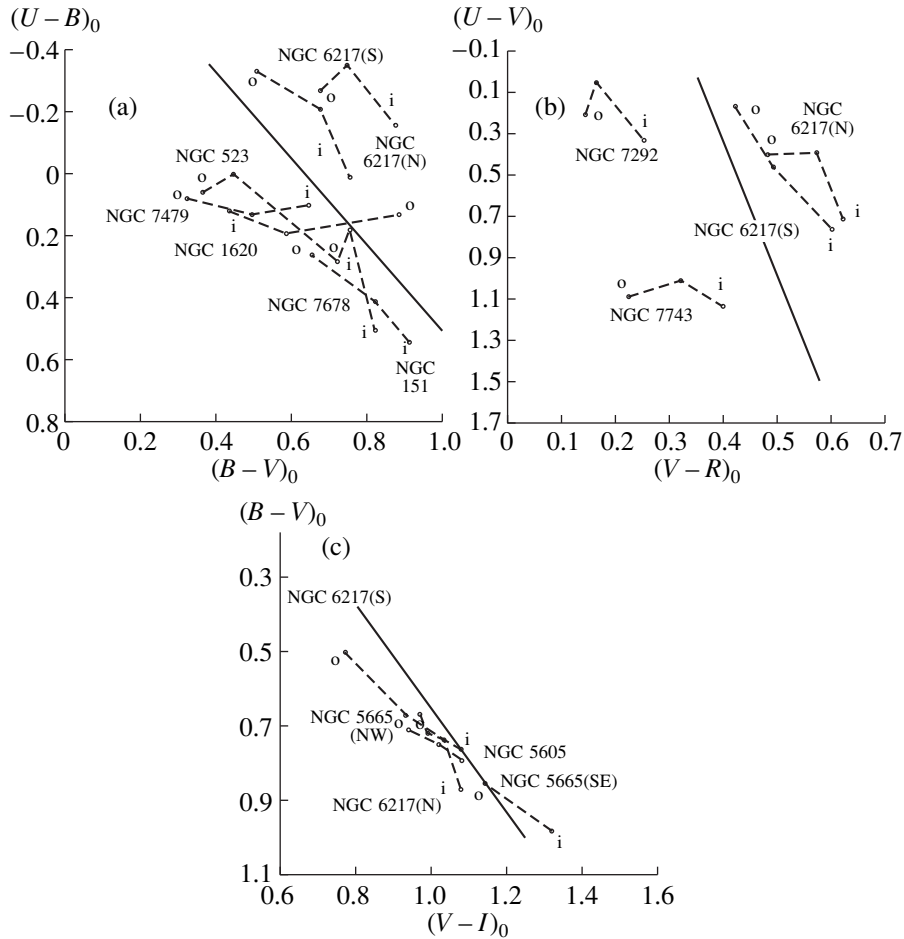
Fig. 5. (a) $(U-B)_0$–$(B-V)_0$, (b) $(U-V)_0$–$(V-R)_0$, and (c) $(B-V)_0$–$(V-I)_0$ two-color diagrams. The dashed curves show variations in the color indices along the bar semimajor axis from inner ("i") to outer ("o") areas. The solid lines show the NCS of galaxies.

the three types of galaxies: systems with IMFs for stars with masses 1–$120 M_\odot$ with indices $\alpha = 2.2$, 2.0, 1.8, 1.6, 1.4, and 1.2.

(2) The IMF of the system corresponds to Kennicutt's [29] IMF for stars with masses larger than some M_{crit} and is zero for stars with lower masses. We considered three models for each of the three types of galaxies: systems with $M_{crit} = 1$, 3, and $10 M_\odot$.

4.2. Model Results

Figures 6 and 7 present two-color diagrams with color sequences for the systems without intermediate-age stars. The systems with SFRs corresponding to

Table 3. SFRs for galaxies of different morphological type

Galaxies	SFR
Ellipticals	$1.2 \times 10^{-9} M \exp(-t/10^9)$
Early-type spirals	$5 \times 10^{10} M \exp(-t/3.1 \times 10^9)$
Late-type spirals	$10^{-10} M$

those of late-type galaxies are in the upper left corners of the diagrams, while those with SFRs corresponding to those of elliptical galaxies are in the lower right corners. With the exception of the active starburst galaxies (see Sections 3.3, 3.4), the observed bar color indices are also plotted in these diagrams. Note that most of the model sequences deviate from the NCS by only a very small amount, only slightly exceeding the error intervals for the color indices of most bars. However, the accuracy of the color indices for the bars in the galaxies in Table 2 is sufficient for meaningful comparisons with the model dependences.

The model color sequences for stellar systems without stars with ages $(1$–$9) \times 10^9$ yrs acquired using the PEGASE [26] and Worthey [27] codes are somewhat different (cf. Figs. 6 and 7). The largest discrepancy can be seen for the model colors of early-type galaxies. This is largely due to the different chemical compositions of the old stellar populations in the model systems obtained using the two codes. The contribution of the old stellar population to the total luminosity of a system decreases from early- to late-type galaxies (see below). For this reason, in the two-color diagrams, the positions
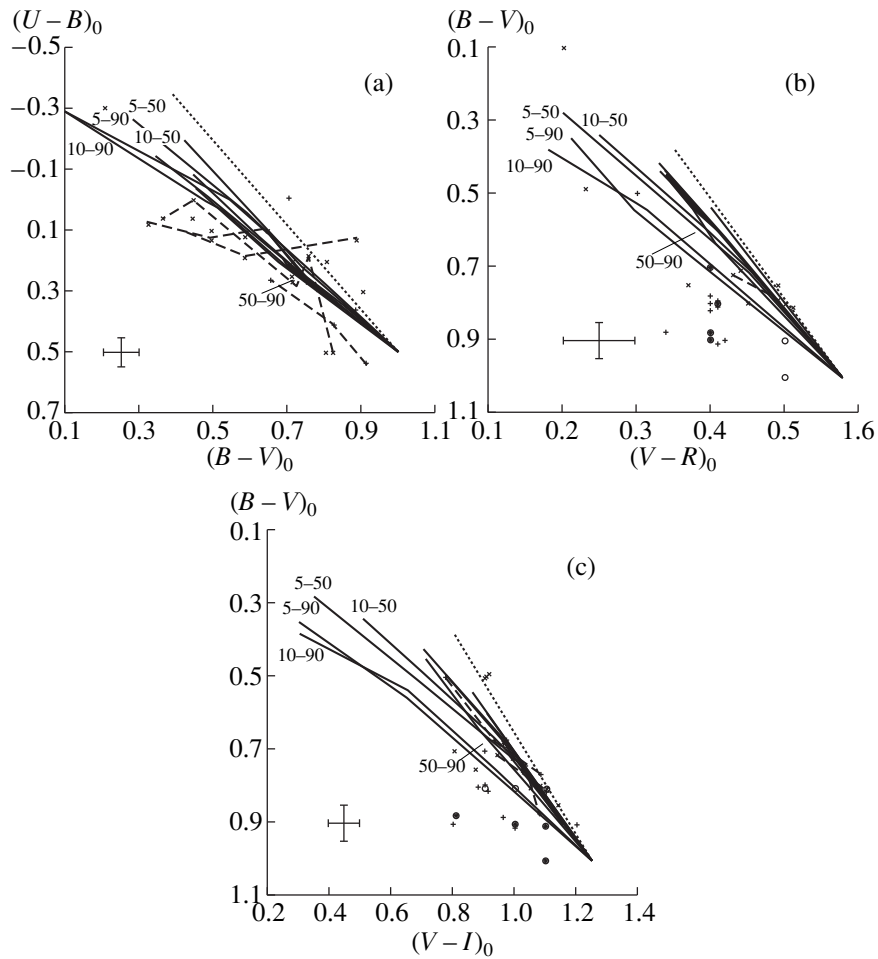
Fig. 6. Model sequences (solid) for systems without intermediate-age stars (age intervals in 10^8 yrs are denoted by the numbers) in the (a) $(U − B)_0–(B − V)_0$, (b) $(B − V)_0–(V − R)_0$, and (c) $(B − V)_0–(V − I)_0$ two-color diagrams, obtained using the PEGASE code. Systems with SFRs corresponding to late-type galaxies are located in the upper left corner, while systems with SFRs corresponding to elliptical galaxies are in the lower right corner. The dotted lines represent the NCS of galaxies. For comparison, the dashed lines indicate the observational data for bars in galaxies that are not undergoing active bursts of star formation (the labels are the same as in Fig. 5). The observational errors for the bar color indices are indicated.

of systems with SFRs corresponding to those typical of late-type galaxies obtained using the PEGASE [26] and Worthey [27] codes differ only slightly (Figs. 6, 7).

As we can see from Figs. 6 and 7, the color indices for models without intermediate-age stars are displaced in the same direction from the NCS as the observed color indices of most bars. Most bars in galaxies with low SFRs occupy the area in the two-color diagrams corresponding to stellar systems without stars with ages $(1–9) × 10^9$ yrs (Figs. 6, 7).

In the $(U − B)_0 − (B − V)_0$ diagram, points corresponding to the outer parts of the bars of most galaxies lie to the left of the model color sequences. It is likely that the OB associations located at the ends of these bars are so intense that they totally dominate the radiation from the old stellar population in the outer areas of the bars (for systems without star formation $(1–9) × 10^9$ yrs ago, the fraction of stars younger than 10^9 yrs making up the total B luminosity varies from 94% for late-type galax-

ies and 77% for early-type galaxies to 0.07% for elliptical galaxies).

The slight deviation of the bars from the model sequences in the $(B − V)_0 − (V − R)_0$ and $(B − V)_0 − (V − I)_0$ diagrams may be due to selective absorption: the bars have a rather large amount of dust (see Section 1). The $(U − B)_0 − (B − V)_0$ diagram is less sensitive to internal absorption in stellar systems, since the model sequences here deviate from the NCS to a smaller degree.

On the whole, the model color sequences for systems without intermediate-age stars in all the two-color diagrams can account for the positions of most of the observed bars. The model color sequences for systems without stars with ages $(0.5–9) × 10^9$, $(1–9) × 10^9$, and $(1–11) × 10^9$ yrs in the $(B − V)_0–(V − R)_0$ and $(B − V)_0–(V − I)_0$ diagrams virtually coincide. This prevents us from more accurately determining the age interval for the stars that are deficient in the bars.
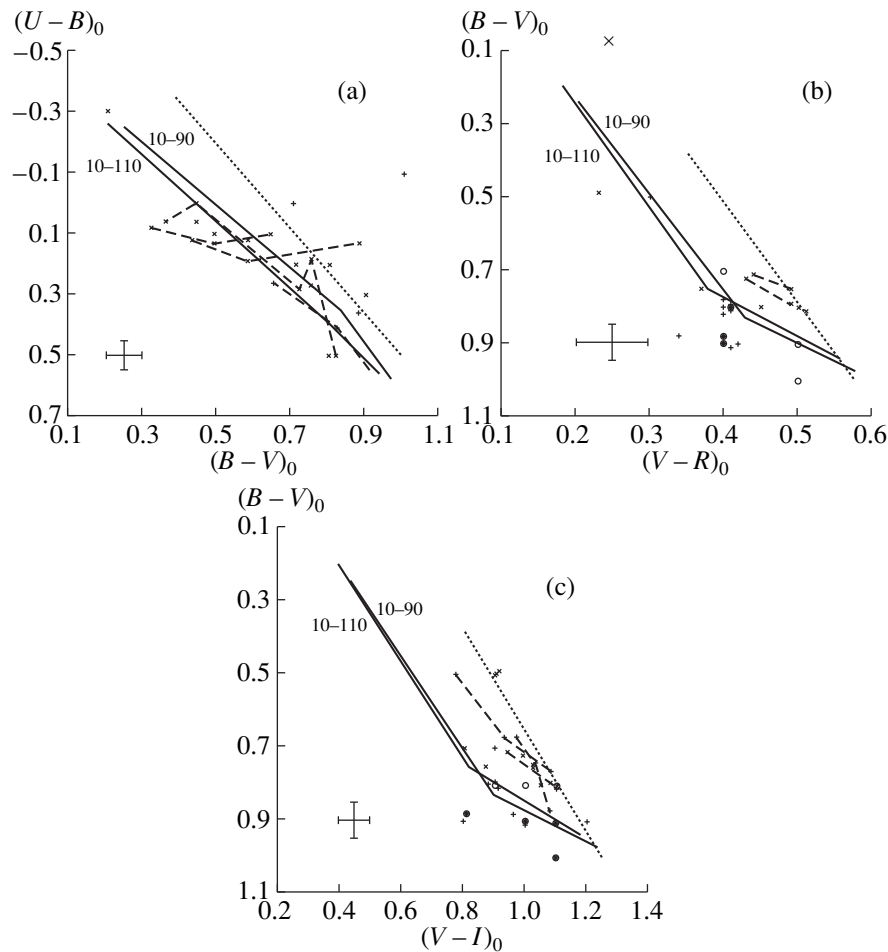
Fig. 7. Same as Fig. 6 for the model sequences obtained using Worthey's [27] code.

Our modeling for the color indices of stellar systems with nonstandard initial mass functions and systems with only intermediate-age stellar populations showed inconsistency between the model sequences and observed bar color indices. As an example, the two-color diagrams in Fig. 8 show evolutionary tracks for systems with stellar populations of approximately the same age. In the $(U - B)_0$–$(B - V)_0$ diagram, most galactic bars do indeed have the same colors as stellar systems consisting only of stars with intermediate ages (5×10^8–3×10^9 yrs). However, in the $(B - V)_0$–$(V - R)_0$ and $(B - V)_0$–$(V - I)_0$ diagrams, most bars are located far to the side of the evolutionary tracks. The model sequences for systems with nonstandard IMFs (systems without low-mass stars or those with a more sloping IMF) are also located either along or to the right of NCS, so that they are even less consistent with the observations for the bars.

Therefore, the displacement of the bar color indices to the left of the NCS is most likely due to a deficit of intermediate-age stars. The fact that there is a relative deficit of star clusters with ages 5×10^8–6×10^9 yrs in the bar of the Large Magellanic Cloud [33] supports this conclusion.

5. DISCUSSION

The deficit of intermediate-age stars in bars can be understood as a result of the fact that, after the formation of the bar, the stars formed in it leave the bar within about 10^9 yrs [11]. The hypothesis that a relatively young bar (formed later than 10^9 yrs ago) is observed against the background of an older disk stellar population is not suitable here, since, for the standard SFR, we would observe for all types of spiral galaxies (including SB0) only an excess of young stars against the background of the standard stellar population.

Bars in early-type galaxies form over periods of 2×10^8–1.2×10^9 yrs [34, 35]. From the time of its formation, the bar potential has a profound impact on the dynamics of the stars and gas in the galaxy. Old stars in the bar move along very elliptical orbits (the x_1 set of orbits, according to the nomenclature of [13]). Radial movements of gas along the bar can result in the formation of an active nucleus in early-type galaxies and in a burst of star formation in late-type galaxies [36, 37]; at the same time, radial gas movements can increase the gas density at the ends of the bar and, consequently,
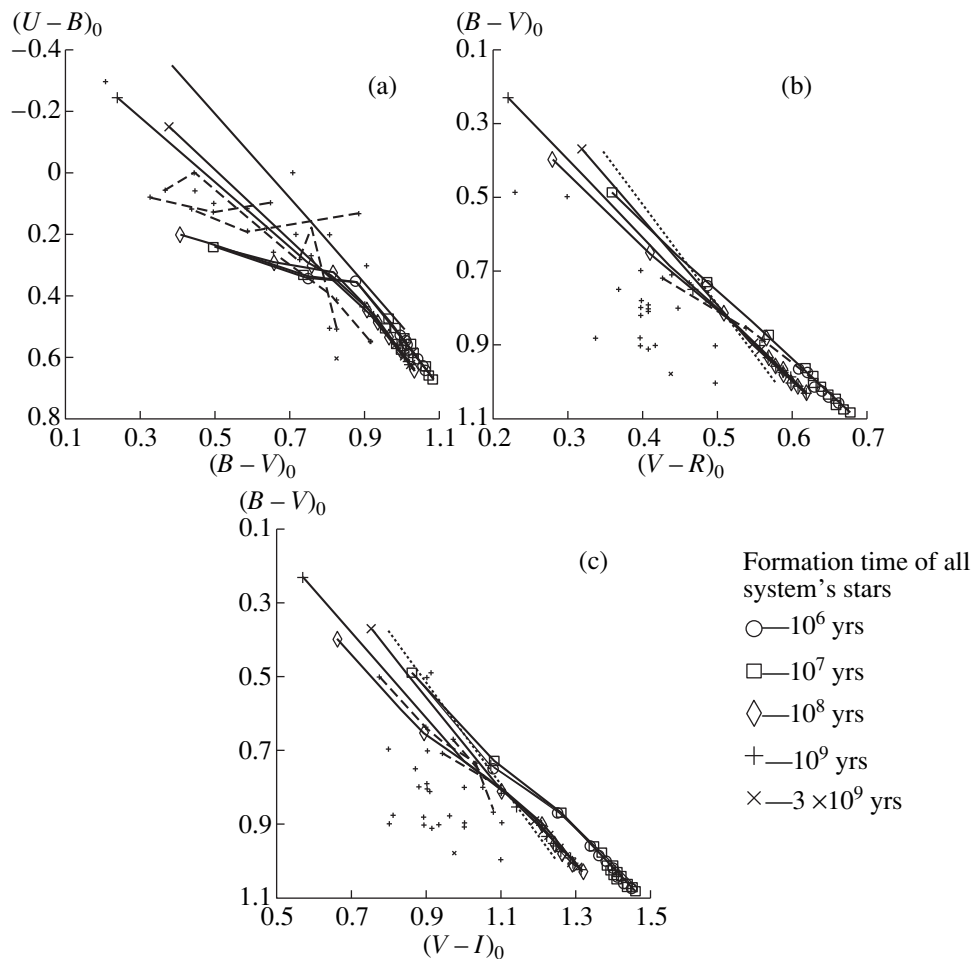
Fig. 8. (a) $(U-B)_0$–$(B-V)_0$, (b) $(B-V)_0$–$(V-R)_0$, and (c) $(B-V)_0$–$(V-I)_0$ two-color diagrams with evolutionary tracks for stellar systems (solid curves) with bursts of star formation that lasted for some time, after which star formation ceased. The corresponding symbols indicate the locations of systems with ages of 0.5, 1, 2, 3, ..., 12×10^9 yrs whose stars were formed within 10^6, 10^7, or 10^8 yrs; of systems with ages of 1, 2, 3, ..., 12×10^9 yrs whose stars were formed within 10^9 yrs; and of systems with ages of 3, 4, 5, ..., 12×10^9 yrs whose stars were formed within 3×10^9 yrs. Time is measured from the start of the burst of star formation 1.2×10^{10} yrs ago. The systems evolve from the upper left corner to the lower right corner of the diagrams. The dotted line represents the NCS of galaxies. The asterisks correspond to the observed color indices of bars in galaxies that are not undergoing active bursts of star formation.

intensify the star formation there [38]. In the presence of inner Lindblad resonance, gas clouds reach the bar at some angle (at an angle of 90° for two inner Lindblad resonances), forming a shock wave at the leading edge of the bar [39]. Before passing through the shock, the gas has a low density and, in the general case, moves toward the end of the bar. After its passage through the shock, the now high-density gas moves toward the nucleus of the galaxy. Dust lanes are an observational manifestation of this shock; appreciable star formation is not observed along these lanes in the bars of early-type galaxies [38].

Thus, in bars that do not contain a large amount of gas, stars form primarily near the nucleus and in the outer regions of the bar [40]. The stars that form move in either circular orbits about the nucleus or in highly elliptical orbits about the bar major axis (the orbits for old bar stars are less elliptical). However, in the regions of the bar that are most distant from the center, radial stellar orbits become unstable, since they end up either in the region of inner Lindblad resonance (the outer boundary of bars in late-type galaxies) or at a distance corresponding to the corotation radius (the inner boundary of bars in early-type galaxies). In addition, the bar potential is capable of dynamically heating the disk due to the presence of both vertical and horizontal inner Lindblad resonances: stars forming in the disk and bar can leave the galactic plane, enriching the bulge [35, 37, 41].

This picture is valid for bars that have formed due to the instability of a rapidly rotating disk. No serious gas and stellar dynamics studies have been carried out for galaxies with bars whose formation is due to instability of radial orbits (the Lynden-Bell mechanism). It is likely, however, that the stellar and gas dynamics in

bars of this type are similar to those described above. This conclusion is supported by the fact that two-color diagrams do not show any significant differences in the locations of bars belonging to galaxies of different morphological types (see Section 3.3) and also by the detection of dust lanes in the bars of galaxies of all morphological types ranging from SB0 to SBm. The only differences between bars of late- and early-type galaxies are that the former have an exponential brightness decrease along the bar major axis [2] and that the star formation in these bars occurs along the entire length of the bar [37]. The formation time for such bars (~10^8 yrs [15]) roughly corresponds to that for bars in rapidly rotating disks. The influence of the bar on the motions of stars and gas in the bar region is probably the same, independent of how the bar was formed.

Thus, young and old stars in the bar have different trajectories of motion. It seems likely that young stars formed at the ends of the bar gradually leave it and enter the inner areas of the disk and bulge. However, the supply of gas to the bar, and consequently the star formation in it, must be continuous, since young stars (younger than 5×10^8–1×10^9 yrs) are observed in bars. Star formation is most intense at the ends of bars, since a large amount of gas is concentrated there, so that the stellar population becomes younger as we approach the ends of bars. Older stars that appeared before and at the time of formation of the bar are also always present in bars.

Another possible explanation for the deficit of intermediate-age stars in bars is the ejection of stars from outer areas of the bar into the inner circumnuclear area of the bar. In this case, the radiation of these stars will be suppressed by that from the nucleus and bulge of the galaxy.

The aperture photometry data presented in Table 2 indicate that, in apertures with diameters equal to, or slightly larger than, the length of the bar, the $(U - B)_0$, $(B - V)_0$, and $(V - R)_0$ values correspond to the NCS; i.e., the stars in galaxies at distances not exceeding the bar semimajor axis are consistent with a standard population. This is possible only if intermediate-age stars leave the bar and supplement the stellar population of the inner part of the disk (or the circumnuclear region).

We thus conclude that the deficit of intermediate-age stars in galactic bars is due to the fact that stars that form in the bar leave it within a few rotations. This may be due to the different trajectories displayed by young and old stars in the bar. The motion of stars in the gravitational potential of a bar will be considered in more detail in a future study.

6. CONCLUSIONS

(1) The distribution of the average surface brightnesses of galactic bars displays two peaks: the first ($B_0 = 21.0^m$/arcsec^2) is characteristic of bars of late-type galaxies and the second ($B_0 = 22.2^m$/arcsec^2) of bars of early-type galaxies. Bars of both types occur in SB0/Ba–SBbc galaxies.

(2) The difference between the average surface brightnesses of the bar and of the galaxy as a whole increases from 1.1^m/arcsec^2 for SB0 galaxies to 2.3^m/arcsec^2 for late-type galaxies.

(3) We have confirmed the previously noted displacement of the color indices of bars in two-color diagrams to the left of the normal color sequence for galaxies.

(4) Bars become bluer with distance from the center: the corresponding points are displaced to the left and upward in two-color diagrams.

(5) The color indices of bars in galaxies of all morphological types suggest that the contribution of intermediate-age [$(1–9) \times 10^9$ yrs] stars is relatively small.

REFERENCES

1. A. T. Kalloglian, Soobshch. Byurak. Obs., Akad. Nauk Arm. SSR **33**, 19 (1963).
2. B. G. Elmegreen and D. M. Elmegreen, Astrophys. J. **288**, 438 (1985).
3. D. M. Elmegreen, B. G. Elmegreen, F. R. Chromey, *et al.*, Astron. J. **111**, 1880 (1996).
4. S. C. Odewahn, Astron. J. **101**, 829 (1991).
5. M. W. Regan and D. M. Elmegreen, Astron. J. **114**, 965 (1997).
6. G. F. Benedict, J. L. Higdon, E. V. Tollestrup, *et al.*, Astron. J. **103**, 757 (1992).
7. A. T. Kalloglian, Soobshch. Byurak. Obs., Akad. Nauk Arm. SSR **25**, 35 (1958).
8. A. C. Phillips, Bull. Am. Astron. Soc. **25**, 1329 (1993).
9. I. I. Pronik, Izv. Krym. Astrofiz. Obs. **45**, 162 (1972).
10. B. G. Elmegreen, D. M. Elmegreen, F. R. Chromey, *et al.*, Astron. J. **111**, 2233 (1996).
11. V. F. Esipov, A. V. Zasov, and G. V. Popravko, Astron. Zh. **70**, 1 (1993) [Astron. Rep. **37**, 1 (1993)].
12. G. Contopoulos, Astron. Astrophys. **81**, 198 (1980).
13. G. Contopoulos and P. Grosbol, Astron. Astrophys. Rev. **1** (3/4), 261 (1989).
14. D. Lynden-Bell, Mon. Not. R. Astron. Soc. **187**, 101 (1979).

15. V. L. Polyachenko and E. V. Polyachenko, Pis'ma Astron. Zh. **20**, 491 (1994) [Astron. Lett. **20**, 416 (1994)].

16. G. de Vaucouleurs, A. de Vaucouleurs, H. G. Corwin, *et al.*, *Third Reference Catalogue of Bright Galaxies* (Springer Verlag, New York, 1991).

17. J. H. Elias, J. A. Frogel, K. Matthews, and G. Neugebauer, Astron. J. **87**, 1029 (1982).

18. R. Buta and K. L. Williams, Astron. J. **109**, 543 (1995).

19. B. P. Artamonov, V. V. Bruevich, and A. S. Gusev, Astron. Zh. **74**, 654 (1997) [Astron. Rep. **41**, 577 (1997)].

20. A. S. Gusev and V. F. Esipov, Astron. Zh. **73**, 357 (1996) [Astron. Rep. **40**, 319 (1996)].

21. B. P. Artamonov, Yu. Yu. Badan, and A. S. Gusev, Astron. Zh. (2000) (in press) [Astron. Rep. (2000) (in press)].

22. B. P. Artamonov, Yu. Yu. Badan, V. V. Bruevich, and A. S. Gusev, Astron. Zh. **76**, 438 (1999) [Astron. Rep. **43**, 377 (1999)].

23. G. F. Benedict, Astron. J. **87**, 76 (1982).

24. W. D. Pence and G. de Vaucouleurs, Astrophys. J. **298**, 560 (1985).

25. R. B. Larson and B. M. Tinsley, Astrophys. J. **219**, 46 (1978).

26. M. Fioc and B. Rocca-Volmerange, Astron. Astrophys. **326**, 950 (1997).

27. G. Worthey, Astrophys. J., Suppl. Ser. **95**, 107 (1994).

28. A. Bressan, F. Fagotto, G. Bertelli, and C. Chiosi, Astron. Astrophys., Suppl. Ser. **100**, 647 (1993).

29. R. C. Kennicutt, Jr., Astrophys. J. **272**, 54 (1983).

30. R. C. Kennicutt, Jr., P. Tamblyn, and C. W. Congdon, Astrophys. J. **435**, 22 (1994).

31. A. Sandage, Astron. Astrophys. **161**, 89 (1986).

32. Ch. Einsel, F.-V. Alvensleben, H. Kruger, and K. J. Fricke, Astron. Astrophys. **296**, 347 (1995).

33. A. S. Gusev, Astron. Zh. **75**, 506 (1998) [Astron. Rep. **42**, 446 (1998)].

34. F. Combes and B. G. Elmegreen, Astron. Astrophys. **271**, 391 (1993).

35. D. Friedli and L. Martinet, Astron. Astrophys. **277**, 27 (1993).

36. R. Arsenault, Astron. Astrophys. **217**, 66 (1989).

37. D. Friedli and W. Benz, Astron. Astrophys. **301**, 649 (1995).

38. E. Athanassoula, Mon. Not. R. Astron. Soc. **259**, 345 (1992).

39. F. Combes, in *The Formation and Evolution of Galaxies*, Ed. by C. Munoz-Tunon and F. Sanchez (Cambridge Univ., Cambridge, 1994), p. 317.

40. D. Reynaud and D. Downes, Astron. Astrophys. **337**, 671 (1998).

41. D. Pfenniger and C. Norman, Astrophys. J. **363**, 391 (1990).

Translated by K. Maslennikov

Ring Structures in Orion KL

L. I. Matveenko[1], P. J. Diamond[2, 3], and D. A. Graham[4]

[1]*Space Research Institute, Russian Academy of Sciences, Profsoyuznaya ul. 84/32, Moscow, 117810 Russia*
[2]*National Radio Astronomical Observatory, Socorro, New Mexico 87801, USA*
[3]*Nuffield Radio Astronomy Observatory, Jodrell Bank, Macclesfield, Cheshire SK11 9DL, UK*
[4]*Max Planck Institute for Radio Astronomy, Auf dem Hügel 69, Bonn, 53121 Germany*
Received October 25, 1999

Abstract—We present the results of studies of the superfine structure of H_2O maser sources in the Orion Nebula. Powerful, low-velocity, compact maser sources are distributed in eight active zones. Highly organized structures in the form of chains of compact components were revealed in two of these, in the molecular cloud OMC-1. The component sizes are ~0.1 AU and their brightness temperatures are $T_b = 10^{12}$–10^{16} K. The structures correspond to tangential sections of concentric rings viewed edge-on. The ring emission is concentrated in the azimuthal plane, decreasing the probability of their discovery. The formation of protostars is accompanied by the development of accretion disks and bipolar flows, with associated H_2O maser emission. The accretion disks are in the stage of fragmentation into protoplanetary rings. In a Keplerian approximation, the protostars have low masses, possibly evidence for instability of the systems. Supermaser emission of the rings is probably triggered by precession of the accretion disk. The molecular cloud's radial velocity is $V_{LSR} = 7.74$ km/s and its optical depth is $\tau \approx 5$. The emission from components with velocities within the maser window is additionally amplified. The components' emission is linearly polarized via anisotropic pumping. © 2000 MAIK "Nauka/Interperiodica".

1. INTRODUCTION

Galactic gas and dust complexes are unique cosmic laboratories with a wide spectrum of physical conditions. Gravitational instabilities in such complexes lead to the formation of local active accretion zones containing protostars in the gravitational contraction phase. Compact regions with enhanced electron density are embedded in ionized HII regions. Each of these regions is a very young area around a recently born hot star. Physical and chemical reactions underway in the active zones lead to the formation of both simple and complex molecules. Maser sources are associated with such compact regions. The only unclear point is their exact location: within the HII region or just outside it. However, it is clear that masers are somehow connected with star-formation processes and are connected with dynamically unstable systems.

When stellar wind impacts gas at rest, a shock wave is formed. The temperature and density of the gas are much higher behind the shock front, promoting the formation and dissociation of molecules, as well as chemical and collisional pumping of masers. These processes are accompanied by strong OH and H_2O maser emission [1, 2]. Maser sources are probably associated with HII regions, as demonstrated by the coincidence of maser velocities with velocities of zones of HII derived from hydrogen recombination lines. Such compact regions have ages of about 10^4 years, testifying to their connection with hot, young stars and the associated maser sources.

It is extremely important to determine which region in a protostellar configuration is responsible for maser emission. This region could be located either in the outer layers of the protostar itself or in nearby gas and dust structures; i.e., the maser sources could be associated not directly with the protostars themselves but with ambient gas and dust. Planets and comets form in this medium. The densest massive clumps probably contract into planets early enough not to be blown out into interstellar space, whereas less massive clumps are accelerated and leave the star's gravitational sphere [3, 4]. However, this process can be accompanied by the formation of an accretion disk and protoplanetary rings [5, 6]. An important task in modern astrophysics is to detect these phases and to determine whether they characterize the formation of protostars and protoplanetary systems. One unique gas and dust complex is the Orion Nebula, which we investigate here.

2. H_2O MASER SOURCES IN THE ORION NEBULA

Maser emission accompanies star-formation processes and is a sensitive indicator of phenomena in active zones. Strong water-vapor maser emission occurs in lines corresponding to the 6_{16}–5_{23} rotational transitions ($f = 22235.08$ MHz, $\lambda = 1.35$ cm). Studies of the fine structure of such zones in their water-vapor line emission are most informative. At the distance to the Orion Nebula, 500 pc, 1 AU corresponds to 2 mas. Thus,

the necessary angular resolution at 1.35 cm wavelength can be achieved using radio interferometers with baselines of several thousand kilometers.

The Orion Nebula was already a primary target for studies in water-vapor lines in the first VLBI experiments, including experiments with high angular resolution on the intercontinental Simeiz–Haystack baseline ($\varphi_f = 0.36$ mas) [7, 8]. Bright, compact H_2O maser sources were revealed. Further studies with global VLBI arrays showed that the H_2O maser sources were concentrated in eight active zones, with sizes up to 2×10^3 AU (Fig. 1) [9]. The strongest sources have H_2O flux densities $F \geq 10^3$ Jy; their sizes do not exceed 0.5 AU, and their velocities are from –8 to +20 km/s. These components are presumably dense maser clouds embedded in a low-velocity flow. The velocity of the flow is $V = 18$ km/s, and it can be up to 10^{14}–2×10^{17} cm in size [10]. The bipolar flow occurs in position angle –30°, and the coordinates of the velocity centroid are

$$R.A. = 05^h32^m46^s.8 \pm 0^s.1,$$
$$DEC = -05°24'27'' \pm 2'' \ (1950.0).$$

The activity center is between two IR sources—the core of Orion KL (IRc4) and IRc2—but is closer to the second. The luminosity of IRc2 is $(10^4-10^5)L_\odot$. The centroid's velocity in the local standard of rest is $V_{LSR} = 10$ km/s. The source's mass-loss rate reaches $(10^{-2}-10^{-4})M_\odot$/yr, the density of matter in the stellar wind decreases as R^{-2}, and the lifetime of the source is 10^3–10^4 yrs.

A high-velocity flow containing components with velocities $V = (30-100)$ km/s is also observed in the Orion Nebula. This high-velocity flow is a factor of 1.5–2 longer than the low-velocity flow. The object BN is probably the source of the high-velocity flow; its mass-loss rate is $M > 10^{-5} M_\odot$/yr [10].

The active zones are characterized by strong outbursts of H_2O maser emission, whose nature and "trigger mechanism" are not yet understood. This phenomenon was first observed on June 6, 1970, in the gas and dust complex W 49 (an object at a distance of 14 kpc) [7]. The radio flux density in one spectral component increased by more than an order of magnitude in less than five minutes, reaching $F = 10^5$ Jy, and then persisted at the new flux level. Such a rapid flux change testifies to the small size of the radio-emitting region (~0.5 AU). Measurements on the Simeiz–Haystack baseline two days later showed that the size of the emitting region did not exceed 1–2 AU, and its brightness temperature was $T_b \approx 10^{16}$ K [8].

A second case of a strong H_2O outburst was observed in the Orion Nebula. Enhanced activity in a spectral feature at radial velocity $V = 8$ km/s persisted in 1979–1987 [5, 11–13]. The flux densities in the H_2O maser outbursts reached $F \geq 10^6$ Jy; however, taking the source distances into account, they were considerably less powerful than the outburst in W49. We obtained obser-
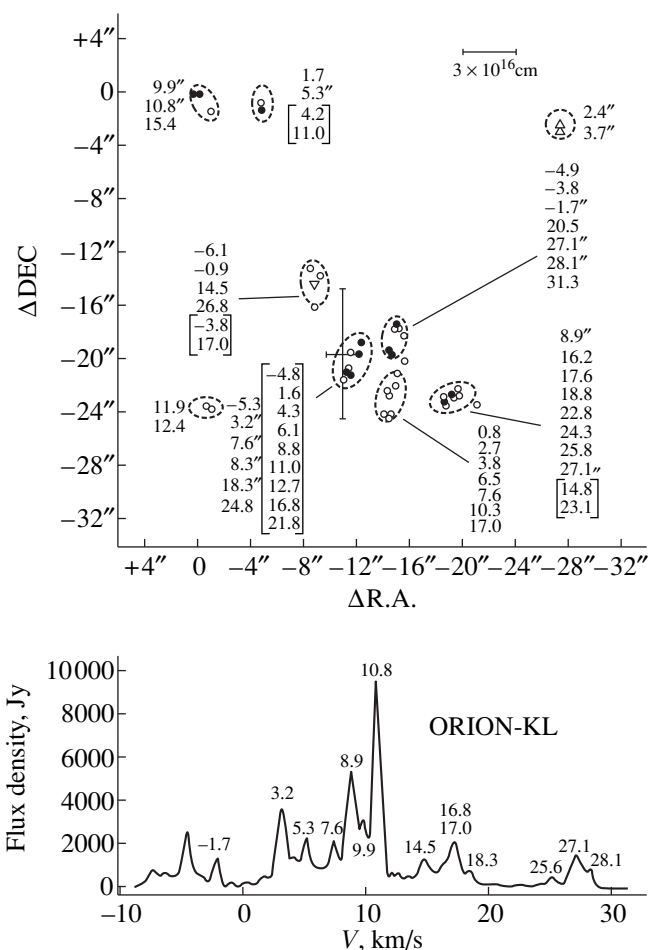
Fig. 1. Spectrum and distribution of H_2O maser sources in active zones of the Orion Nebula. The coordinate origin corresponds to [9] R.A. $= 05^h32^m47^s.58 \pm 0^s.02$, DEC $= -05°24'09''.3 \pm 0''.5$ (1950.0).

vations of this remarkable event in Orion over the entire period of its development. Below, we present the results of our studies.

3. THE REGION OF H_2O SUPERMASER EMISSION

The radiation of the supermaser sources in Orion was characterized by unusually high linear polarization, $P > 60\%$ [11–14]. The outbursts (intervals of enhanced emission) sometimes lasted as long as several months, though one of the outbursts lasted no more than one day [15]. The coordinates of the $V = 8$ km/s supermaser source were measured with the Very Large Array (VLA) [13]:

$$R.A. = 05^h32^m46^s.65 \pm 0^s.01,$$
$$DEC = -05°24'29''.8 \pm 0''.1 \ (1950.0)$$

or, for epoch 2000.0:

R.A. $= 05^h35^m14\overset{s}{.}118 \pm 0\overset{s}{.}01$,

DEC $= -05°22'36''.34 \pm 0''.1$ (2000.0).

These coordinates were later improved using further VLA observations [16] and a quasar in the vicinity, 0529+075, as a reference source:

R.A. $= 05^h35^m14\overset{s}{.}121 \pm 0\overset{s}{.}003$,

DEC $= -05°22'36''.27 \pm 0''.05$ (2000.0).

The field where the supermaser outburst occurred was studied earlier in [17]. Within the measurement errors, compact sources were found at this position, with radial velocities in October–December 1976 equal to $V = 6.7$ and $V = 7.6$ km/s and flux densities $F = 400$ and $F = 1300$ Jy, respectively. Their coordinates were

R.A. $= 05^h32^m46\overset{s}{.}70 \pm 0\overset{s}{.}05$,

DEC $= -05°24'27''.9 \pm 1''.0$ (1950.0) ($V = 6.7$ km/s),

R.A. $= 05^h32^m46\overset{s}{.}68 \pm 0\overset{s}{.}10$,

DEC $= -05°24'29''.3 \pm 1''.5$ (1950.0) ($V = 7.6$ km/s).

The systematic measurement errors for these data can be as high as $2''$ in both coordinates.

Measurements in February 1977 [9] showed that the flux densities for the $V = 6.5$ and $V = 7.6$ km/s sources were $F = 240$ and 1800 Jy at the following coordinates:

R.A. $= 05^h32^m46\overset{s}{.}5639 \pm 0\overset{s}{.}0005$,

DEC $= -05°24'30''.19 \pm 0''.15$ (1950.0) ($V = 6.5$ km/s),

R.A. $= 05^h32^m46\overset{s}{.}7678 \pm 0\overset{s}{.}0005$,

DEC $= -05°24'28''.57 \pm 0''.04$ (1950.0) ($V = 7.6$ km/s).

Here, the systematic errors were reduced to $0\overset{s}{.}02$ and $0''.5$, respectively, in right ascension and declination.

The spatial structure of the supermaser-outburst region was studied at an early stage of the activity, on September 25, 1979, on the Simeiz–Pushchino baseline (the width of the interference fringes was $\varphi_f \approx 3$ mas). At that time, the flux density of the H_2O maser emission was $F = 0.5 \times 10^6$ Jy, and the line's radial velocity was $V \approx 8$ km/s. The line profile was Gaussian, with a low-velocity "tail." Most of the emission was from a com-

pact core at the end of an elongated component 2.5 AU in length, extended approximately east–west. The size of the core was 0.5 mas, or 0.25 AU. The radial velocities of the components were $V = 8.1$ and $V = 7.5$ km/s, and the corresponding brightness temperatures were $T_b > 10^{15}$ and $T_b = 10^{14}$ K [5, 18]. A similar structure was detected on the Green Bank–Haystack and Simeiz–Effelsberg baselines on November 16, 1979 [19]. By that time, the outburst's flux density had reached $F = 1.7 \times 10^6$ Jy. The core size did not exceed 0.36 AU, and its brightness temperature reached $T_b \approx 10^{16}$ K. The extended region was 1.6 AU in size, with a brightness temperature $T_b = 7 \times 10^{14}$ K. The components' emission showed unusually high linear polarization, $P > 80\%$ [20–22].

Further studies showed that the active supermaser region was highly structured, forming an elongated chain of bright compact sources, with the velocities gradually changing from one component to another [5]. The polarization of each source shows a characteristic orientation, which also gradually changed along the chain [5, 14]. The source brightnesses sometimes changed appreciably with time, but their relative positions and velocities were virtually constant. The brightness variations of the individual sources were not correlated with each other.

A high-resolution study of the nebula using a global VLBI array was carried out in October 1985. As in earlier studies, a single feature with a low-velocity "tail" dominated in the spectrum. This feature's radial velocity was $V = 7.81$ km/s, its width was $\Delta V = 0.63$ km/s, and the peak density of its radio emission was $F_0 = 2.2 \times 10^6$ Jy. The degree of polarization at the line center reached $P_0 = 74\%$ with polarization position angle $\chi = -23°$. The measurements confirmed the strong structural organization, with a four-link chain (groups A–D) extended nearly east–west. The synthesized beam was 0.3×1.1 mas. The chain's total length was 8.2 AU.

Table 1 presents the relative positions of the bright regions ΔR in AU. Their radial velocities gradually decrease toward lower right ascensions, from $V = 8.05$ to $V = 6.45$ km/s. Their brightnesses are in the range $B_{peak} = (1–140)$ kJy/beam. In addition, fainter compact components of the E group with emission not exceeding 40 and 50 Jy/beam are observed at $V = 8.8$ and 8.7 km/s, 2.35 and 2.3 AU from the relative zero. Including these components, the total length of the chain is 10.5 AU. Each of the groups contains fine structure [23].

Figure 2 shows the positions and brightnesses of the compact components in each region. The diameters of the circles are presented on a logarithmic scale and represent brightness $B = 1.07 \times 10^{0.132d}$ kJy/beam. The brightest source has $B_{max} = 10^6$ Jy/beam and diameter $d = 22$ units. The compact sources are 0.1 AU in size, and their brightness temperatures are $T_b = (10^{15}–10^{17})$ K. Table 1 gives the radial velocities V for the components in each group, the ranges ΔV of the velocities of com-

Table 1. Parameters of groups of components

Parameter	E	D	A	B	C
ΔR, AU	2.3	0	−2.34	−5.15	−8.52
V, km/s	8.7–8.8	7.7–8.8	6.8–8.1	6.13–6.83	6.13–6.76
ΔV, km/s	0.1	1.05	1.27	0.70	0.63
V_0, km/s	8.75	8.22	7.43	6.40	6.40
V_{max}, km/s	8.75	8.05	7.46	6.56	6.45
B_{peak}, kJy/beam	0.05	90	140	1.1	1.0
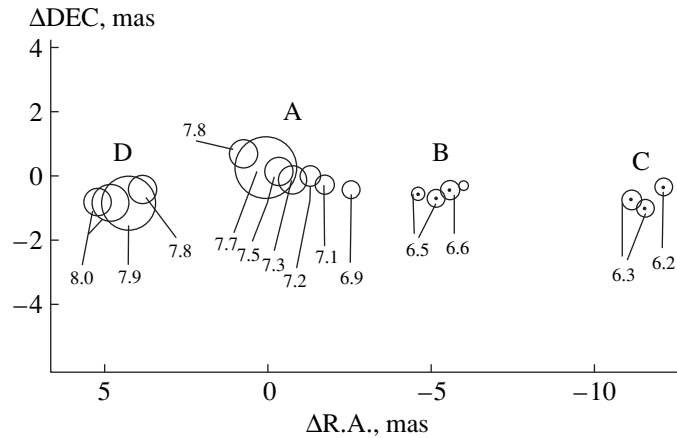
Fig. 2. Fine structure of regions of supermaser emission.
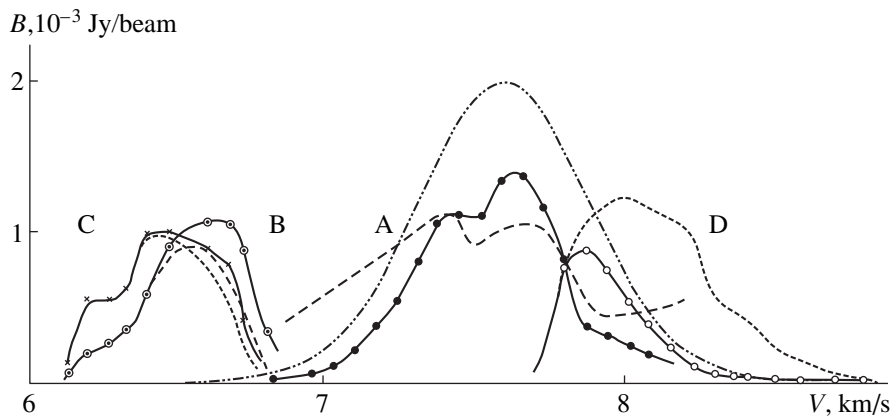
Fig. 3. Brightness distribution in the supermaser regions as a function of velocity (solid curves). The dashed curves are brightnesses corrected for amplification in the maser cloud. Groups A and D are a factor of 100 brighter than groups B and C. The dot–dash curve is the maser amplification by the clouds.

pact components, the value V_0 corresponding to the profile center, and the position of the maximum V_{max}.

Table 2 and Figure 3 present the distributions of the peak brightnesses for the components in each group (in kJy/beam) with radial velocity V. As noted above, the brightnesses of the E-group components are relatively low, and they are not shown in this figure. The brightnesses of components in groups A and D are two orders of magnitude higher than those in groups B and C. The brightnesses for these latter two groups are nearly the same, ~1 kJy/beam. The radial velocities for groups B and C are also close: 6.64 and 6.46 km/s, respectively. The velocities of groups A and D are higher by ~1 km/s: 7.56 and 7.87 km/s, respectively. The velocities of groups A and D differ by 0.31 km/s, and their brightnesses differ by a factor of 1.6. Thus, we note a correlation between the brightesses and relative velocities for the groups.

The different brightnesses of the groups of components can be explained by amplification of their radia-

tion in a maser cloud whose velocity is close to those for groups A and D. The H_2O maser line profile width is determined by the kinetic temperature T_k of the emitting region and is given by

$$\Delta f \approx 3.73 T_k^{0.5} \text{ kHz.}$$

When $T_k \approx 100$ K, the window width is ~40 kHz, or 0.54 km/s. The profile width for a line associated with the maser cloud depends not only on the kinetic temperature but also on differential motions and the amplification regime. In one case, the profile might become broader and, in another, narrower. Let us consider a Gaussian line profile with full width at half maximum 50 kHz (0.67 km/s). The corresponding profile is shown in Fig. 3 as a dot–dashed curve. The apparent brightness of the components in this case is

$$T_b = T_0[1 + e^{\tau_0} e^{-(\Delta V/0.4)^2}],$$

Table 2. Component brightnesses, B, kJy/beam

V, km/s	D		A		B		C		G
6.13	–		–	–	0.06	0.06	0.13	0.13	1
6.20	–		–	–	0.19	0.19	0.56	0.56	1
6.27	–		–	–	0.24	0.24	0.45	0.45	1
6.34	–		–	–	0.35	0.35	0.62	0.62	1
6.41	–		–	–	0.59	0.58	1.00	0.98	1.02
6.48	–		–	–	0.90	0.84	1.00	0.93	1.07
6.62	–		–	–	1.08	0.9	0.88	0.73	1.2
6.69	–		–	–	1.10	0.6	0.79	0.44	1.8
6.76	–		–	–	0.88	0.3	0.40	0.14	2.8
6.83	–		2.00	0.53	0.30	0.08	0.00	0.00	3.8
6.97	–		4.40	0.34	–	–	–	–	13
7.04	–	–	10	0.5					20
7.11	–	–	20	0.7					28
7.18	–	–	39	0.87					45
7.25	–	–	53	0.88					60
7.32	–	–	80	1.08					74
7.39	–	–	105	1.11					95
7.46	–	–	111	1.01					110
7.53	–	–	110	0.91					121
7.60	–	–	135	1.05					128
7.67	–	–	136	1.1					124
7.74	19.0	0.16	117	1.0					116
7.81	74.0	0.78	80	0.84					95
7.88	88.0	1.17	36	0.48					75
7.95	75	1.25	30	0.5					60
8.02	52	1.16	22	0.49					45
8.09	39	1.3	–	–					30
8.16	22	1.1	–	–					20
8.23	9.6	0.74	–	–					13
8.30	4.5	0.64	–	–					7
8.37	2.5	0.5	–	–					5
8.40	1.3	0.4	–	–					3.3
8.51	0.3	0.18	–	–					1.7
8.58	0.25	0.2	–	–					1.3
8.65	0.08	0.07	–	–					1.1
8.72	0.08	0.08	–	–					1.06
8.79	0.04	0.04	–	–					1.02

where τ_0 is the optical depth at the middle of the window, at V_0, and $\Delta V = V_i - V_0$ is the relative velocity. The velocities of the structure under consideration are from 6 to 9 km/s, so that they extend significantly beyond the maser line profile, and the amplification of the groups' brightnesses should be nonuniform.

Suppose that the brightness temperatures of the groups of components before amplification correspond to $B_0 = 1$ kJy/beam. Groups A and D have maximum brightnesses, with a brightness ratio equal to 1.62. It follows that the radial velocity of the cloud (line profile) is close to the velocity of the A components and equal to $V_0 = 7.6$ km/s. In this case, the velocities of groups relative to the middle of the window are $\Delta V_A = -0.14$, $\Delta V_D = +0.45$, $\Delta V_B = -1.04$, $\Delta V_C = -1.15$, and $\Delta V_E = +1.15$ km/s. The maximum brightness, equal to

140×10^3 Jy/beam, is shown by group A at the velocity corresponding to the middle of the window. Here, the amplification is a factor of 140, and the optical depth of the amplifying cloud can be as high as $\tau_0 \approx 5$ in the unsaturated regime. The velocities for groups B and C are fairly far from the line center, and amplification $G(v)$ can affect only the high-velocity parts of their profiles. The brightness amplification factor for groups B, C, and E does not exceed 1.004, and their apparent brightnesses correspond to those of the maser sources themselves. The group profiles corrected for amplification in the maser cloud are shown by the dashed curves in Fig. 3 and are presented in the right column of Table 2 for each of the groups. Significant changes are found for the profiles of groups A and D. In group A, the contribution of the peripheral region is substantial, whereas, in group D, we have a significant contribution at high velocities. The slight dip in the group-A profile is due to the nonuniform brightness distribution for the fine structure. The velocities of group-A components are (6.85–8.1) km/s, with mean velocity 7.46 km/s. Group D components are observed at velocities of (7.7–8.8) km/s, with mean velocity 8.05 km/s.

Model of the supermaser region. The maser-emitting region is an electrically neutral medium—cool molecular gas—so that highly organized structures such as parallel filaments cannot be due to magnetic fields. However, they can appear under the action of gravitational forces. An accretion disk is a typical structural component in the formation of a protostar. In this case, the observed chain of bright components could be an accretion disk splitting into separate rings. Each of the bright compact maser sources corresponds to a tangential section of a ring observed edge-on. The optical depth τ is maximum in this direction (Fig. 4). The observed velocity of the source will correspond to the longitudinal component of the rotational velocity for its incoming part. Consequently, the velocity distribution along the chain will be determined by the disk's Keplerian rotation. The ring geometry and the angular dependence of the optical depth lead to directed emission. The ratio of the source length l to the cross section of its incoming part Δr determines the directivity of the emission. The ring's emission is concentrated in the azimuthal plane. In the elevation plane, the emission will be limited to the angle $\varphi = \Delta r/l$ radians and can essentially be detected only when the plane of the ring is oriented toward the observer. Thus, the directivity of the ring's emission is $\Omega \approx 2\pi\Delta r/l$ ster.

In this model, disk precession could trigger supermaser radiation [20, 23]. The period of apparent high ring emission corresponds to the disk plane being oriented towards the observer. Thus, the activity should be periodic, with its period determined by the angular velocity of precession. The angular velocity of precession can be either higher than, or comparable to, the disk's rotational velocity (rapid precession, as opposed to the slow, "pure" precession observed for a regularly
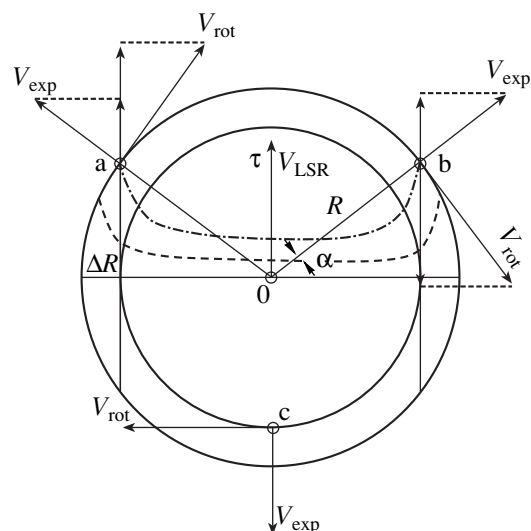
Fig. 4. Schematic presentation of the ring maser source observed edge-on. The points a and b are inputs of maser sources in the tangential direction; point c is the central source. The dashed and dot–dash curves correspond to the optical depths for ring thicknesses of 0.1 and 0.2R, respectively.

activated, rapidly rotating solid disk) [24, 25]. The protostar–accretion disk (protoplanetary ring) system is in the formation stage and, in principle, is nonstationary, but not a solid disk.

Protoplanetary rings are precursors of planets. At this stage, a ring is a torus consisting of a mixture of gas, dust particles, and ice at a temperature of ~100 K in Keplerian motion around the protostar [26]. Infrared radiation sublimates the ice grains, and molecules of water vapor are blown away by stellar wind and radiation pressure. As a result, the outer side of the ring is surrounded by a halo of water-vapor molecules, as is observed in comets. The rate at which the molecules are blown out is determined by the wind's kinetic energy and the radiation pressure. In addition, IR radiation, similar to stellar wind, can be a source of maser pumping. Thus, the halo is an "expanding" maser ring whose emission is concentrated in the azimuthal plane. Pumping can also result from material from the ambient medium falling onto the accretion disk.

The distribution of ice particles and the conditions for sublimation and excitation of the molecules in the ring are nonuniform. Accordingly, the pattern of emission in the azimuthal plane is jagged, and the source's observed brightness will change due to rotation of the ring. The emission patterns of each ring are independent, so no correlation is observed in the brightness changes of the sources. The depth of the "cuts" in the emission pattern, the width of fringes in the azimuthal plane, and the high brightness temperatures of the components testify that the maser regime is either unsaturated or only partially saturated. In this case, the brightness temperature is $T_b \approx T_s(e^\tau - 1)$, and slight changes

of the optical depth, $\Delta\tau = 1$–2, will lead to significant changes in the brightness and "jaggedness" of the emission pattern. The duration of an "outburst" will be determined by the ring's rotational velocity and the characteristic width of the fringes in the azimuthal plane.

The observed chain of components corresponds to one side of the rings (disk). Their symmetrical opposite side has not been detected. This could be an effect of amplification of the emission from the sources in the maser cloud situated in front of the ring structure. Only parts of the structure with radial velocities close to that of the cloud are amplified. On the opposite side of the ring, the radial component of the rotation velocity has the opposite sign, so that it leaves the maser window. In this way, the emission from the opposite side of the ring is not amplified and remains below the detection threshold. In this case, they go beyond the signal detection band.

To derive the system's kinematics, we must know its velocity in the local standard of rest, in order to identify it with a particular location along the line of sight. In the direction toward the object of interest, there is an ionized HII region: the Orion Nebula, with a dense molecular cloud behind it. The molecular density in the cloud is $N_{H_2} \approx 2 \times 10^5$ cm^{-3}. These structures are separated by a thin "sandwiched" layer of dense, cool gas with $N_{H_2} \approx 10^5$ cm^{-3} and $T \approx 50$ K, confined between the ionization front and shock front [27, 28]. The radial velocity of the sandwiched layer in the local standard of rest is 9.7 km/s.

The HII region is ~1 pc in size and contains a star cluster, the Trapezium, whose ultraviolet radiation ionizes the surrounding gas. The velocity of these stars in the local standard of rest is –(12–14) km/s. Stellar wind and radiation pressure blow out the ionized gas, forming an empty cavity around the star cluster. The distant part of the ionized gas recedes from us toward the molecular cloud with a velocity of 1 km/s, whereas the nearer part approaches with a velocity of –5 km/s. The mean radial velocity of the ionized gas along the line of sight derived from recombination lines is $V = -(2$–$3)$ km/s. The electron density near the Trapezium stars is $N_e \approx 2 \times 10^4$ cm^{-3}. Individual compact clouds have $N_e = 5 \times 10^4$–10^5 cm^{-3}, and the electron temperature is $T_e \approx 10^4$ K [27].

The dense molecular cloud extends over 10^{18} cm. It contains a core: the KL nebula, or the object OMC-1. It is assumed that the core includes IR, H_2O, and OH maser sources. The radius of the core does not exceed 10^{17} cm; the density of hydrogen molecules is $N_{H_2} > 10^7$ cm^{-3}. The core's radial velocity in the local standard of rest is $V_{LSR} = 8$ km/s. The velocities of the OH source in right- and left-circular polarization ($V_{LSR} = 7.1$ and 8.6 km/s, respectively) correspond to a magnetic field of 3 mG [27]. The source's radial velocity is $V = 7.85$ km/s. Outside the dense molecular cloud, there is cool neutral gas with $T = 15$ K and a particle concentration of ~2000 atoms/cm^3. The radial velocities of the gaseous and stellar components in Orion could be sig-

nificantly different, making it difficult to estimate the velocity of the system of supermaser emission.

Judging from the coincidence of the molecular-line velocities, the supermaser structure is probably in the core of Orion KL. Thus, the part of the molecular cloud situated in front of the maser sources is the "amplifier." The structure of the supermaser sources indicates that the radial velocity is $V_{LSR} = 7.6$ km/s; improved data yielded the refined value $V_{LSR} = 7.74$ km/s (see below). The velocities of the H_2O and OH maser sources virtually coincide; their slight difference may be due to differential motions in the regions under investigation.

In a stationary model, the rotational velocity of the rings is Keplerian:

$$RV^2 = (M + m)G,$$

where M is the mass of the star, m the mass of the ring, and G the gravitational constant. The mass of the ring should be of order a planetary mass; i.e., $m \ll M$. The chains of components can be represented as

$$(R_0 + \Delta R_i)(V_0 + \Delta V_i)^2 = MG.$$

Table 1 presents the relative velocities ΔV_i and positions ΔR_i of compact components. We have used these values to compute models. We can obtain a reasonable mass for the protostar when the protostar's velocity is negative. For a protostar velocity of $V_0 = -3$ km/s, these data correspond to $R_0 = 19$ AU and $M = 2.6\ M_\odot$. The radius of the inner ring is $R_{min} = 19$ AU, and the mass of the outer ring is $R_{max} = 27.5$ AU; their rotational velocities are $V_{rot} = 11.2$ and $V_{rot} = 9.4$ km/s, respectively.

Thus, a steady-state model is plausible only for negative system velocities. If the system's velocity is coincident with the velocity of the ambient medium, it must be located in the HII region ($V = -3$ km/s); alternatively, the system could be located in the KL nebula, but then the velocity of the protostar does not agree with the nebula's velocity. Increasing the protostar velocity lowers the component radial velocities and protostar mass below reasonable limits. As a limiting case, we can adopt $V_0 = 0$ km/s, which leads to a mass for the star $M = (0.7$–$1.2)\ M_\odot$ at $R = (10$–$16)$ AU. Higher velocities for the star are not realistic for steady-state models.

Let us suppose that the supermaser structure is near a shock front and has velocity $V_{LSR} = 5$ km/s. Then the component velocities do not exceed 1–3 km/s and the protostar mass is $M \approx 0.01\ M_\odot$. However, the apparent velocities of the maser components can be significantly influenced by stellar wind and radiation pressure that blow out the water vapor. For a maser source, this is equivalent to expansion of the ring. Taking into account the radial velocity of the rings, we arrive at the following model parameters. The mass of the central star is $M \approx (0.2$–$0.5)\ M_\odot$. The radius of the inner ring is $R \approx 6$ AU, its rotational velocity is $V_{rot} \approx 5$ km/s, and its expansion velocity is $V_{exp} \approx 3.8$ km/s [5].

In an unsaturated regime, the brightness temperatures of the sources are $T_b \cong T_c(e^\tau - 1)$ K. For a kinetic

Flux density, kJy
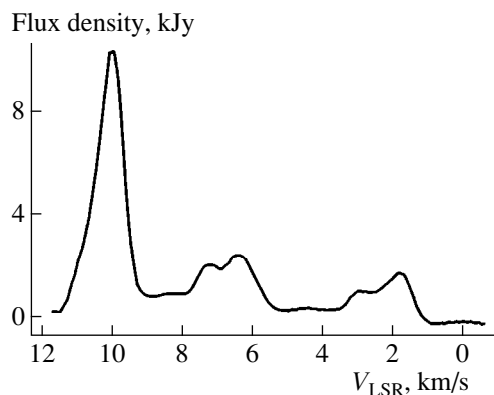
Fig. 5. Spectrum of the maser emission on May 26, 1995, during the "quiescent" period.

gas temperature $T_k \approx 100$ K and brightness temperature $T_b = 10^{12}$–10^{14} K, the optical depth of the maser source is $\tau \approx 23$–28. Additional enhancement of the brightness temperature occurs when the velocities of the source and cloud, with optical depth $\tau \approx 5$, coincide.

4. STRUCTURE OF THE SUPERMASER REGION IN "QUIESCENCE"

An image of concentric rings observed edge-on should contain, in addition to bright compact components, extended regions, low-brightness bridges corre-sponding to the front and back parts of the rings. These could not be detected because of the high brightness of the supermaser components. To try to distinguish these extended structures, we observed the rings on May 26, 1995, after the decline of the activity. At that time, the maximum emission, $F = 9 \times 10^3$ Jy, corresponded to a spectral feature at $V = 10$ km/s (Fig. 5). At the superma-ser-emission velocities, the flux densities did not exceed $F \approx 10^3$ Jy ($V = 8.2$ km/s), $F \approx 2 \times 10^3$ Jy ($V = 7.2$ km/s), and $F \approx 2.3 \times 10^3$ Jy ($V = 6.4$ km/s). We obtained polarization-sensitive measurements with the Very Long Baseline Array of the National Radio Astron-omy Observatory. The resulting angular resolution (syn-thesized beam) was 0.3×0.7 mas. The large dynamical range obtained (~40 dB) enabled us to measure a wide range of brightnesses in the compact components. The velocity resolution was $\Delta V = 0.1$ km/s, and the sensitiv-ity was sufficient to measure components with bright-ness $B \approx 1$ Jy/beam, or $T_b \approx 10^{10}$ K.

Figure 6 shows the dependence of the source corre-lated flux densities on baseline length, which provides evidence for a complicated spatial structure and the pres-ence of compact components. Extended components (≥ 0.7 mas) were resolved on baselines $\leq 350 \times 10^6$ λ. On longer baselines, $B \leq 640 \times 10^6$ λ, corresponding to interference fringe widths $\varphi_f \geq 0.3$ mas, the correlated fluxes slowly decline and remain at the level $F_{cor} = 150$ Jy. This means that the brightness temperature of the com-

Correlated flux, kJy
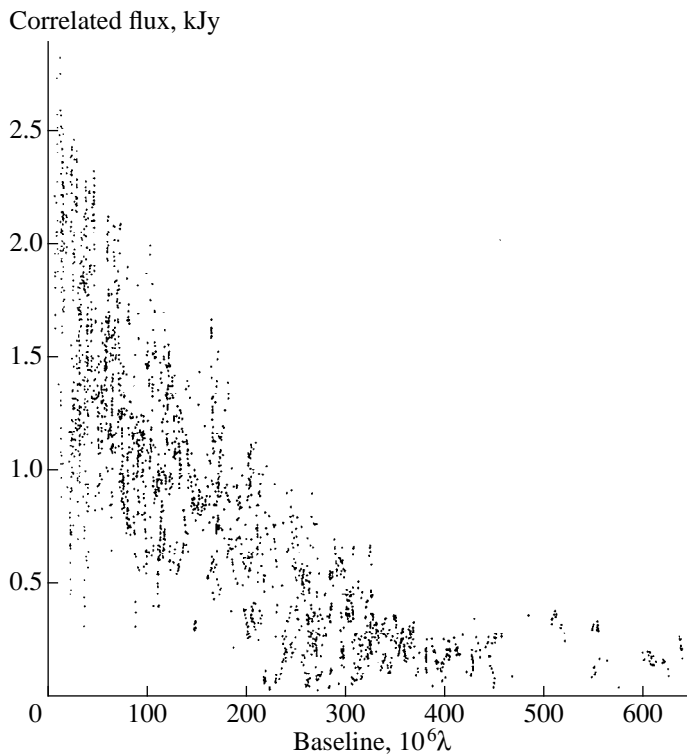
Fig. 6. Dependence of the Orion Nebula's correlated flux on baseline.
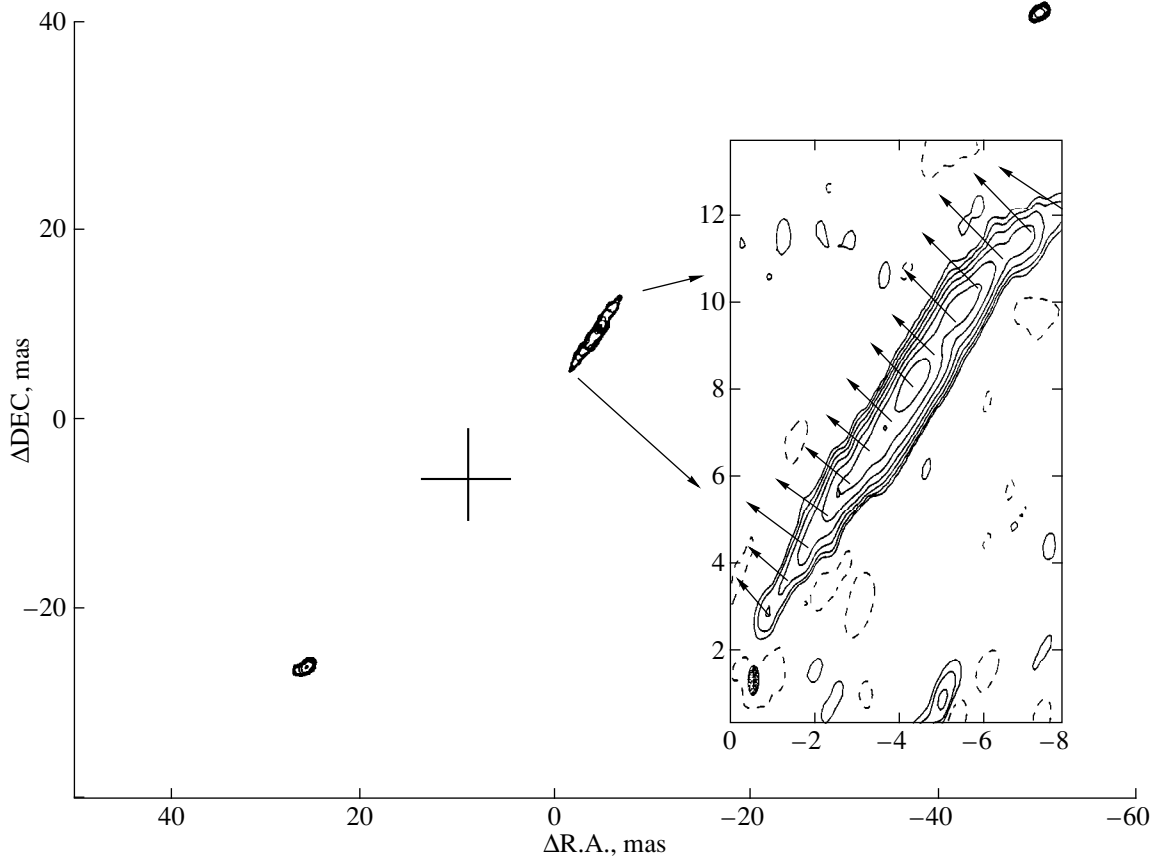
Fig. 7. Structure of the region of supermaser emission during "quiescence." The jet is shown magnified to the right. The arrows indicate polarized radiation. One milliarcsecond corresponds to polarization $P = 25\%$; for clarity, the polarization vectors have been rotated by $90°$.

pact components ($\varphi_f = 0.13$ mas, visibility $\gamma = 0.5$) is $T_b \approx 5 \times 10^{13}$ K.

Identification of the studied region. One of the most important problems in studies of fine structure and dynamics is aligning images at different epochs and determining the relative positions between features in different images. First, we had to identify the field under investigation and fix its coordinates with high precision. For this purpose, after the standard procedure of phase referencing the interferometric signals and determining the position of the array beam from calibration observations of quasars, we were able to identify a standard reference source in our field. At the calculated position of the supermaser emission [17], at velocities $\Delta V = 5$–8 km/s, we observed a structure consisting of three components. One of these was shifted relative to the central one by 6 mas in position angle PA = $-38°$, and the other, by 4 mas in PA = $163°$. We adopted the central, bright source as the reference. It has a simple emission profile. The peak line flux density was $F = 1300$ Jy; its width, $\Delta V = 1.2$ km/s; and its radial velocity, $V = 6.2$ km/s. The coordinates of the reference feature were subsequently improved using the rates of the radio interferometric signals. The reference

source is ~$3''$ to the southeast of the supermaser region [13, 17]:

$$\Delta R.A. = -879.1 \pm 8.4 \text{ mas} = -0\overset{s}{.}5885 \text{ and}$$
$$\Delta DEC = -3163.1 \pm 59.6 \text{ mas}.$$

Structure of the region. We searched for features in a ±150-mas field around the region of supermaser emission. We observed a complex structure, consisting of southeastern and northwestern compact components and a jet (Fig. 7). Their radiation is linearly polarized. The parameters of the components are collected in Table 3, which presents their velocities V in km/s, distances R in AU, structural position angles relative to the center PA in degrees, degrees of polarization P in percent, and polarization position angles χ in degrees. Table 3 gives the peak flux densities F in Jy and brightness temperatures T_b in units of 10^{12} K. The component velocities are within the window for the maser cloud. It is possible that their brightness temperatures (Table 3) have been additionally amplified, as for the supermaser emission. Assuming that the components had equal brightness temperatures prior to amplification and that the window width is 50 kHz, we obtain a radial velocity for the cloud $V_{LSR} = 7.74 \pm 0.03$ km/s. The component

velocities relative to the middle of the window, ΔV, are also presented in Table 3. The component brightness temperatures are

$$T_b = 2.89 \times 10^{12} e^{-\{\Delta V/0.4\}^2} \text{ K}.$$

The amplification by the cloud in the middle of the window is a factor of ~ 200 ($\tau \approx 5$). In this case, the intrinsic brightnesses of the structures do not exceed $T_b \approx 10^{10}$ K. Structures with such brightness temperatures are below the detection threshold and can be observed only in the presence of additional amplification. This structure can be understood as a bipolar outflow, typical of "protostar–accretion" disk systems [6].

Polarization of the radiation. The structure discussed above is characterized by a high level of polarization. Figure 7 shows the distribution of the polarization along the jet axis. For increased clarity, the polarization position angle χ has been rotated by $90°$. The degree of polarization is uniform in the central part of the jet ($P = 33\%$), and increases toward the ends. In the southeastern part, $P = 45\%$; and in the northwestern part, $P = 50\%$. χ gradually changes from $-40°$ to $-45°$. The generally accepted mechanism for the linear polarization of H_2O maser emission supposes normal Zeeman splitting: strong interaction and a saturated regime [29]. The magnetic field should be of the order of 50 G, and the degree of polarization should not exceed a few tens of percent.

On the other hand, degrees of polarization as high as 100% can occur in an unsaturated regime, in the presence of pumping anisotropies >10% [30–32]. This is precisely the case for the model of concentric rings and bipolar flows under consideration. Isotropic infrared or collisional pumping from the protostar becomes anisotropic with respect to the ring. The ring's cross section is small compared to the distance to the pumping source, and the wave front (flow) is virtually flat. Anisotropic pumping will also occur in interactions of the bipolar flow of particles with the ambient medium. In this case, the direction of the polarization will be determined by the direction of the flow. The bipolar jet and compact components constituting the bipolar flow were ejected from a common source, and the velocity vectors of the components should be directed toward this source [23].

The observed orientations of the components' polarization differ from the expected behavior. This could be due to passage of the radiation through the ionized medium of the HII region. The rotation of the polarization plane is described by the rotation measure RM:

$$\text{RM [rad/m}^2] = 8.1 \times 10^5 N_e \text{ [cm}^3] \, B \text{ [G]} \, l \text{ [pc]}.$$

The electron density in the H II region under consideration is $N_e \approx 10^3$ cm^{-3}, the magnetic field is $B = (10–50) \times 10^{-6}$ G, and its extent along the line of sight is $l \approx 0.6$ pc. Therefore, we have for the rotation measure $5 \times 10^3 < \text{RM} < 25 \times 10^3$ rad/m^2, and the rotation angle at 1.35 cm is 1–5 rad.

The jet is a flow of particles with its axis aligned along the velocity of their motion. The observed difference between the direction of the jet (PA = $-33°$) and the polarization plane ($\chi = -45°$) is $12° \pm 180°n$, where n is an integer, which is within the possible range expected for Faraday rotation estimated above. Let us assume that the intrinsic χ value is oriented along the position angle of the jet, $-33°$. The observed difference should be conserved within the studied field. Accordingly, we will rotate the observed polarization position angles by $12°$ and assume that this enables us to infer the direction of the velocity vectors of the components.

These vectors will intersect at the activity center: the protostar and accretion disk. The center is marked with a cross in the figure. Within the errors ($\Delta\text{R.A.} = \pm 0.\!^s003$ and $\Delta\text{DEC} = \pm 50$ mas), this point is at the center of the supermaser region. No other structures are coincident with this point within the errors. Analysis of the structure shows that the activity center is probably the origin of the jet. It is natural to suppose that this center coincides with the system of concentric rings associated with the supermaser emission. Thus, they represent a common system.

Table 3 shows that the degree of polarization of the components decreases with distance from the activity center. This is probably due to a loss of anisotropy in the particle flow as it propagates outward. The flow loses anisotropy due to collisional interactions between the particles and the ambient medium, which decelerates them and makes their motion more chaotic. The observed differences in the directions of the component motions from the center could be due to precession of the rotation axis of the "star–accretion disk" system. Water-vapor molecules can be present both in the surrounding medium and in the injected matter. Distant components correspond to compact clumps and provide evidence for nonstationary matter injection. On

Table 3. Parameters of components of the supermaser region

Parameter	Components		
	southeastern	jet	northwestern
V, km/s	7.95	7.66	7.45
ΔV, km/s	0.21	-0.08	-0.29
R, AU	23	0	28
PA, degrees	132	-33	-55
P, %	45	32	12.5
χ, degrees	-53.5 ± 1.5	-45.3 ± 0.5	-54.5 ± 2.5
F, Jy	485	1060	317
T_b, 10^{12} K	2.2	2.8	1.7
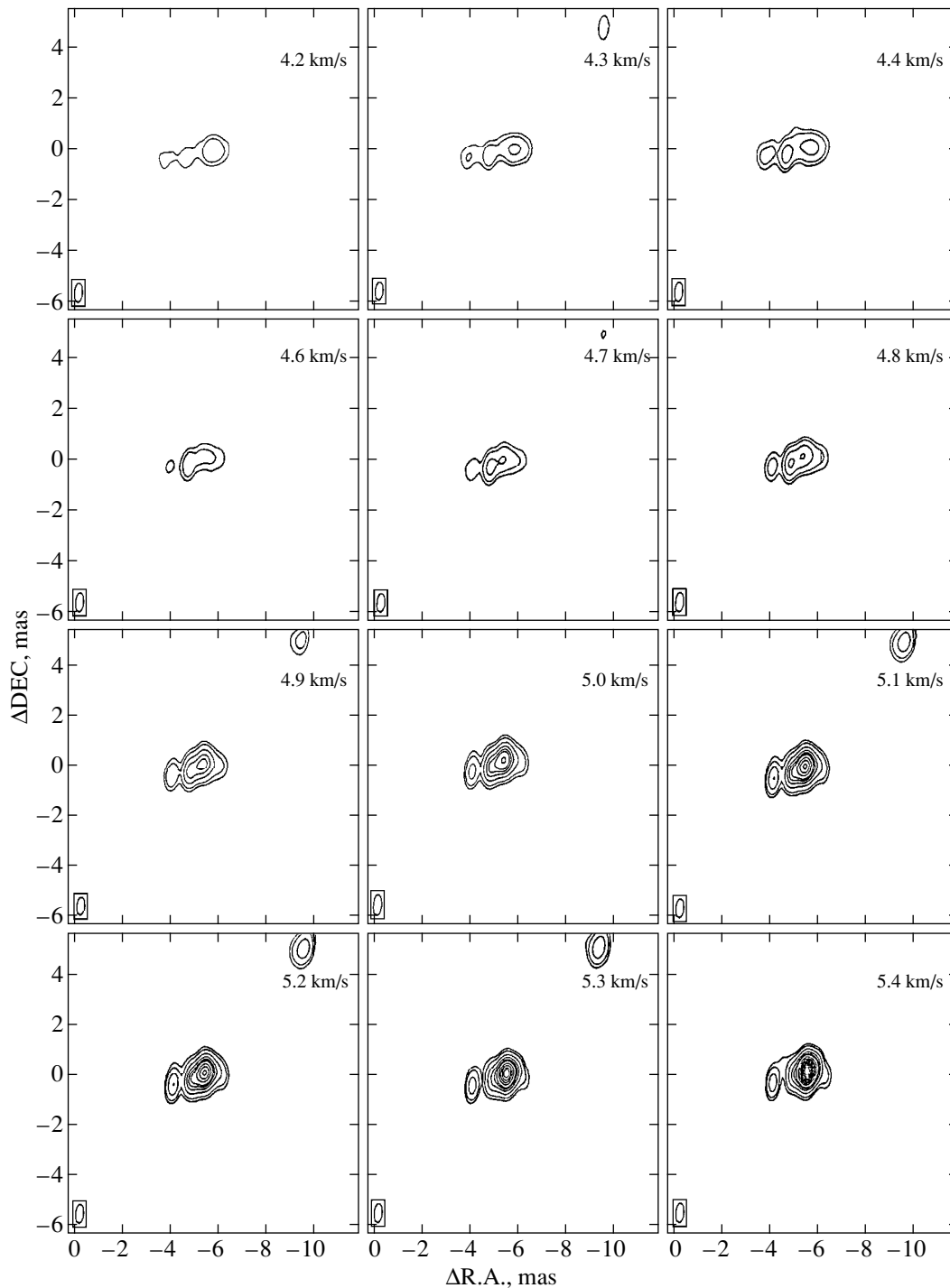
Fig. 8. Brightness distribution of the H_2O maser emission in the active region of the Orion Nebula. The coordinate origin is R.A. =

$05^h35^m14\overset{s}{.}118$, DEC = $-05°22'36\overset{''}{.}34$ (2000.0). The synthesized beams are shown in the bottom left corners. F_{peak} = 750 Jy/beam.
For velocities V = 4.2–4.4 and 9.6–9.8 km/s, levels of 0.225 (1, 2, 5, 10, 15, 20, 30, 40, 50, 60, 70, 80, 90, 100) Jy/beam are given;
for V = 4.6–5.1, 9.4, and 9.5 km/s, the levels are 0.750 (1–100) Jy/beam; for V = 5.2–5.4 km/s, the levels are 1.499 (1–100) Jy/beam;
for V = 8.7–9.3 km/s, the levels are 0.375 (1–100) Jy/beam.

the other hand, these components could result from a nonuniform distribution of the water-vapor molecules in the surrounding region. The bipolar jet itself corresponds to a quasistationary flow.

Thus, our studies of H_2O maser emission have led to the discovery in one of the active regions of the Orion Nebula of the KL system, consisting of an accretion disk subdivided into several protoplanetary rings and a
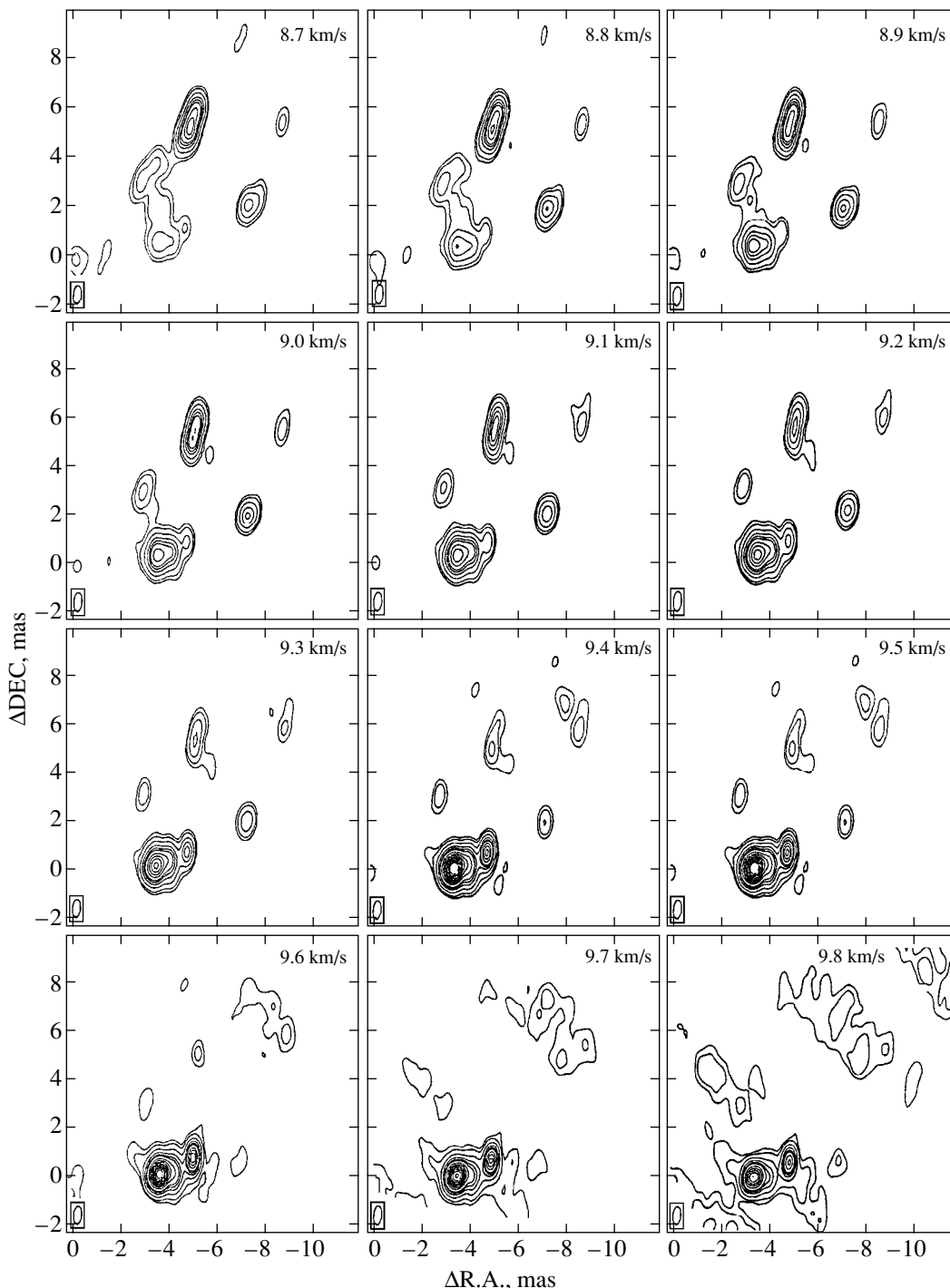
Fig. 8. (Contd.)

bipolar flow. However, is this structure associated with the formation of an accreting star? Our further analysis confirms that this is the case.

5. REGION OF THE REFERENCE SOURCE

We detected several characteristic structures through our analysis of a ±500 mas field around the reference source in the velocity range 0–12 km/s. Figures 8 and 9 show maps for various velocities with $\Delta V = 0.1$ km/s resolution; the synthesized beam was 0.3×0.7 mas oriented in PA = $-5°$.

The ring structure. There is a symmetrical structure in the immediate vicinity of the reference source, at velocities 4.2–5.8 and 9.0–9.8 km/s. It consists of
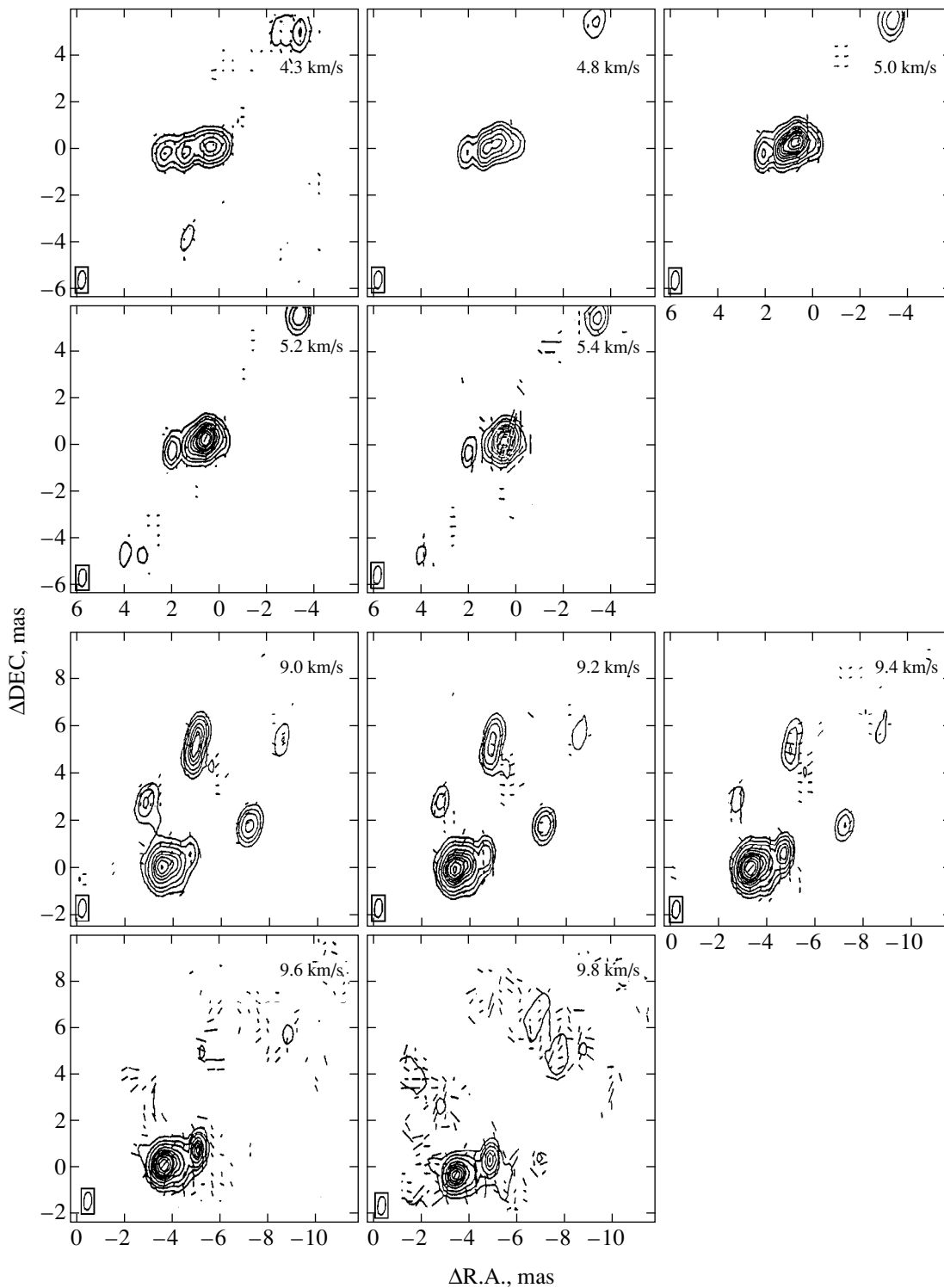
Fig. 9. Brightness distribution of the polarized H$_2$O maser emission in the active region of the Orion Nebula KL. The coordinate origin is R.A. = 05^{h}35^{m}14^s.118, DEC = −05°22′36″.34 (2000.0). F_{peak} = 750 Jy/beam. For the velocity V = 4.3 km/s, the levels are 0.036 (2, 5, 10, 20, 30, 40, 50, 60, 75, 90) Jy/beam. (The sticks correspond to the level and orientation of the polarization, with 1 mas = 125 mJy/beam.) For V = 4.8–5.0 km/s, the levels are 0.215 (2–90) Jy/beam (polarization sticks: 1 mas = 250 mJy/beam); for V = 5.2 km/s, the levels are 0.502 (2–90) Jy/beam (polarization sticks: 1 mas = 1.25 Jy/beam); for V = 5.4 km/s, the levels are 1.435 (2–90) Jy/beam (polarization sticks: 1 mas = 833 mJy/beam); for V = 9.0–9.4 km/s, the levels are 0.718 (1, 2, 5, 10, 15, 20, 30, 40, 50, 60, 70, 80, 90, 100) Jy/beam (polarization sticks: 1 mas = 250 mJy/beam); for V = 9.6–9.8 km/s, the levels are 0.215 (2–90) Jy/beam (polarization sticks: 1 mas = 250 mJy/beam).
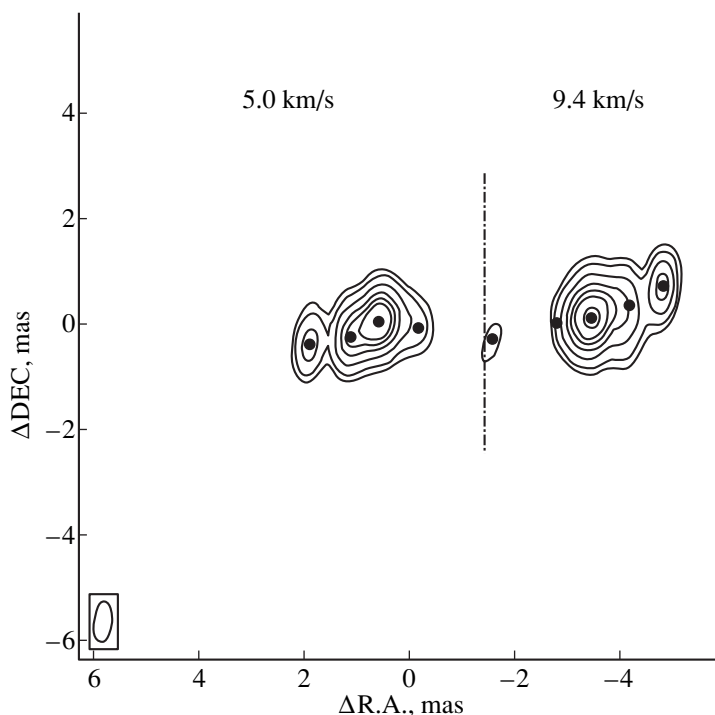
Fig. 10. Brightness distribution in the ring structure with $V_{LSR} = 5.0$ and 9.4 km/s. The central source has $V_{LSR} = 7.7$ km/s and brightness 0.4 Jy/beam. The solid points show compact sources.

two regions, each containing a chain of four compact components. Figure 10 shows a composite of images for velocities 5.0 and 9.4 km/s. The solid circles correspond to compact components. The emission profile widths for each group of components are $\Delta V \approx 0.6$ km/s. Emission from the brightest components of the third group dominates. These components determine the velocities of the eastern and western profiles, $V = 5.25$ and $V = 9.42$ km/s. The north–south brightness sections are comparable to the beam width. The peak values for the profiles are 80 and 28 Jy/beam; and their full widths at half maximum are 0.76 and 0.75 mas, respectively. Corrected for the beam size in a Gaussian approximation, this translates into source sizes of 0.20–0.28 mas, or 0.10–0.14 AU. In this case, the brightnesses of the components in the third group are $B \approx 350$ and $B \approx 160$ Jy/beam, and their brightness temperatures are $T_b = 7 \times 10^{12}$ and $T_b = 6 \times 10^{12}$ K. The planes of the

rings are tilted with respect to each other (Table 4), forming a hat-brim shape. The farther from the center, the greater the tilt, possibly due to a nonsymmetrical external perturbation.

The general orientation of the disk's axis of rotation in the plane of the sky is PA $\approx 8°$. The brightness temperatures of the components of the principal ring (No. 3) are $T_b \sim 5 \times 10^{12}$ K; the brightness temperatures for the remaining components are lower by factors from four to eight. Table 4 presents the distances between pairs of components $2\Delta R$ in AU, their position angles PA in degrees, their rotation velocities V_{rot} and relative velocities ΔV in km/s, their brightnesses B in Jy/beam, and their brightness temperatures T_b in units of 10^{12} K. The components' brightness temperatures are comparatively low. This might be due to a lack of additional amplification in the outer maser cloud, since the veloc-

Table 4. Parameters of components of the ring structure

Ring no.	2R, AU	PA, degrees	V_{rot}, km/s	ΔV, km/s	B, Jy/beam		T_b, 10^{12} K	
					eastern	western	eastern	western
1	3.40	−80	1.85	−0.6	8	11	0.5	0.7
2	2.64	−84	2.11	−0.31	8	7	0.5	0.5
3	2.02	−90	2.41	0.0	80	28	5.0	4.6
4	1.32	−88	2.98	0.55	2	1	0.13	0.06
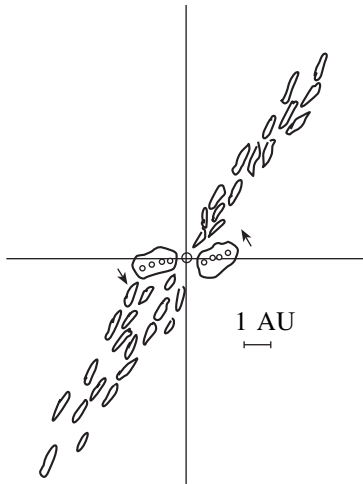
Fig. 11. Schematic representation of the "accretion disk–bipolar flow" structure.

ities of the components are outside the window, $\Delta V > 1.5$ km/s.

In the middle of this structure, at velocities $V = 7.7$–9.0 km/s, there is a faint compact source (Fig. 10) with brightness approximately 0.4 Jy/beam, radial velocity $V_{LSR} \sim 8.4$ km/s, and brightness temperature $T_b \sim 10^9$ K.

Model of the ring source. The brightness temperature of the maser source in the unsaturated regime,

$$T_b(f) = |T_s|(e^{\tau(f)} - 1) + T_F e^{\tau(f)},$$

is determined by the excitation temperature $|T_s|$ and the background (base) temperature T_F. The excitation temperature,

$$T_s = (\tau_q^{-1} + \tau_r^{-1})/[(T_r\tau_r)^{-1} + (T_k\tau_q)^{-1}],$$

depends on the time scales for collisional excitation, τ_q, and radiatively induced transitions, τ_r. In optically thin clouds, the energy density of intrinsic molecular line emission is low, and the background radiation dominates. At higher particle concentrations, the role of radiative transitions becomes less important, and the excitation temperature T_s approaches the kinetic temperature [33]. Let us suppose that the kinetic temperature is $T_k = 100$ K. For a maser source corresponding to a tangential section of the ring, the background temperature will be lower than the kinetic temperature, so that $T_b(f) \cong |T_s|e^{\tau(f)}$.

The maser's brightness and apparent size depend on its optical depth τ, and, in our case, they will be determined by its incoming part, where the optical depth reaches its maximum value. The radial velocities of the components are determined by the projected velocities of their incoming parts (points "a" and "b" in Fig. 4), while their brightnesses are determined by the optical depth $\tau(f)$. The projected velocity of the incoming part of the source is a combination of the projected veloci-

ties of rotation and of outward motion. The observations indicate that the source sizes do not exceed 0.14 AU. The optical depth and radial velocity depend on the geometrical thickness of the ring. The ring's thickness is larger than the apparent source size but is smaller than the distance between rings ($0.1 < \Delta R < 0.2$ AU, Table 4). The dashed and dot–dashed curves in Fig. 4 show the change in the relative optical depth (geometrical size) when the ring thickness changes from $0.1R$ to $0.2R$. The optical depth of the maser depends on the window width and the differential velocity along the line of sight. The total velocity range along the line of sight is 0.36 km/s and does not exceed the width of the maser line's window, $\Delta V \approx 0.5$ km/s.

The central component (point "c" in Fig. 4) probably corresponds to radiation of the protostar amplified by the front of the ring. Its brightness temperature, $T_b(f) \cong T_F e^{\tau(f)}$, depends on the background—the temperature of the star. The star's radiation has a continuous spectrum. Therefore, the line profile and velocity will be determined by the front of the ring.

Let us consider a ring with rotational velocity V_{rot} and expansion velocity V_{exp} (Fig. 4). The velocity of the central star in the local standard of rest is V_{LSR}. According to Fig. 4, the radial velocities at the incoming parts of the (a) eastern, (b) western, and (c) central maser sources are

$$V_{a\|} = +V_{exp}\sin\alpha + V_{rot}\cos\alpha + V_{LSR} = 5.25 \text{ km/s},$$

$$V_{b\|} = +V_{exp}\sin\alpha - V_{rot}\cos\alpha + V_{LSR} = 9.42 \text{ km/s},$$

$$V_{c\|} = -V_{exp} + V_{LSR} = 8.3 \text{ km/s}.$$

From these relations, $V_{rot} = -2.09/\cos\alpha$. For a ring diameter $2R = 2.02$ AU (ring No. 3, Table 1) and thickness $\Delta R = 0.15$ AU, $\alpha \approx 30°$ and $V_{rot} = -2.4$ km/s. In accordance with the notation of Fig. 4, the minus sign indicates counterclockwise rotation of the ring. From these parameters, the mass of the central star for Keplerian motion is $M = 0.007\, M_\odot$.

The brightness temperatures of the components of the other rings are lower than those of ring No. 3 by factors of four to ten, making it difficult to distinguish their emission in the integrated profile and determine their velocities. Therefore, we calculated predicted rotational velocities for the rings in a Keplerian approximation, based on their diameters relative to the third group. Table 4 gives the ring diameters $2R$ in AU, their orientations PA in degrees, and their velocities V_{rot} in km/s.

Let us determine the radial velocity of the system. It follows from the above equations that

$$V_{LSR} + V_{exp}\sin\alpha = 7.35 \text{ km/s}.$$

For a stationary system, $V_{exp} = 0$ km/s. The protostar's radial velocity in the local standard of rest is $V_{LSR} = 7.35$ km/s, which differs from that of the molecular cloud by -0.39 km/s. This difference may be due to the radial velocity of the ring; i.e., the system is
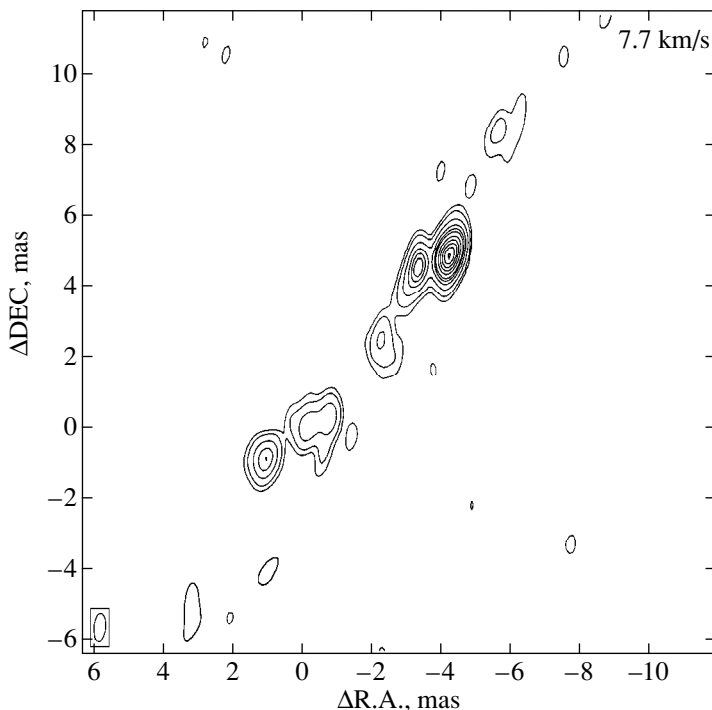
Fig. 12. Map of the bipolar flow ($V = 7.7$ km/s).

dynamically nonstationary, the ring's expansion velocity (Fig. 4) is $V_{exp} = -0.64$ km/s, and $V_{LSR} = 7.66$ km/s.

We will estimate the sizes of the compact sources based on changes in their optical depths. The maximum brightness temperature of a source, $T_{max} \approx T_s e^{\tau_0}$, is determined by the optical depth at the line center, τ_0. The brightness temperature of source No. 3 is $T_b = 5 \times 10^{12}$ K (Table 4), corresponding to $\tau_0 \approx 25$. The source size Q is defined as that at the half-maximum of the peak brightness temperature, corresponding to a reduction in the optical depth by $\Delta\tau = 0.7$, or $\Delta\tau/\tau_0 \approx 0.03$ in relative units. It follows from Fig. 4 that, for a ring thickness of $0.15R$, its maximum geometrical size (the optical depth $\tau_{0r} = R\sin 30°$) is equal to 0.5 AU (ring No. 3, Table 4). To the first approximation, the relation between the size of the source and the maser optical depth is $\Delta r \approx \Delta\tau \tan 30°$, and the size of the source is $\Delta r \approx 0.01$ AU. High brightness temperature will lead to partial saturation of the maser and smoothing of the brightness peak and therefore to increased angular size. A similar effect will take place if the edge of the ring is indistinct. However, even if we take the effective size of the source to be 0.05 AU, or 0.1 mas, close to the observed value, its brightness temperature will be $T_b \geq 10^{14}$ K, so that $\tau_0 \geq 28$.

The brightness of the central source (c) is 0.3 Jy/beam, corresponding to $T_b = 10^9$ K. The star's brightness temperature is $T_b \sim 10^4$ K, and the maser amplification in the front of the ring will be $\sim 10^5$, so that $\tau = 11.5$. In this

case, the emission of the ring itself will correspond to 10^7 K, significantly below the detection threshold. Let us estimate the optical depth of the central part of the ring from its geometrical size. From measurements in tangential sections of the ring, $\tau \sim 30$. The ratio of the geometrical values is 6.7, and the optical depth in the central part of the ring is $\tau \approx 4.5$, which differs from our previous estimate by about a factor of 2.5. The velocity of the central source is within the amplification window for the outer medium, with optical depth $\tau \approx 5$. In this case, the two estimates nearly coincide. Thus, the brightness of the bridge between the two compact components is below the detection threshold.

The emission from the ring structure is linearly polarized. Polarization maps for various velocities are presented in Fig. 9. Table 5 presents the fluxes F in Jy, degrees of polarization P in percent, and polarization position angles χ in degrees. The maximum degree of polarization is as high as 2.8% at velocity 5.4 km/s, with $\chi = -18°$. The size of the emitting region is 0.18 AU.

The bipolar flow. The ring structure discussed above is supplemented by a bipolar flow, directed in PA $= -34°$, at an angle of $-42°$ relative to the rotation axis of the disk. The flows are detectable to distances of 10 AU. The brightness temperatures of individual components in the flow are $T_b \leq 10^{10}$ K. The velocities of the northwestern and southeastern components are $V = 7.4$–8.2 km/s and $V = 6.1$–7.2 km/s, respectively. The velocities of the maser components differ from each other by only 1.2 km/s. The small difference between
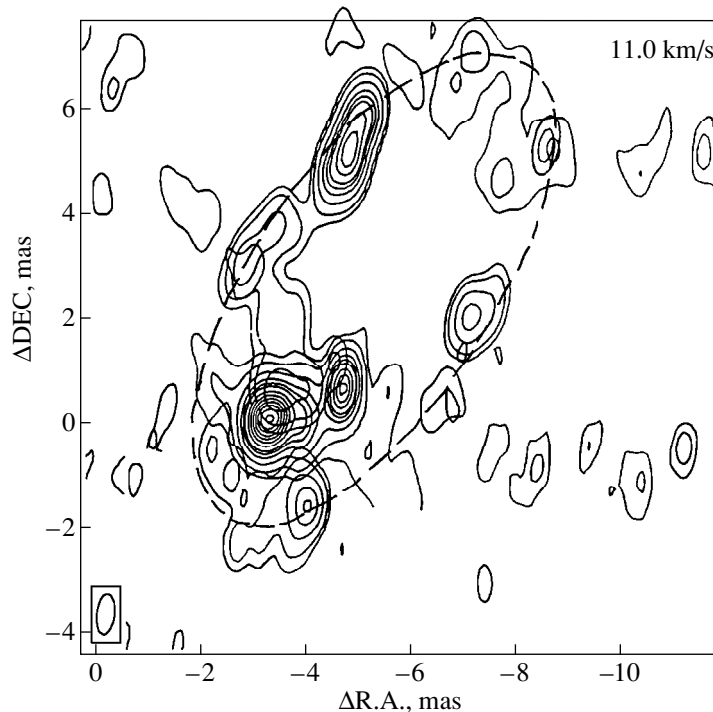
Fig. 13. Elliptical structure in the region of the reference source: superposition of maps for velocities $V = 8.7$, 9.7, and 11.0 km/s.

the velocities of the bipolar flows could indicate that the flows lie nearly in the plane of the sky, so that their radial projections differ only slightly. On the other hand, the observed velocity $V = 0.6$ km/s may actually refer to the velocity of water-vapor molecules in the ambient medium that are accelerated by the flows. The radial velocity of the bipolar flow is 7.2 km/s, which coincides within the errors with the velocity of the ring structure, $V_{LSR} = 7.35$ km/s, as well as with that of the central protostar, $V = 7.7$ km/s (Fig. 10).

6. THE ELLIPTICAL STRUCTURE

In addition to the systems discussed above, an elliptical structure was revealed near the reference source (Fig. 8). Figure 13 presents a map for $V = 11$ km/s, with images for $V = 8.6$ and $V = 9.6$ km/s superimposed. In the lower part, the western part of the ring system is projected onto the elliptical structure. The major and minor axes of

the ellipse are 7 and 2.5 AU. The ellipse's major axis lies in position angle $-35°$. The ellipse may be a ring inclined $70°$ to the plane of the sky. The brightnesses of this structure is not high, so that only its brightest fragments are visible. Their brightness temperatures reach $T_b \approx 10^{10}$ K. Pieces of the structure can be followed at velocities from 6.1 to 11.2 km/s (Fig. 8). A slight velocity gradient is observed, from $V = 6.3$ km/s in the northeastern part to $V = 9.8$ km/s in the southwestern part. This suggests expansion at 1.7 km/s (the radial projection of the velocity), or, taking into account the structure's inclination, $V_{exp} = 2$ km/s. The radial velocity of the system as a whole is ~ 8 km/s. The velocities of individual fragments are within the window for the molecular cloud's maser line, $V \approx 7.74$ km/s, so that their brightness temperatures are enhanced to $T_b \approx 10^{12}$ K. This elliptical structure could also be connected with an expanding elliptical envelope [34].

Table 5. Component emission characteristics

Eastern part				Western part			
V, km/s	F, Jy	P, %	$-\chi$, degrees	V, km/s	F, Jy	P, %	$-\chi$, degrees
5.2	72	1.3	18				
5.3	120	0.7	40	9.4	20	0.5	45
5.4	72	2.8	18	9.5	32	<1.0	45
5.7				9.7	20	<1.0	40

7. CONCLUSIONS

Strong water-vapor maser emission accompanies the formation of protostellar structures in gas and dust complexes. In our investigation of the superfine structure of active regions in the Orion Nebula with angular resolution, corresponding to 0.1 AU, we have obtained the following results.

(1) Stars are formed collectively. The compact maser sources are concentrated in eight active zones. Their velocities are $V_{LSR} = (0-10)$ km/s, and their H_2O F line flux densities are $F > 1$ kJy.

(2) In two zones separated by a projected distance of 1500 AU toward the core of the molecular cloud, we have detected highly organized structures—chains of compact components, an elliptical structure, and bipolar flows of particles.

(3) The chains of compact components correspond to tangential sections of protoplanetary rings observed edge-on. The apparent size of the sources is ~0.1 AU.

(4) The maser ring is from a halo of water vapor surrounding the protoplanetary ring. The sublimation of ice crystals produces water vapor, which is then blown out by stellar wind and radiation pressure. These factors are also sources of molecular excitation in collisional and radiative pumping. Pumping due to matter from the ambient medium falling onto the accretion disk is also possible.

(5) The emission from the "expanding" maser ring is concentrated in the azimuthal plane and is observed only if this plane is oriented toward the observer. The nonuniform distribution of water-vapor molecules results in nonuniform emission: a jagged "pattern," observed as source variability. The variability time scale is determined by the rate of rotation and the fringe widths.

(6) The brightness temperatures of the compact sources, protoplanetary ring structures, are $T_b = 10^{12}$–10^{16} K, while those of individual features in the bipolar flows and elliptical structure are $T_b \leq 10^{10}$ K.

(7) The radial velocity of the molecular cloud in front of these structures is $V = 7.74$ km/s, and its optical depth is $\tau \sim 5$. Emission from structures with velocities within the window of the cloud's maser line are amplified by approximately two orders of magnitude, leading to the supermaser emission of components at velocities $V \approx 7.5$–8.0 km/s.

(8) Judging from the coincidence of their radial velocities, both zones are located in the dense core of the cool molecular cloud (the object OMC-1, or Orion KL).

(9) The formation of protostars is accompanied by accretion disks and bipolar flows. The accretion disks we have detected are in the stage of splitting into protoplanetary rings. These structures are directly connected to the strong water-vapor maser emission. Collisions of particle flows with molecules of water vapor excite the maser emission.

(10) The polarization of the maser emission from the various structures is due to anisotropic pumping.

(11) The period of enhanced activity, supermaser emission, could be due to a change in the orientation of the accretion disk plane (precession). This suggests the possibility of periodic supermaser activity determined by the precession period.

(12) The system of rings determining the supermaser emission have $V_{rot} = 10.8$–9.3 km/s, $R = 23$–31 AU, $M = 3M_\odot$, and $V_{LSR} = -3$ km/s. If $V_{LSR} = 5$ km/s, the protostar mass is <0.01 $M_\odot$.

(13) In the second zone, the accretion disk is subdivided into four rings. The third ring has $V_{rot} = 2.4$ km/s and $R = 1.01$ AU. For Keplerian motion, the protostar mass is $M \leq 0.007M_\odot$. In the local standard of rest, the protostar's velocity is $V_{LSR} = 7.35$ km/s. The ring structure is observed edge-on, but the planes of the rings do not coincide, resulting in a "hat-brim" effect.

(14) The detected ring structures are observed edge-on. This is a selection effect: only in this case can sufficient optical depth and high brightness be achieved for sources in the tangential directions.

(15) The 7×2.5 AU elliptical structure could be an expanding ring inclined at $70°$ or an elliptical envelope. Its individual components have brightness temperatures $T_b \sim 10^{10}$ K.

(16) An accretion disk and bipolar flows are typical phenomena accompanying the process of protostar formation.

ACKNOWLEDGMENTS

REFERENCES

1. I. S. Shklovskiĭ, Astron. Tsirk., No. 372, 1 (1967).
2. M. M. Litvak, Science **165**, 855 (1969).
3. V. S. Strel'nitskiĭ, Usp. Fiz. Nauk **113**, 463 (1974) [Sov. Phys. Usp. **17**, 507 (1974)].
4. V. S. Strelnitskij, Mon. Not. R. Astron. Soc. **207**, 339 (1984).
5. L. I. Matveenko, Pis'ma Astron. Zh. **7**, 100 (1981) [Sov. Astron. Lett. **7**, 54 (1981)].
6. R. Bachiller, Annu. Rev. Astron. Astrophys. **34**, 111 (1996).
7. B. F. Burke, K. J. Johnston, V. A. Efanov, *et al.*, Astron. Zh. **49**, 465 (1972) [Sov. Astron. **16**, 379 (1972)].
8. B. F. Burke, K. J. Johnston, V. A. Efanov, *et al.*, Radiofizika, No. 5, 799 (1973).
9. R. Genzel, D. Downes, J. M. Moran, *et al.*, Astron. Astrophys. **66**, 13 (1978).
10. R. Genzel, M. J. K. Reid, J. M. Moran, and D. Downes, Astrophys. J. **244**, 884 (1981).

11. Z. Abraham, N. L. Cohen, R. Opher, *et al.*, Astron. Astrophys. Lett. **100**, L10 (1981).

12. Z. Abraham, J. W. S. Vilas Boas, and L. F. Giampo del, Astron. Astrophys. **167**, 311 (1986).

13. G. Garay, J. M. Moran, and A. D. Haschick, Astrophys. J. **338**, 244 (1989).

14. L. I. Matveenko, Pis'ma Astron. Zh. **20**, 456 (1994) [Astron. Lett. **20**, 388 (1994)].

15. Z. Abraham and J. W. S. Vilas Boas, Astron. Astrophys. **290**, 956 (1994).

16. L. J. Greenhill, C. R. Gwinn, C. Schwartz, *et al.*, Preprint No. 4750 (SAO, 1998).

17. R. Genzel and D. Downes, Astron. Astrophys. **61**, 117 (1977).

18. L. I. Matveenko, L. R. Kogan, and V. I. Kostenko, Pis'ma Astron. Zh. **6**, 505 (1980) [Sov. Astron. Lett. **6**, 279 (1980)].

19. L. I. Matveenko, D. M. Moran, and R. Genzel, Pis'ma Astron. Zh. **8**, 711 (1982) [Sov. Astron. Lett. **8**, 382 (1982)].

20. L. I. Matveenko, D. A. Graham, and P. J. Diamond, Pis'ma Astron. Zh. **14**, 1101 (1988) [Sov. Astron. Lett. **14**, 468 (1988)].

21. L. I. Matveenko, A. M. Romanov, L. R. Kogan, *et al.*, Pis'ma Astron. Zh. **9**, 456 (1983) [Sov. Astron. Lett. **9**, 240 (1983)].

22. A. M. Romanov and L. I. Matveenko, Pis'ma Astron. Zh. **10**, 345 (1984) [Sov. Astron. Lett. **10**, 145 (1984)].

23. L. I. Matveenko, P. J. Diamond, and D. A. Graham, Pis'ma Astron. Zh. **24**, 723 (1998) [Astron. Lett. **24**, 623 (1998)].

24. R. P. Feynman, R. B. Leighton, and M. Sands, *The Feynman Lectures on Physics* (Addison-Wesley, Reading, Mass., 1964; Mir, Moscow, 1965).

25. *Classical Mechanics*, Ed. by H. Goldstein (Addison-Wesley, Reading, Mass., 1980).

26. A. J. R. Prentice, Aust. J. Phys. **33**, 623 (1980).

27. *The Orion Complex: A Case Study of Interstellar Matter*, Ed. by C. Goudis (Reidel, Dordrecht, 1982), Vol. 90.

28. *Physics of Thermal Gaseous Nebula*, Ed. by L. H. Aller (Reidel D., Dordrecht, 1984), Vol. 112, p. 226.

29. P. Goldreich, D. A. Keeley, and J. Kwan, Astrophys. J. **179**, 111 (1973).

30. D. A. Varshalovich, Usp. Fiz. Nauk **101**, 369 (1970) [Sov. Phys. Usp. **13**, 429 (1970)].

31. L. R. Western and W. D. Watson, Astrophys. J. **275**, 195 (1983).

32. L. R. Western and W. D. Watson, Astrophys. J. **285**, 158 (1984).

33. S. A. Kaplan and S. B. Pikel'ner, *Physics of the Interstellar Medium* [in Russian] (Nauka, Moscow, 1979), p. 591.

34. L. I. Matveenko, P. J. Diamond, and D. A. Graham, Preprint No. 2015, IKI RAN (Institute for Space Research, Russian Academy of Sciences, Moscow, 1999).

Translated by N. Samus'

Spectral Features of RZ Psc, a Cool Star
with Algol-like Brightness Minima

B. M. Kaminskiĭ, G. U. Kovalchuk, and A. F. Pugach

Main Astronomical Observatory, National Academy of Sciences of Ukraine, Kiev-22, 252650 Ukraine

Received August 23, 1999

Abstract—We have determined the physical (T_{eff}, $\log g$, ζ) and kinematic ($V_e \sin i$, V_r) parameters and abundances for 14 chemical elements in the atmosphere of the "antiflare" variable RZ Psc, using medium-resolution spectra obtained with the Coudé spectrographs of the 6-m telescope of the Special Astrophysical Observatory and the Crimean Astrophysical Observatory 2.6-m Shain telescope. The chemical composition of the star is characterized by a slight metal deficiency; however, the iron and calcium abundances are consistent with the solar values within the errors. We also detected a peculiar dip (depression) of the continuum level near the H_α line. Assuming that this depression and the photospheric H_α line have independent origins, we calculated the hydrogen abundance X in the atmosphere of RZ Psc. The resulting value $X = 0.70$ (of the solar value) implies a relative deficiency of hydrogen. Together with the spatial location of the star, these properties provide evidence that RZ Psc is an evolved star, most likely belonging to population II. © *2000 MAIK "Nauka/Interperiodica"*.

1. INTRODUCTION

RZ Psc belongs to a small group of fast, irregular variable stars with Algol-like brightness minima. All well-studied stars of this type display bright H_α emission. On the basis of these two distinguishing features, the acronym ALIVARS (Algol-Like or Alpha-Line Irregular VARiable Stars) was suggested for this group of stars [1]. This acronym describes the group more clearly and underlines its difference from the wider, but less well defined, group of Herbig Ae/Be stars. There is no fundamental difference between the previously used term "antiflare stars" and the term ALIVARS; in our opinion, however, the new acronym reflects significant properties of this group of stars more adequately.

The following important characteristics served as a basis for distinguishing ALIVARS from Herbig Ae/Be stars.

(1) All ALIVARS display the same characteristic type of variability.

(2) ALIVARS are generally unrelated to young stellar systems and star-forming regions. Many ALIVARS undoubtedly are so-called "isolated" stars [2, 3].

(3) ALIVARS are not main-sequence stars and are located in the zone of giants and stars of higher luminosity in the $\log g - \log T$ diagram [1, 4].

(4) All ALIVARS display a characteristic relationship between the equivalent width of the H_α emission line and effective temperature [5].

(5) Some ALIVARS display weakened Balmer lines; for V351 Ori, a low hydrogen abundance was found [6].

All these properties form a distinct boundary between Herbig Ae/Be stars and ALIVARS and provide grounds to consider ALIVARS an independent group of variables. This conclusion is strengthened by the fact that, as directly indicated by three of the five points above (2, 3, and 5), ALIVARS are evolved stars and thus are not related to Herbig Ae/Be stars, which are commonly considered to be young objects.

Though a typical star with Algol-like brightness dips, RZ Psc was not identified with ALIVARS with regard to its spectral features for a long time, since its spectrum was poorly studied. It was only known that its spectral type was in the range G8–K0 and that there were no bright emission lines in the spectrum.

However, RZ Psc has been very thoroughly studied photometrically [7–10]. In addition to studies of the general character of its brightness and color-index variability, it was established that the brightness–color-index relation for this star is not single-valued. In the initial stages of decay, the color indices increase nearly in accordance with the interstellar reddening law; however, they decrease as the star approaches minimum brightness. For this reason, the color indices in deep minima are close to the unreddened values observed in maximum. Such peculiar curvature in the color–magnitude relation was first detected by Zaĭtseva [11] for UX Ori and later acknowledged as a characteristic property of many ALIVARS.

The hypothesis of circumstellar extinction is in good agreement with the collected photometric and polarimetric observations (see, for example, [3, 12, 13]). The hypothesis of circumstellar dust as applied to RZ Psc is confirmed both by the star's characteristic variability and by the behavior of its colors [10]. It is nearly

Table 1. Observations

Date	Number of spectra: RZ Psc/comparison star	Exposure, min	S/N (near H_α)	Spectrograph	Spectr. wavelength range, nm
Dec. 17, 1991	2/1	30	68	LYNX	500–850
Dec. 20, 1991	2/1	30	44	LYNX	500–850
Aug. 13, 1998	2/2	60	54	SP-14	653–660

universally accepted that, for all ALIVARS, the brightness decay is due to absorption of the intrinsic radiation of the star by a circumstellar envelope, while the curvature of the color relation is a consequence of the scattering of photospheric radiation by circumstellar dust [14, 15].

The rich photometric data for RZ Psc made it possible to investigate the possibility of periodic brightness variations and the presence of a secondary. A periodic component in the brightness variations is frequently observed. It is, however, manifested rather strangely: at times it completely disappears, or the epoch of brightness decay deviates from that for the ephemeris. Some epochs of deep minima ($V > 12^{m}.0$) are consistent with a period of $12^{d}.67$ [8, 9], leading Shevchenko *et al.* [16] to introduce the concepts of marginal "proto-Algol" and "quasi-Algol" binaries, to which they assigned RZ Psc. Quasi-periodic decays are indeed observed in the brightness variations of RZ Psc; however, the suggestion that they are regular contradicts the earlier conclusion of Tsesevich [7] that no period exceeding one day is consistent with the observations. One possible compromise is that deep brightness decays are induced by some periodic process occurring inside the star. The connection between this process and the brightness decays is statistical rather then strict, as for R CrB stars [17, 18].

Here, we study the spectral properties of RZ Psc in order to estimate its physical parameters, which can be used in combination with the rich photometric data available to investigate the origin of the appearance of clumps of circumstellar matter in the line of sight.

2. OBSERVATIONS AND REDUCTION

The observations were made with the 6-m telescope of the Special Astrophysical Observatory and the 2.6-m Shain Telescope of the Crimean Astrophysical Observatory. The LYNX échelle spectrograph was used at the Nasmyth focus of the 6-m telescope, providing spectral resolution ($R \sim 25\,000$) and a wide wavelength range (450–900 nm) [19], which enabled the confident detection of a large number of spectral lines. To study the H_α line, which was not detected by the LYNX spectrograph due to the on–off time ratio for the échelle spectrograms, we observed with the Shain telescope using the SP-14 Coudé CCD spectrograph. A summary of the observations is presented in Table 1.

We carried out the preliminary reduction of the observations, including taking into account noise, instrument constants, and image cutting, using master programs composed by the producers of the spectral equipment. The final processing of the spectra and of individual lines was performed using an unpublished code developed by V.O. Skarzhevskiĭ.

We used a thorium–argon spectrum [20] to linearize the wavelength scale and also to determine the instrumental profiles for both spectrographs. We did not take natural line broadening into account. Since the instrumental profiles for various wavelengths coincided with a Gaussian to within $\pm 2\sigma$ of its width, we used the Gaussian FWHM in pixels when convolving the synthetic spectrum with the instrumental response.

3. DATA ANALYSIS

The high quality of our spectral data and the reduction technique used enabled the identification and measurement of nearly 200 absorption lines. As a result, we were able to derive a number of physical parameters: the temperature and gravitational acceleration of RZ Psc at the photospheric level; the microturbulence, radial, and rotational velocities; and metal abundances. The hydrogen abundance was also estimated.

3.1. Effective Temperature

For stars with solar abundances, T_{eff} determinations based on high-resolution spectra present no special problems. In the case of RZ Psc, however, the situation is complicated by its unknown chemical composition. Since there could be a hydrogen deficiency in RZ Psc, as in other ALIVARS [6], determination of the atmospheric parameters required a self-consistent solution including three independent parameters: T_{eff}, $\log g$, and X. We derived T_{eff} using three different techniques based on an analysis of the color indices, the equivalent widths of temperature-insensitive lines, and the Boltzmann equilibrium.

3.1.1. Colorimetric temperature RZ Psc. The rich photometric data for RZ Psc enabled us to derive a so-called color temperature, implicitly reflected in the $B - V$ and $V - R$ color indices, and tie it to the effective temperature scale. Using 147 brightness measurements in each of the B, V, and R bands made during our many-year observations during the normal state of the star

[21], we determined the average color indices $B - V = 0\overset{m}{.}846 \pm 0\overset{m}{.}008$ and $V - R = 0\overset{m}{.}638 \pm 0\overset{m}{.}007$.

To determine T_{eff}, we used the fact that the color indices RZ Psc were measured under the same conditions—using the same telescope, equipment, and reduction technique—as the B, V, and R magnitudes for 300 unreddened standard stars [22]. T_{eff} values for several dozen G3–K4 stars from this list were determined based on either the curve of growth technique or atmosphere models [23]. We used their color indices and effective temperatures to construct $(B - V)$–T_{eff} and $(V - R)$–T_{eff} relations (Fig. 1), which could then be used to estimate T_{eff}, given known color indices undistorted by interstellar absorption. For temperatures of 4500–5500 K, the temperature errors did not exceed ± 110 K. When both color indices were used simultaneously, the error for the average of the two values did not exceed ± 75 K.

RZ Psc is located at a high Galactic latitude ($b = -34.5°$), in an area where no appreciable absorbing material has been detected. According to [24], no significant interstellar absorption is present in the direction of RZ Psc up to a distance of 2 kpc, so we can use the observed $B - V$ and $V - R$ values directly. The fact that both color indices yield the same temperature supports this approach. If the color indices were appreciably distorted by interstellar absorption, the temperatures determined from the graphs in Fig. 1 would indicate differences due to the selective character of the absorption.

The resulting effective temperature for RZ Psc averaged over the two estimates was $T_1 = 5170 \pm 75$ K. The fact that we are able to use the observed, unreduced color indices indicates that the absorption does not exceed the detection threshold of the photometric technique used rather than that there is no absorption at all. It is quite admissible that the interstellar absorption is on the order of $0\overset{m}{.}02$–$0\overset{m}{.}03$, so the real T_{eff} value is 100–200 K higher.

3.1.2. T_{eff} derived from temperature-insensitive lines.

The idea behind this method was used in the Harvard spectral classification: two lines are selected—one with variable intensity over some temperature interval and one whose intensity is constant over this interval; their intensity ratio depends on temperature. Synthetic spectra provide wide possibilities for the selection of such line pairs within the required wavelength and temperature intervals. Figure 2 presents the iron-line pair Fe I λ 6469.21 (1258) and Fe I λ 6475.63 (206), one of which varies its equivalent width by a factor of more than two when T_{eff} varies by 1000 K, while the other remains nearly constant. For each pair found in this way, we constructed calibration curves based on synthetic spectra calculated for various temperature values. Given the observed intensity ratio, we estimated the effective temperature from these curves.
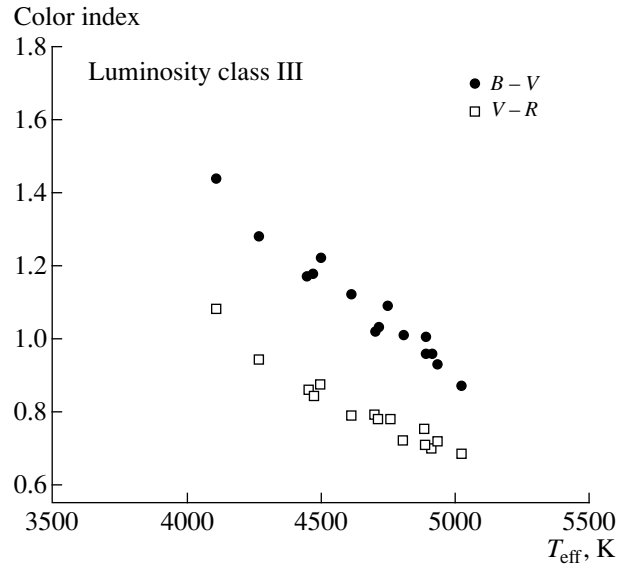
Fig. 1. Dependence of $B - V$ and $V - R$ on T_{eff} used for the photometric temperature determination.
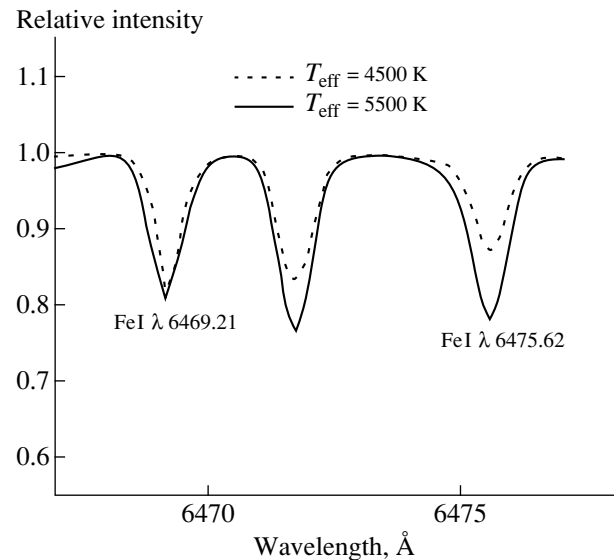
Fig. 2. Dependence of the relative intensities of temperature-insensitive (Fe I λ 6469.21, dots) and temperature-sensitive (Fe I λ 6475.62, solid line) lines on T_{eff}.

We found about 40 temperature-insensitive line pairs in the spectrum of RZ Psc in the interval 4500–5500 K. In Table 2, the lines with low temperature sensitivity and completely temperature-insensitive lines are marked "tm." The average temperature determined using this method is $T_2 = 4810 \pm 200$ K.

3.1.3. Boltzmann equilibrium T_{eff}.

The idea behind this method is that the derived abundance of an element $\log \varepsilon_i$ should not depend on the excitation potential for the lines used. Lines with low excitation potentials χ_i are sensitive to temperature variations. If the calculated

Table 2. Lines used to determine the chemical composition, $V_e \sin i \, T_{eff}$, $\log g$

Element Solar abundance, $\log \varepsilon_\odot$	λ, Å	EV, eV	$\log gf$	$\log \varepsilon$	W_λ, Å	$V_e \sin i$, km/s	Notes*
1	2	3	4	5	6	7	8
Al I	6631.218	4.02	−0.699	−6.1	0.14		
−5.57	6631.809	4.02	−0.549	−	−		
Ba II	6141.713	0.7	−0.159	−9.5	0.22		gr
−9.91							
Ca I	5581.965	2.52	−0.709	−5.4	0.137		gr
−5.68	5588.749	2.53	0.21	−6.3	0.127		
	5590.114	2.52	−0.709	−6.1	0.106		
	5601.277	2.53	0.689	−6.2	0.076		
	5857.451	2.93	0.23	−5.2	0.22		
	5867.562	2.93	−1.519	−5.5	0.032		gr
	6102.723	1.88	−0.889	−4.2	0.475		gr
	6122.217	1.89	−0.409	−5.6	0.293		
	6166.439	2.52	−0.899	−5.4	0.101		gr
	6169.563	2.53	−0.269	−5.5	0.318		
	6439.075	2.53	0.47	−5.1	0.4		
	6462.567	2.52	0.31	−5.2	0.284		
	6471.662	2.53	−0.589	−5.2	0.136		gr
	6493.781	2.52	0.14	−5.1	0.255		
Cr I	4954.807	3.12	−0.309	−6.3	0.048		gr
−6.37	5070.054	2.71	−1.189	−6.6	0.028		
	5204.506	0.94	−0.169	−7.7	0.251		
	5206.037	0.94	0.03	−7.3	0.287		
	5208.419	0.94	0.16	−7.2	0.41		
	5312.871	3.45	−0.469	−6.6	0.036		gr
	5409.772	1.03	−0.719	−6.9	0.026		gr
Cu I	5105.537	1.39	−1.519	−8.6	0.072		
−7.83	5700.237	1.64	−2.309	−8.6	0.076		
Fe I	4957.298	2.85	−0.339	−4.6	0.607		b
−4.50	4957.596	2.81	0.13	−	−		
	4966.087	3.33	−0.819	−4.4	0.192		b
	4967.878	4.19	−0.869	−4.6	0.208		
	4968.703	3.64	−1.709	−	−		b
	4969.916	4.22	−0.739	−4.8	0.173		b
	4970.499	3.64	−1.629	−	−		b
	4973.100	3.96	−0.879	−4.9	0.103		b
	4978.445	3.98	−0.899	−4.6	0.158		
	4985.239	2.87	−1.579	−5.2	0.168		
	4985.554	2.87	−1.579	−	−		b
	4988.945	4.15	−0.819	−5.1	0.115		b
	4993.674	4.21	−1.399	−5.1	0.212		
	4994.129	0.91	−1.399	−	−		b
	5001.862	3.88	0.002	−4.9	0.108		b
	5002.789	3.4	−1.509	−5.0	0.042		
	5004.037	4.21	−1.329	−5.0	0.045		
	5005.699	3.88	−0.339	−4.6	0.384		
	5006.125	2.83	−0.869	−	−		b
	5012.067	0.86	−2.639	−5.0	0.24		b
	5067.151	4.22	−0.889	−4.6	0.076		
	5068.765	2.94	−1.109	−4.9	0.118		

Table 2. (Contd.)

Element Solar abundance, $\log\varepsilon_\odot$	λ, Å	EV, eV	$\log gf$	$\log\varepsilon$	W_λ, Å	$V_e \sin i$, km/s	Notes*
1	2	3	4	5	6	7	8
Fe I	5072.068	4.280	−1.289	−4.4	0.166		b
−4.50	5072.654	4.22	−1.229	−	−		b
	5074.748	4.22	−0.189	−4.6	0.169		b
	5075.156	4.18	−1.579	−	−		b
	5090.767	4.26	−0.389	−4.9	0.137	30	
	5096.981	4.28	−0.579	−4.6	0.135		
	5098.559	3.93	−1.169	−4.9	0.305		b
	5098.703	2.18	−2.099	−	−		b
	5099.075	3.98	−1.459	−	−		b
	5104.029	3.02	−2.799	−4.8	0.090		b
	5104.185	4.18	−1.899	−	−		b
	5104.436	4.28	−1.619	−	−		b
	5107.446	0.99	−3.089	−5.8	0.177		b
	5107.664	1.56	−2.829	−	−		b
	5191.461	3.04	−0.799	−4.4	0.694		b
	5191.351	3.00	−0.659	−	−		b
	5202.335	2.18	−1.559	−5.1	0.175	30	
	5215.187	3.27	−2.249	−5.1	0.139		
	5216.277	1.61	−2.249	−5.1	0.139		
	5217.396	3.21	−1.229	−4.4	0.150		
	5226.869	3.04	−0.809	−4.8	0.445		b
	5227.191	1.56	−1.419	−	−		b
	5229.852	3.28	−1.339	−3.9	0.187	30	
	5302.299	3.28	−0.809	−4.3	0.186		
	5307.360	1.61	−3.449	−4.3	0.113		
	5324.178	3.21	−0.20	−5.2	0.345	30	
	5328.037	0.91	−1.469	−5.2	0.633		b
	5328.534	1.56	−2.099	−	−		b
	5397.127	0.91	−1.989	−4.9	0.287	25	
	5400.502	4.37	−0.049	−4.7	0.120		
	5404.112	0.99	−1.839	−4.7	0.369	20	
	5405.774	0.99	−1.839	−4.7	0.369		
	5410.91	4.47	0.27	−4.1	0.223		
	5415.192	4.39	0.5	−4.0	0.276	20	
	5424.069	4.32	0.58	−4.2	0.364		
	5429.695	0.96	−1.879	−4.6	0.449	30	
	5432.946	4.45	−0.969	−4.5	0.123		
	5434.523	1.01	−2.119	−4.8	0.224	25	
	5436.297	4.39	−1.469	−4.8	0.189		b
	5437.089	2.45	−3.579	−	−		b
	5445.042	4.39	0.04	−4.4	0.186	24	
	5446.916	0.99	−1.859	−4.6	0.410		
	5455.441	4.32	−0.189	−4.6	0.352		b
	5455.613	1.01	−2.149	−	−		b
	5462.952	4.47	−0.229	−4.5	0.295		b
	5463.27	4.43	0.120	−	−		b
	5543.147	3.69	−1.499	−4.7	0.168		b
	5543.936	4.22	−1.069	−	−		b
	5553.578	4.43	−1.339	−4.5	0.076		
	5554.881	4.55	−0.409	−4.8	0.115		b
	5555.101	4.14	−1.949	−	−		b
	5557.976	4.47	−1.209	−4.6	0.076		

Table 2. (Contd.)

Element / Solar abundance, $\log\varepsilon_\odot$	λ, Å	EV, eV	$\log gf$	$\log\varepsilon$	W_λ, Å	$V_e \sin i$, km/s	Notes*
1	2	3	4	5	6	7	8
	5560.207	4.43	−1.119	−4.6	0.067	30	
	5562.684	4.43	−1.019	−4.9	0.180		b
Fe I	5563.599	4.19	−0.919	–	–		b
−4.50	5565.687	4.61	−0.439	−4.6	0.120		gr
	5567.392	2.61	−2.729	−5.3	0.053		b
	5568.056	4.15	−1.459	–	–		b
	5569.618	3.42	−0.529	−4.8	0.197	23	
	5572.841	3.4	−0.299	−1.3	0.326	25	b
	5662.506	4.18	−1.049	−4.7	0.178		b
	5662.936	3.69	−2.279	–	–		b
	5686.524	4.55	−0.619	−4.6	0.103		gr
	5705.465	4.3	−1.529	−4.5	0.160		b
	5705.98	4.61	−0.519	–	–		b
	5717.835	4.28	−1.059	−4.4	0.101	19	
	5837.70	4.29	−2.269	−4.2	0.097		b
	5838.37	3.94	−2.269	–	–		b
	5852.217	4.55	−1.259	−4.5	0.036	22	
	5956.692	0.86	−4.599	−4.6	0.09	23	gr
	5958.339	2.18	−4.219	−3.8	0.082		
	5974.603	4.19	−2.149	−4.9	0.060		b
	5975.337	4.83	−0.989	–	–		b
	5975.353	4.08	−1.669	–	–		
	5976.761	3.94	−1.349	−4.3	0.094	24	gr
	5983.658	4.55	−1.709	−3.5	0.126		
	5984.793	4.73	−0.509	−4.0	0.120		
	5987.046	4.8	−0.729	−4.2	0.08	24	gr
	5997.776	4.61	−1.769	−3.5	0.079		
	6003.009	3.88	−1.089	−4.2	0.134	19	gr
	6005.547	2.59	−3.579	−4.7	0.02	22	
	6007.938	4.65	−1.599	−3.6	0.333		b
	6008.54	3.88	−1.069	–	–		b
	6012.206	2.22	−4.089	−4.2	0.031	28	
	6020.169	4.61	−0.239	−3.8	0.181	18	gr
	6024.048	4.55	−0.089	−3.9	0.182	18	gr
	6136.621	2.45	−1.419	−4.9	0.580		b
	6136.993	2.2	−2.679	–	–		b
	6137.694	2.59	−1.509	–	–		b
	6147.829	4.08	−1.629	−4.5	0.073		
	6151.616	2.18	−3.349	−4.6	0.082	24	gr
	6157.725	4.08	−1.189	−4.4	0.098	22	gr
	6252.554	2.4	−1.699	−4.6	0.228		
	6256.359	2.45	−2.549	−4.0	0.22		gr
	6265.131	2.18	−2.249	−4.7	0.182	25	
	6270.222	2.86	−2.639	−4.2	0.095		
	6290.937	4.73	−1.189	−4.1	0.081		
	6297.792	2.22	−2.779	−4.8	0.102	20	tm; gr
	6301.510	3.65	−1.039	–	–		gr
	6302.503	3.69	−1.499	−4.3	0.140		
	6311.500	2.83	−3.159	−4.7	0.036		
	6322.691	2.59	−2.419	−4.2	0.152	24	gr
	6335.328	2.2	−2.109	−5.0	0.123	18	

Table 2. (Contd.)

Element Solar abundance, $\log\varepsilon_\odot$	λ, Å	EV, eV	$\log gf$	$\log\varepsilon$	W_λ, Å	$V_e \sin i$, km/s	Notes*
1	2	3	4	5	6	7	8
	6336.822	3.69	−1.019	−5.0	0.165	19	gr
	6430.844	2.18	−2.019	−4.7	0.166	17	gr
	6469.106	2.4	−4.379	−4.0	0.113		b
	6469.213	4.83	−0.759	−	−		b
	6475.625	2.56	−2.869	−4.4	0.097	23	
Fe I	6481.869	2.28	−2.989	−4.3	0.109		
−4.50	6609.110	2.56	−2.739	−4.6	0.124		
	6633.415	4.83	−1.419	−4.4	0.165		b
	6633.745	4.56	−0.769	−	−		b
	6634.098	4.8	−1.359	−	−		b
Mg I	5172.684	2.71	−0.399	−4.5	0.142		
−4.46	5183.604	2.72	−0.179	−4.55	1.210		
	5528.405	4.35	−0.619	−4.55	0.253		gr
	6318.717	5.11	−1.729	−4.6	0.258		b
	6319.237	5.11	−1.949	−4.6	−		b
Mn I	5420.354	2.14	−1.289	−6.8	0.142		
−6.65	6013.513	3.07	−0.469	−6.3	0.093		
	6021.819	3.07	−0.169	−7.2	0.067		gr
Na I	5682.633	2.1	−0.699	−5.0	0.197		gr
−5.71	5688.205	2.1	−0.449	−5.8	0.113		
	6154.226	2.1	−1.559	−5.9	0.04		gr
Ni I	4976.32	1.68	−2.939	−6.6	0.032		
−5.79	4980.166	3.61	−0.109	−6.8	0.104		
	4998.217	3.61	−0.469	−6.6	0.027		gr
	5102.958	1.68	−2.909	−6.4	0.064		
	5578.71	1.68	−2.879	−6.5	0.047		
	5694.977	4.09	−0.359	−6.1	0.062		
	5715.066	4.09	−0.409	−6.2	0.06		tm
	6327.592	1.68	−3.149	−5.8	0.082		
	6643.629	1.68	−2.299	−5.7	0.141		gr
Sc I −8.94	6305.657	0.02	−1.279	−8.6	0.06		gr
Sc II	6309.91	1.506	−1.569	−9.0	0.022		tm
−8.94	6320.86	1.507	−1.769	−8.6	0.025		tm
Si I	5337.988	5.62	−0.019	−5.5	0.088		
−4.49	5413.099	5.62	−0.709	−5.5	0.096		tm
	5665.555	4.92	−2.039	−4.6	0.04		
	5666.676	5.62	−1.049	−	−		
	5675.417	5.62	−1.029	−4.2	0.115		
	5675.756	5.62	−1.779	−	−		tm
	5948.541	5.08	−1.229	−4.8	0.065		
	6125.021	5.61	−0.929	−5.1	0.012		
	6131.573	5.62	−1.199	−5.1	0.036		
	6131.852	5.62	−1.139	−	−		
	6145.016	5.62	−0.819	−5.0	0.039		
	6155.135	5.62	−0.399	−4.7	0.093		

Table 2. (Contd.)

Element / Solar abundance, $\log\varepsilon_\odot$	λ, Å	EV, eV	$\log gf$	$\log\varepsilon$	W_λ, Å	$V_e \sin i$, km/s	Notes*
1	2	3	4	5	6	7	8
Ti I	4997.098		−2.139	−7.3	0.073		gr
−7.05	5965.828	1.88	−0.109	−7.5	0.071		gr
	5978.543	1.87	−0.359	−7.3	0.045		gr
	6126.217	1.07	−1.259	−7.7	0.017		gr
	6258.104	1.44	−0.359	−7.9	0.128		gr
Ti I	6258.709	1.46	−0.299	−	−		
Ti II	5336.78	1.583	−1.769	−6.5	0.095		
−7.05	5418.75	1.586	−2.069	−6.6	0.109		gr
	6491.6	2.067	−1.899	−7.1	0.036		
V I	5698.518	1.06	0.03	−8.7	0.114		gr
−8.04	5703.577	1.05	−0.249	−8.8	0.134		gr
	5727.05	1.08	−0.059	−8.3	0.057		gr
	6119.527	1.06	−0.619	−7.9	0.043		gr

* "b"—blended line; "gr" and "tm"—gravitation- and temperature-insensitive lines, respectively.

temperature is underestimated, using these lines will also lead to abundance underestimation. Similarly, the use of overestimated temperatures will result in overestimation of the abundances derived from lines with low χ_i values. Thus, if for some fixed temperature we observe a tendency in the $\log\varepsilon_i - \chi_i$ relation in either direction, the temperature is incorrect. We adopted as a desired temperature the value for which no systematic deviation in the $\log\varepsilon_i - \chi_i$ relation is seen.

In this method, we used the equivalent widths of 36 unblended iron lines and determined the abundances for temperatures of 4750, 5250, and 5500 K. For each temperature, we determined the behavior of the relation and interpolated the value $T_3 = 5450 \pm 150$ K according to the above condition. We assumed solar hydrogen abundance in all atmospheric models used.

Our three independent temperature determinations indicate substantial discrepancies. These could have several origins; one of the most important is the following. All calculations were carried out assuming solar abundance of all elements, including hydrogen. It is known, however, that some ALIVARS have substantially reduced hydrogen abundances. For example, for V351 Ori, $X = 0.4$ [6], while such ALIVARS as IP Per and V346 Ori [4], and also RZ Psc itself, display appreciably fainter hydrogen lines than those observed in the spectra of normal stars with the same temperatures and luminosities. Thus, we expect the hydrogen abundance in RZ Psc to be low. In this case, calculation of synthetic spectra assuming solar chemical composition can result in errors in the line intensity calculations.

In connection with this, we assigned each of the three methods a weight, proportional to the degree to which its results are independent of the assumed hydrogen abundance. The least sensitive method is that based on the color indices (weight 3), although the Balmer discontinuity, and hence the UV flux, depend on X. However, at wavelengths 450–700 nm, this effect is negligible. The second and third methods were assigned weights of 1 and 2, respectively. The resulting weighted average effective temperature is $T_{\text{eff}} = 5210 \pm 75$ K. In all subsequent calculations, we adopted $T_{\text{eff}} = 5250$ K.

3.2. Determination of $\log g$

We determined $\log g$ from metal lines that are insensitive to the gravitational acceleration (pressure). Initially, we calculated a set of synthetic spectra given the known temperature for $1.5 \leq \log g \leq 5.0$. Using these spectra, we searched for lines whose equivalent widths displayed substantially different dependences on $\log g$. Then, we selected pairs of lines with opposite characteristics for various $\log g$ values and constructed calibration curves based on the ratios of these lines. These curves made it possible to determine $\log g$ using measured intensity ratios. In total, about 80 line pairs were measured. Averaging the results for these pairs yielded $\log g = 3.41 \pm 0.02$.

3.3. Microturbulence Velocity

The method we applied is based on an idea similar to those used to determine the temperature and gravitational acceleration. The microturbulence velocity ζ affects faint lines least. For this reason, given an erroneous ζ value, the abundances for a particular element derived separately from faint and strong lines will diverge [25]. We adopted as the true ζ value that for which the abundances do not depend on the equivalent width EW of selected lines. We assumed that ζ does not depend on the height of line formation. This assumption is completely justified: judging from its $\log g$, RZ Psc is a giant, for which this condition is satisfied. To determine ζ, we calculated iron abundances from 69 lines for several microturbulence velocities ζ (1, 2, and 3 km/s). For each ζ, we constructed the dependence of [Fe/H] (derived from individual lines) on the line equivalent widths (Fig. 3). We used linear approximations to construct a family of lines, from which we selected the line with zero gradient. We can see from the figure that there is no dependence of ε on W_λ EW for $\zeta = 2.0$ km/s. Thus, our best estimate of the microturbulence velocity for RZ Psc is $\zeta = 2.0 \pm 0.5$ km/s.

3.4. $V_e \sin i$ and V_r

The parameter $V_e \sin i$ was determined by comparing the synthetic (convolved with the instrumental profile and current velocity value) and observed spectra. The value for which they best coincided was adopted as the projection of the axial rotation velocity. Using data for numerous lines, we derived the value $V_e \sin i = 23 \pm 1$ km/s for the averaged velocity. We determined the radial velocity V_r and its reduction to the center of the Sun in the usual way. As a result, we obtained the value $V_r = -11.75 \pm 1.1$ km/s.

3.5. Chemical Composition of RZ Psc

The values for T_{eff}, $\log g$, and ζ are sufficient to determine the abundances of some elements with measurable lines. Although many lines remained unregistered due to the density of the spectral orders, the échelle technique enabled detection of lines over a broad spectral interval. Table 2 presents a list of unblended or only weakly blended lines. In addition to the element designation and line wavelength λ, the columns contain the excitation potential EV, line equivalent width W_λ, oscillator strength gf, $V_e \sin i$, and a remark denoting specific properties of the line: "tm" indicates lines insensitive to temperature in the interval $4500 \leq T_{\text{eff}} \leq 5500$ K, whereas "gr" indicates lines insensitive to the gravitational acceleration.

We derived the chemical composition using synthetic spectra. Direct comparison of equivalent widths proved to be less effective, since it requires unblended lines, which restricts its application. Synthetic spectra
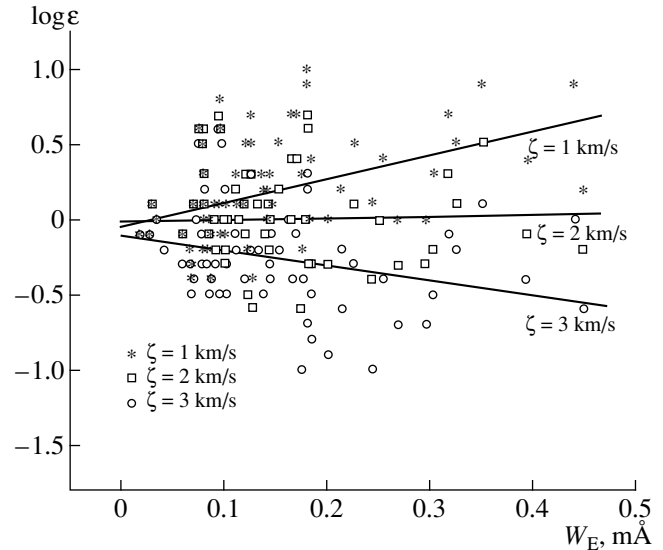

Fig. 3. Determination of microturbulence velocity ζ for RZ Psc.

were calculated using the model atmospheres of Kurucz [26, 27]. We computed a model grid for various values of T_{eff} (3500–50000 K) and $\log g$ (0–5.5) with the ATLAS12 code, taking into account blanketing due to approximately 5×10^7 lines and convective energy transfer in stars with effective temperatures below 8000 K.

We used the atomic constants published in [28]. We used the STARSP package developed by V.V. Tsymbal (private communication) to construct the synthetic spectra. When comparing the observed and calculated spectra, the latter was convolved with an instrumental profile and the observed value of $V_e \sin i$.

The spectrum calculated for a particular $\log \varepsilon$ value for a given element was compared to the observed spectrum, and, if necessary, the abundance was varied until the best fit to the observations was achieved. The method is described in more detail by Lyubimkov [25]. Table 3 presents the abundances of 14 elements in terms of [El/H] = $\log \varepsilon_{\text{RZ Psc}} - \log \varepsilon_\odot$ (i.e., relative to the solar abundance).

Unlike the other elements, the hyperfine structure of the λ 6141.71 line was taken into account when estimating the Ba abundance. Neglect of the hyperfine structure results in overestimation of the Ba abundance (by up to 0.7). Moreover, if this effect is not taken into account, the abundance determined from the Ba II λ 5853.61 line, for which no data on the hyperfine structure are available, is even more overestimated (by 1.1).

4. RESULTS AND DISCUSSION

Since ours is the first study of the chemical composition not only of RZ Psc but also of ALIVARS in general, we had hoped that the peculiar photometric behav-

Table 3

Element	Abundances [El/H]	Number lines n
Fe	+0.05	135
Ca	+0.16	14
Ni	−0.52	9
Cu	−0.8	2
Cr	−0.57	7
Mg	−0.09	5
Sc	+0.21	3
Ti	−0.43	9
Na	+0.14	3
Si	−0.45	12
Al	−0.53	2
Ba	+0.01	1
Mn	−0.12	3
V	−0.38	4

ior of the star would prove to be related to some physical peculiarities or anomalous chemical composition. However, our spectral analysis did not reveal any properties that would lead us to consider the spectral portrait of RZ Psc to be "peculiar." The star proved to be much less interesting spectrally then it was photometrically. Its physical (T_{eff}, $\log g$, ζ) and kinematic (V_r, $V_e \sin i$) parameters, as well as its localization in space and its chemical composition, suggest it is a moderately evolved population-II giant. According to the collected data, RZ Psc resembles most variable and nonvariable G8 III stars. The minor difference in its $V_e \sin i$ is too small to be related to the interesting photometric variability of the star. Nonetheless, RZ Psc does possess an interesting spectral feature: its H_α line profile. Figure 4a presents this line profile for the comparison star HD 212496 obtained on the same night, while Fig. 4b presents the profile H_α for RZ Psc. The following two facts stand out.

(1) RZ Psc's continuum spectrum has a pronounced saucerlike depression, which extends approximately ±2 nm from the line center. The depression can clearly be seen in both Crimean spectrograms of RZ Psc and is not seen in any of the spectra of HD 212496.

For the given T_{eff} and $\log g$ values, it is difficult to understand the observed depression as a result of regular photospheric mechanisms giving rise to broad line wings (the Stark effect, van der Waals forces). Moreover, the profile of the depression does not resemble the shapes of wings formed by these mechanisms. The fact
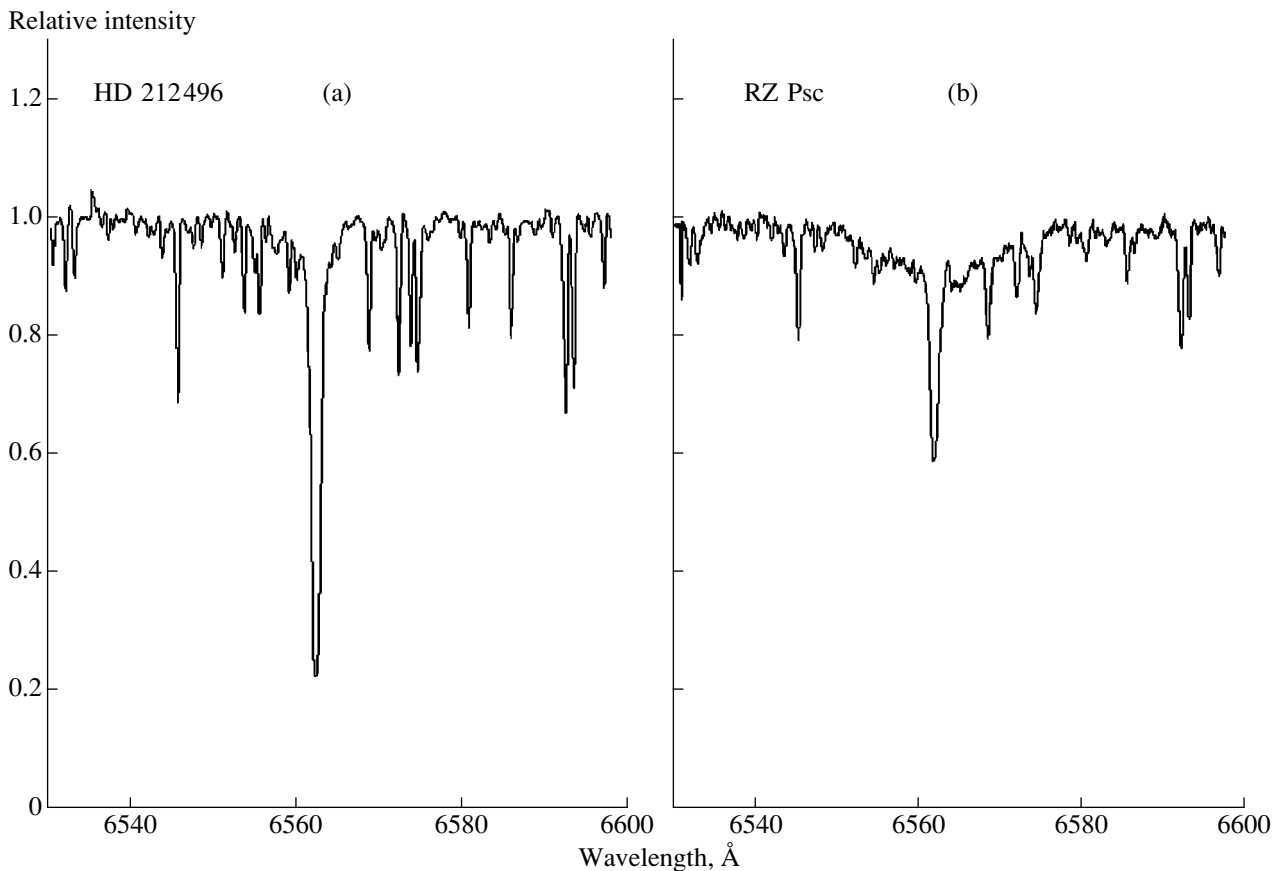

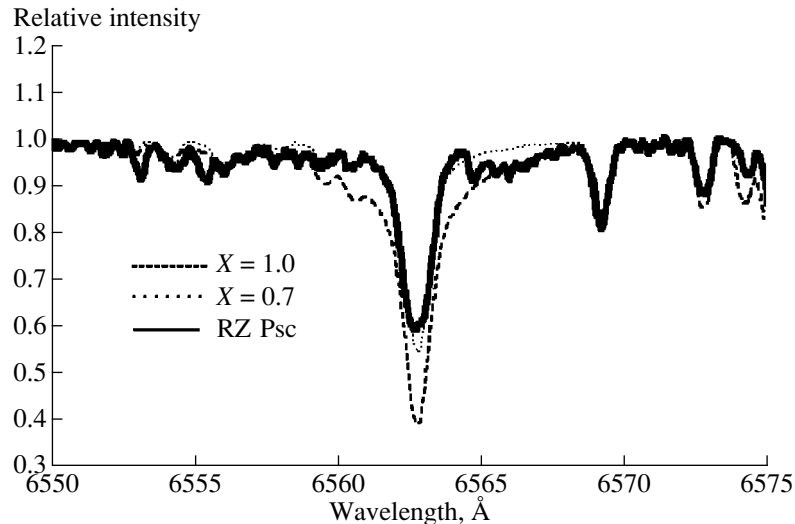**Fig. 4.** H_α profiles for (a) the standard star HD 212496 (G8.5 III) and (b) RZ Psc.

Fig. 5. Comparison between the observed H_α profile for RZ Psc (solid) and calculated profiles for relative hydrogen abundances $X = 0.7$ (dotted) and $X = 1.0$ (solar chemical composition, dashed).

that similar depressions have been detected for *A–F* supergiants at large Galactic latitudes (see the H_α profile for HD 161 796 published in [29, 30]) also rules out such explanations. The Stark effect is hardly likely to play a role in the rarified atmospheres of supergiants.

Although the origin of the depression is still unknown, the fact that similar continuum depressions have been detected for a number of well-evolved objects remote from the Galactic plane provides indirect evidence against a young age for RZ Psc.

(2) The other characteristic feature of RZ Psc is its reduced H_α line emission. Comparison with the H_α profile for HD 212496, another G8.5 III star, clearly indicates that the hydrogen abundance in the atmosphere of RZ Psc is reduced compared to normal stars. Unfortunately, we cannot calculate the hydrogen abundance accurately applying the technique to metal lines, since the depression noted above suggests some unknown special conditions for the formation of this line. Nonetheless, some estimates can be made, under certain assumptions.

Let us assume that the mechanisms or conditions for the formation of the depression and photospheric absorption line H_α are unrelated (for example, the depression is due to a remote hydrogen envelope) and can be considered independent. Two arguments can be presented in favor of this assumption. First, the depression profile has a saucer-like shape that bears no resemblance to the shape of broad wings, where the curvature indicates opposite sign. Second, if a single process resulted in the formation of both observed components, the photospheric line itself could be considered a core and the depression to represent broad wings of the same line. In that case, the line equivalent width would be 1.75 Å, which exceeds the maximum theoretical equivalent width for the H_α absorption line for normal stars of this spectral type.

The conditions for the formation of the depression and photospheric line can thus be considered to be independent, and the observed spectral pattern is essentially the result of an arithmetic addition of two profiles. In this case, the depression profile is the H_α line quasi-continuum. Then, the H_α absorption line profile normalized to the quasi-continuum will appear as shown in Fig. 5 (solid curve).

We calculated H_α line profiles for various reduced (compared to the solar value) hydrogen abundances, assuming a solar chemical composition. Ya. V. Pavlenko kindly provided us with his calculations of three model atmospheres for a star with $T_{eff} = 5250$ K, $\log g = 3.4$, and $X = 1.0, 0.7,$ and 0.5 (of the solar value) obtained using the so-called "sample opacity" technique [28, 32]. The dotted curve in Fig. 5 presents the H_α profile for a star with $T_{eff} = 5250$ K, $\log g = 3.4$, and solar hydrogen abundance. It is apparent that this curve is not in good agreement with the observed RZ Psc profile. The dashed line presents the calculated profile for $X = 0.7$ for the same T_{eff} and $\log g$. The consistency between the calculated and observed profiles provides evidence that, allowing for the above reservations, RZ Psc has a relative deficiency of hydrogen.

Comparison of the calculated (for $X = 0.7$) and observed H_α profile (Fig. 5) suggests the presence of modest emission in the line core with an equivalent width of about 0.033 Å. This is of fundamental importance. First, it enables classification of RZ Psc as a star with H_α emission, which is a property of ALIVARS. Second, this emission enables us to confirm in a lower temperature interval the relation between the H_α equivalent width and effective temperature previously discovered for ALIVARS [5]. RZ Psc possesses the lowest effective temperature of all ALIVARS studied thus far

[1] and also the faintest H_α emission component. Thus, study of the emission profile for this cool "antiflare" star has made it possible to confirm the relation between $W(H_\alpha)$ and T_{eff} established for hotter stars.

There is another peculiarity of RZ Psc worthy of comment. The axial rotation parameter $V_e \sin i$ is 23 km/s, which is slightly above normal. As is known from statistical data [33], stars with the parameters of RZ Psc have average equatorial rotation velocities $V_e \leq 15$–20 km/s. We will not dwell here on the question of why the value of $V_e \sin i$ for RZ Psc exceeds 20 km/s. Another point is more important: the large $V_e \sin i$ value clearly suggests that we observe RZ Psc edge-on, that is, the line of sight lies in the equatorial plane of the star or very close to it. This could explain the following two facts: first, RZ Psc is a very photometrically active star and, second, its brightness minima are sharp and brief, as in classical eclipse variables.

Thus, the studied parameters of RZ Psc do not provide a clear answer to the question of the origin of its photometric variability. It appears that the solution to this problem goes beyond the framework of the set of physical and kinematic parameters considered here. Possible reasons for this include binarity of the star, strong macroturbulence, and latent subphotospheric pulsations.

5. CONCLUSIONS

(1) We have determined physical (T_{eff}, $\log g$, ζ) and kinematic (V_r, $V_e \sin i$) parameters of RZ Psc, together with its chemical composition. These parameters and the localization of the star in space suggest that RZ Psc is most likely an evolved population-II star. None of the derived parameters provide a direct connection to the specific brightness variability displayed by the star.

(2) The star's chemical composition indicates a slight metal deficiency, although the iron and calcium abundances are consistent with the solar values to within the errors.

(3) We discovered a peculiar continuum depression in the region of the H_α line, which is sometimes observed in the spectra of other stars (primarily supergiants located at high Galactic latitude) but remains unexplained.

(4) We have calculated the hydrogen abundance in the atmosphere of RZ Psc assuming independent origins for the H_α depression and photospheric H_α line. The resulting value $X = 0.70$ (of the solar value) provides evidence for a relative deficiency of this element in the atmosphere of RZ Psc, which also confirms that the star is fairly evolved.

(5) Traces of emission detected in the core of the photospheric H_α line confirm that RZ Psc obeys the relation between $W(H_\alpha)$ and T_{eff} found earlier for ALIVARS as a whole.

(6) The properties of RZ Psc studied here cannot explain the origin of the star's characteristic variability.

REFERENCES

1. G. U. Kovalchuk and A. F. Pugach, Astron. Astrophys. **325**, 1077 (1997).

2. V. P. Grinin, N. N. Kiselev, N. Kh. Minikulov, *et al.*, Astron. Astrophys., Suppl. Ser. **186**, 283 (1991).

3. V. P. Grinin, N. N. Kiselev, and N. Kh. Minikulov, Pis'ma Astron. Zh. **15**, 448 (1989).

4. G. U. Koval'chuk and A. F. Pugach, Kinematika Fiz. Nebesnykh Tel **8**, 81 (1992).

5. A. F. Pugach and G. U. Kovalchuk, Astron. Astrophys. **325**, 1083 (1997).

6. G. U. Koval'chuk and A. F. Pugach, Pis'ma Astron. Zh. **24**, 133 (1998) [Astron. Lett. **24**, 106 (1998)].

7. V. P. Tsesevich, Peremen. Zvezdy **10**, 406 (1956).

8. V. I. Kardopolov, V. V. Sakhanenok, and N. A. Shutemova, Peremen. Zvezdy **21**, 310 (1980).

9. G. V. Zaĭtseva, Peremen. Zvezdy **22**, 181 (1985).

10. A. F. Pugach, Kinematika Fiz. Nebesnykh Tel **4**, 36 (1988).

11. G. V. Zaĭtseva, Peremen. Zvezdy **19**, 63 (1973).

12. V. P. Grinin, N. N. Kiselev, N. Kh. Minikulov, and G. P. Chernova, Pis'ma Astron. Zh. **14**, 514 (1988) [Sov. Astron. Lett. **14**, 219 (1988)].

13. G. V. Zaĭtseva and P. F. Chugaĭnov, Astrofizika **20**, 447 (1984).

14. V. P. Grinin, Pis'ma Astron. Zh. **14**, 65 (1988) [Sov. Astron. Lett. **14**, 27 (1988)].

15. V. P. Grinin, N. N. Kiselev, and N. Kh. Minikulov, Pis'ma Astron. Zh. **15**, 1028 (1989) [Sov. Astron. Lett. **15**, 448 (1989)].

16. V. S. Shevchenko, É. A. Vitrichenko, K. A. Grankin, *et al.*, Pis'ma Astron. Zh. **19**, 334 (1993) [Astron. Lett. **19**, 125 (1993)].

17. A. F. Pugach, Inf. Bull. Var. Stars, No. 1277, 1 (1977).

18. R. I. Goncharova, G. U. Koval'chuk, and A. F. Pugach, Astrofizika **19**, 279 (1983).

19. V. E. Panchuk, V. G. Klochkova, G. A. Galazutdinov, *et al.,* Pis'ma Astron. Zh. **19**, 1061 (1993) [Astron. Lett. **19**, 431 (1993)].

20. S. D'Odorico, C. Dous, D. Ponz, and J. L. Tanne, ESO Sci. Rep., No. 2, 1 (1984).

21. A. F. Pugach, Peremen. Zvezdy **23**, 391 (1996).

22. R. I. Goncharova, G. U. Koval'chuk, G. A. Lazorenko, *et al.*, *Catalog of WBVR Magnitudes for 300 Stars*, available from VINITI, No. 5183-B90 (Kiev, 1990).

23. G. Cayrell de Strobel, C. Soubiran, E. D. Feild, *et al.*, Astron. Astrophys., Suppl. Ser. **124**, 299 (1997).

24. M. P. FitzGerald, Astron. J. **73**, 983 (1968).

25. L. S. Lyubimkov, *Chemical Composition of Stars* (Astroprint, Moscow, 1995).

26. R. L. Kurucz, Astrophys. J., Suppl. Ser. **40**, 1 (1979).

27. R. L. Kurucz, *Peculiar Versus Normal Phenomena in A-Type and Related Stars*, Ed. by M. M. Dworetsky, F. Castelli, and R. Faraddianna, Astron. Soc. Pac. Conf. Ser. **44**, 87 (1993).

28. R. L. Kurucz, Type List (1988).

29. S. Giridhar, A. A. Ferro, and L. E. Parrao, in *IAU Symp. 132: The Impact of Very High S/N Spectroscopy on Stellar Physics* (1988), p. 407.

30. R. E. Luck, H. E. Bond, and D. L. Lambert, Astrophys. J. **357**, 188 (1990).

31. R. L. Kurucz, Preprint No. 3459, Ser. Harvard-Smithsonian Center Astrophys. (1992), p. 1.

32. Ya. V. Pavlenko and L. A. Yakovina, Astron. Zh. **71**, 863 (1994) [Astron. Rep. **38**, 768 (1994)].

33. A. A. Boyarchuk and I. M. Kopylov, Izv. Krym. Astrofiz. Obs. **31**, 44 (1964).

Translated by K. Maslennikov

Evolution of the Distribution Function and Radiation Spectrum for Electrons in a Magnetic Field

G. S. Bisnovatyĭ-Kogan and O. V. Shorokhov

Space Research Institute, Russian Academy of Sciences, Profsoyuznaya ul. 84/32, Moscow, 117810 Russia
Received September 15, 1999

Abstract—The evolution of a system of electrons with a given initial distribution in an external magnetic field is considered. An equation describing the evolution of the electron distribution function in a uniform magnetic field is derived for the case of arbitrarily relativistic electrons, and an exact solution to this equation is found. Asymptotics of this solution corresponding to the cases of synchrotron radiation and relativistic dipole radiation are calculated, and the evolution of the radiation spectra for these limiting cases is analyzed. The curvature of the magnetic field lines is taken into account phenomenologically, which demonstrates the presence of an exponential dependence in the case of synchrotron radiation. © 2000 MAIK "Nauka/Interperiodica".

1. INTRODUCTION

The problem of gyrosynchrotron radiation by a system of electrons in an external magnetic field as applied to astrophysical objects has been considered from many points of view, in particular, to explain X-ray emission by accreted matter [1–3] and the emission of radio galaxies [4, 5]. The nonthermal, power-law radio spectra and the radio jets of active galactic nuclei argue in favor of synchrotron radiation as the dominant radiation mechanism at radio wavelengths [6]. Another important evidence in favor of this mechanism is the presence of high polarization, as for the optical emission of the Crab Nebula [7, 8]. The synchrotron mechanism is also responsible for the radio emission of supernova remnants, where relativistic electrons are accelerated at the fronts of shock waves, as well as for the emission of "plerions" over a wide spectral range, where the acceleration of electrons is associated with the action of a central young radio pulsar [9, 10].

The aim of the present paper is to study the evolution of a system of electrons with a given initial angular and energy distribution in a uniform background magnetic field [5, 11]. The electrons will move along the field lines in spiral trajectories and lose their energy to magnetic bremsstrahlung radiation. The angle between the electron velocity vectors and the magnetic-field direction (the so-called pitch angle) will also decrease. As a result, the electron angular and energy distributions will change with time and become strongly anisotropic in the uniform magnetic field.

We shall consider magnetic bremsstrahlung by relativistic particles, such that the characteristic cone $\Delta\psi \approx \dfrac{mc^2}{E}$ in which most of the radiation is concentrated is fairly small [12]. Below, we shall consider separately

relativistic dipole radiation, when the pitch angle $\theta \ll \Delta\psi$, and synchrotron radiation, when $\theta \gg \Delta\psi$. In the synchrotron case, an electron emits a broad spectrum along the direction of its motion, and, to first approximation, we can neglect variations in the pitch angle and consider only the energy loss of the particle when calculating the radiation intensity. In the relativistic dipole case, the spectrum in the limit consists of a single spectral line, whose energy depends only on the electron energy and the magnetic-field strength. On the other hand, the intensity of this spectral line depends substantially on the transverse component of the electron momentum, i.e., on the angle θ. Therefore, to calculate the intensity of relativistic dipole radiation, we must take into account time variations in the pitch angle θ, despite the fact that the frequency of this radiation does not depend on θ.

2. MOTION OF AN ELECTRON IN A BACKGROUND MAGNETIC FIELD

Let us consider the motion of an electron in a constant and uniform magnetic field **H**. We introduce a Cartesian coordinate system (x, y, z), with the field along the z axis. Neglecting the reaction force of the radiation, the equation of motion takes the form

$$\frac{d}{dt}\left(\frac{m\mathbf{v}}{\sqrt{1-\dfrac{v^2}{c^2}}}\right) = \frac{e}{c}[\mathbf{v}\mathbf{H}] = \mathbf{f}$$

or, in terms of individual components,

$$\dot{v}_x = \omega v_y, \quad \dot{v}_y = -\omega v_x, \quad \dot{v}_z = 0,$$

where $\omega = \dfrac{ecH}{E}$ and $E = \dfrac{mc^2}{\sqrt{1 - \dfrac{v^2}{c^2}}}$ is the particle energy.

As the electron moves in the field $\mathbf{H}$, it experiences the deceleration force [13]

$$\mathbf{g} = \frac{2e^4}{3m^2c^4}\frac{1}{c}[\mathbf{H}[\mathbf{H}, \mathbf{v}]]$$

$$- \frac{2e^4}{3m^2c^5\left(1 - \dfrac{v^2}{c^2}\right)}\mathbf{v}\left(\frac{1}{c}[\mathbf{v}, \mathbf{H}]\right)^2. \tag{1}$$

Thus, we obtain the following equation of motion for the relativistic particle (in units where $c = 1$):

$$\dot{\mathbf{p}} = \frac{d}{dt}\left(\frac{m\mathbf{v}}{\sqrt{1 - v^2}}\right)$$

$$= \frac{m\dot{\mathbf{v}}}{\sqrt{1 - v^2}} + \frac{m\mathbf{v}}{(1 - v^2)^{\frac{3}{2}}}(\mathbf{v}, \dot{\mathbf{v}}) = \mathbf{f} + \mathbf{g}. \tag{2}$$

Writing the individual components of this expression, we obtain a system of equations for $\dot{v}_x$, $\dot{v}_y$, and $\dot{v}_z$:

$$\frac{m\dot{v}_i}{\sqrt{1 - v^2}} + \frac{mv_i}{(1 - v^2)^{\frac{3}{2}}}\sum_{j = x, y, z} v_j\dot{v}_j = f_i + g_i, \tag{3}$$

$$i = x, y, z.$$

The force is given by

$$\mathbf{g} = -\frac{2e^4H^2}{3m^2}\left\|\begin{matrix} v_x + \dfrac{v_x}{1 - v^2}(v_x^2 + v_y^2) \\[2mm] v_y + \dfrac{v_y}{1 - v^2}(v_x^2 + v_y^2) \\[2mm] \dfrac{v_z}{1 - v^2}(v_x^2 + v_y^2) \end{matrix}\right\|. \tag{4}$$

After some transformations, the system (3) can be reduced to

$$\dot{v}_x = \omega v_y - \frac{2e^4H^2}{3m^3}v_x\sqrt{1 - v^2},$$

$$\dot{v}_y = -\omega v_x - \frac{2e^4H^2}{3m^3}v_y\sqrt{1 - v^2}, \tag{5}$$

$$\dot{v}_x = 0.$$

Therefore, the velocity component along the magnetic field $v_\|$ remains constant, whereas the component perpendicular to the field decreases [14]:

$$v_\| = v_z = \text{const},$$

$$\dot{v}_\perp = -Av_\perp\sqrt{1 - v^2}, \quad A = \frac{2e^4H^2}{3m^3}, \quad v_\perp^2 = v_x^2 + v_y^2, \tag{6}$$

$$v^2 = v_\|^2 + v_\perp^2.$$

Let us write equations for the electron energy E and the angle between the direction of motion of the electron and the field $\theta = \angle(\mathbf{v}, \mathbf{H})$:

$$\frac{dE}{dt} = \frac{d}{dt}\left(\frac{m}{\sqrt{1 - v^2}}\right) = \frac{1}{2}\frac{m}{(1 - v^2)^{\frac{3}{2}}}\frac{d}{dt}(v^2). \tag{7}$$

Using (6), we find $\dfrac{d(v^2)}{dt} = \dfrac{d(v_\perp^2)}{dt} = 2v_\perp\dfrac{dv_\perp}{dt}$. Substituting this expression into (7), using (6), and introducing the notation

$$\gamma_\| = \frac{1}{\sqrt{1 - v_\|^2}}, \tag{8}$$

we find

$$\frac{dE}{dt} = -\frac{A}{m\gamma_\|^2}[E^2 - (m\gamma_\|)^2]. \tag{9}$$

Integration results in the expression

$$\text{arccoth}\left(\frac{E}{m\gamma_\|}\right) = \frac{At}{\gamma_\|} + \text{arccoth}\left(\frac{E_0}{m\gamma_\|}\right). \tag{10}$$

This result was presented in [13] for the planar case, which corresponds to $\gamma_\| = 1$. As expected, $E \longrightarrow m\gamma_\| = \dfrac{m}{\sqrt{1 - v_\|^2}}$ at $t \longrightarrow \infty$. We can determine the angle θ using the equation

$$\frac{d}{dt}(\tan\theta) = \frac{d}{dt}\left(\frac{v_\perp}{v_\|}\right) = -A\frac{v_\perp}{v_\|}\sqrt{1 - v^2}$$

or

$$\frac{d}{dt}(\tan\theta) = -A\frac{m}{E}\tan\theta. \tag{11}$$

Integration of (11) yields

$$\tan\theta = \tan\theta_0\frac{E_0}{E}\sqrt{\frac{E^2 - m^2\gamma_\|^2}{E_0^2 - m^2\gamma_\|^2}}$$

$$= \tan\theta_0\left[\cosh\left(\frac{At}{\gamma_\|}\right) + \frac{m\gamma_\|}{E_0}\sinh\left(\frac{At}{\gamma_\|}\right)\right]^{-1}. \tag{12}$$

3. EVOLUTION OF A SYSTEM OF ELECTRONS IN A UNIFORM MAGNETIC FIELD

Let us consider a spatially uniform system of electrons in a background magnetic field. Let n be the

number of particles per unit volume, which can be written

$$n = \int N_p(\mathbf{p}, t)d^3 p, \tag{13}$$

where $N(\mathbf{p}, t)$ is the phase-space "density." Introducing the spherical coordinates (p, θ, φ) in phase space and imposing the condition of axial symmetry, we obtain

$$n = 2\pi \int N_p(p, t)p^2 \sin\theta \, dp \, d\theta. \tag{14}$$

Expression (14) can be rewritten

$$n = 2\pi \int N_E(E, t)\sin\theta \, dE \, d\theta, \tag{15}$$

where

$$N_E = pEN_p. \tag{16}$$

The quantity N_p obeys the equation of continuity in momentum space:

$$\frac{\partial N_p}{\partial t} + \nabla_p \left(N_p \frac{d\mathbf{p}}{dt} \right) = 0, \tag{17}$$

which takes the following form in Cartesian coordinates:

$$\frac{\partial N_p}{\partial t} + \frac{\partial}{\partial p_x}\left(N_p \frac{dp_x}{dt} \right) + \frac{\partial}{\partial p_y}\left(N_p \frac{dp_y}{dt} \right)$$
$$+ \frac{\partial}{\partial p_z}\left(N_p \frac{dp_z}{dt} \right) = 0. \tag{18}$$

Since the quantity $v_\parallel$ is conserved during the motion of a radiating electron in the uniform magnetic field, in the presence of axial symmetry, the kinetic equation (18) can be reduced to a form that depends only on two variables. In spherical coordinates, the derivatives with respect to p and θ will depend on each other, making such a representation convenient. Note that the angle θ is approximately conserved in the ultrarelativistic case of synchrotron radiation. Therefore, the formulas obtained for the approximation $\theta = \text{const}$ in [5] coincide with asymptotics of the exact formulas derived below. On the other hand, our solution is also valid for relativistic dipole radiation, when θ rapidly decreases, as well as in intermediate cases.

Due to conservation of $v_\parallel$, any function of this quantity can be adopted as a new independent variable. Let us make a transformation from the variables (p_x, p_y, p_z) to (p, u, φ):

$$p = \sqrt{p_x^2 + p_y^2 + p_z^2}, \quad u = v_\parallel \gamma_\parallel = \frac{p_z}{\sqrt{p_x^2 + p_y^2 + m^2}},$$
$$\cos\varphi = \frac{p_x}{\sqrt{p_x^2 + p_y^2}}, \quad \sin\varphi = \frac{p_y}{\sqrt{p_x^2 + p_y^2}}. \tag{19}$$

The electron motion in (p, u, φ) coordinates is described by the equations

$$\dot{u} = 0, \quad \dot{\varphi} = -\omega,$$
$$\frac{dp}{dt} = -\frac{A}{m}\frac{\sqrt{p^2 + m^2}(p^2 - m^2 u^2)}{p(1 + u^2)}. \tag{20}$$

Taking into account (19) and (20) and the axial symmetry of the problem

$$\frac{\partial N_p}{\partial \varphi} = 0, \tag{21}$$

we can easily show that (18) will take the form

$$\frac{\partial N_p}{\partial t} + \frac{1}{p\sqrt{p^2 + m^2}}\frac{\partial}{\partial p}\left(N_p p\sqrt{p^2 + m^2}\frac{dp}{dt} \right) = 0. \tag{22}$$

Equation (22) can be rewritten

$$\frac{\partial N_E}{\partial t} + \frac{\sqrt{E^2 - m^2}}{E}\frac{\partial}{\partial E}\left(N_E \frac{E}{\sqrt{E^2 - m^2}}\frac{dE}{dt} \right) = 0. \tag{23}$$

Note that the widely used equation (see, for example [5, 11])

$$\frac{\partial N_E}{\partial t} + \frac{\partial}{\partial E}\left(N_E \frac{dE}{\partial t} \right) = 0,$$

in fact, represents the ultrarelativistic limit of Eq. (23).

Solving (22) taking into account (20), we find

$$N_p = N_p^0(p_0, u)\exp\left(-\int_0^t \Psi[p(p_0, u, \tau), u]d\tau \right), \tag{24}$$

where $N_p^0(p_0, u)$ is the initial particle distribution, $p_0(p, u, t)$ is the particle momentum at time $t = 0$, and

$$\Psi(p, u) = -\frac{2A[2p^2 + m^2(1 - u^2)]}{m(1 + u^2)\sqrt{p^2 + m^2}},$$

$$\int_0^t \Psi(p(p_0, u, \tau), u)d\tau = \int_{p_0}^p \Psi(\rho, u)\frac{1}{\frac{dp}{dt}(\rho, u)}d\rho$$
$$= \int_{p_0}^p \frac{2\rho[2\rho^2 + m^2(1 - u^2)]}{(\rho^2 + m^2)(\rho^2 - m^2 u^2)}d\rho$$
$$= \ln\frac{(p^2 + m^2)(p^2 - m^2 u^2)}{(p_0^2 + m^2)(p_0^2 - m^2 u^2)}. \tag{25}$$

Therefore, we obtain

$$N_p(p, u, t) = N_p^0(p_0, u)\frac{(p_0^2 + m^2)(p_0^2 - m^2 u^2)}{(p^2 + m^2)(p^2 - m^2 u^2)}, \tag{26}$$

where, using (10),

$$\operatorname{arccoth}\left(\frac{\sqrt{p_0^2 + m^2}}{m\sqrt{1 + u^2}}\right) = \operatorname{arccoth}\left(\frac{\sqrt{p^2 + m^2}}{m\sqrt{1 + u^2}}\right) - \frac{At}{\sqrt{1 + u^2}}. \tag{27}$$

The distribution (26) can also be obtained in another way, using an integral form of the law of conservation of particle number [11]:

$$n = 2\pi \int N_p p^2 \sin\theta\, dp\, d\theta = 2\pi \int N_p \frac{\sqrt{p^2 + m^2}}{(1 + u^2)^{\frac{3}{2}}} p\, dp\, du.$$

As a result,

$$N_p = N_p^0 \frac{\sqrt{p_0^2 + m^2}}{\sqrt{p^2 + m^2}} \frac{p_0}{p}\left(\frac{\partial p_0}{\partial p}\right)_{u,t}.$$

Substituting

$$\left(\frac{\partial p_0}{\partial p}\right)_{u,t} = \frac{p}{p_0}\frac{\sqrt{p_0^2 + m^2}}{\sqrt{p^2 + m^2}}\frac{p_0^2 - m^2 u^2}{p^2 - m^2 u^2}$$

into the previous formula also results in expression (26).

Transforming from the coordinates (p, u, φ) to the spherical coordinates (p, θ, φ), we obtain

$$N_p(p, \theta, t) = N_p^0(p_0, \theta_0)\left(\frac{p_0^2 + m^2}{p^2 + m^2}\right)^2$$
$$\times \left(\frac{p_0 \sin\theta_0}{p \sin\theta}\right)^2 \frac{p^2 \sin^2\theta + m^2}{p_0^2 \sin^2\theta_0 + m^2}. \tag{28}$$

If N_E is used instead of N_p, in accordance with formula (16), then

$$N_E(E, \theta, t) = N_E^0(E_0, \theta_0)\left(\frac{E_0}{E}\right)^3$$
$$\times \sqrt{\frac{E_0^2 - m^2}{E^2 - m^2}}\left(\frac{\sin\theta_0}{\sin\theta}\right)^2 \frac{(E^2 - m^2)\sin^2\theta + m^2}{(E_0^2 - m^2)\sin^2\theta_0 + m^2}, \tag{29}$$

where $N_E^0(E_0, \theta_0)$ is the initial energy and angular distribution of the electrons, and the initial energy $E_0(E, \theta, t)$ and angle $\theta_0(E, \theta, t)$ are determined by Eqs. (10) and (12) with

$$\gamma_\parallel(E, \theta) = \left[\sin^2\theta + \left(\frac{m}{E}\right)^2 \cos^2\theta\right]^{-\frac{1}{2}}. \tag{30}$$

Equation (10) can be used to derive the limiting energy for electrons moving at angle θ at time t. In order for the quantity E_0 in (10) to be positive, the following inequality must be satisfied:

$$\operatorname{arccoth}\left(\frac{E}{m\gamma_\parallel}\right) - \frac{At}{\gamma_\parallel} \geq 0. \tag{31}$$

In other words, $E < E_{cr}(\theta, t)$, where E_{cr} is the solution of the equation

$$\frac{E_{cr}}{m\gamma_\parallel} = \coth\left(\frac{At}{\gamma_\parallel}\right). \tag{32}$$

When $\dfrac{At}{\gamma_\parallel} \ll 1$, Eq. (32) leads to

$$E_{cr} \approx \frac{m\gamma_\parallel^2}{At} \gg m\gamma_\parallel. \tag{33}$$

On the other hand, we obtain when $\dfrac{At}{\gamma_\parallel} \gg 1$

$$E_{cr} \approx m\gamma_\parallel\left(1 + 2e^{-\frac{2At}{\gamma_\parallel}}\right). \tag{34}$$

If $E \gg m\gamma_\parallel$ (as follows from (33) and (34), this condition is satisfied when $\dfrac{At}{\gamma_\parallel} \ll 1$), formula (10) results in

$$E \approx \frac{E_0}{1 + \dfrac{E_0}{E_{cr}}}. \tag{35}$$

4. LIMITING CASES

Let us consider the case $E \gg m$ (so that, consequently, $E_0 \gg m$). Then, formula (29) yields

$$N_E \approx N_E^0(E_0, \theta_0)\left(\frac{E_0}{E}\right)^4\left(\frac{\sin\theta_0}{\sin\theta}\right)^2 \frac{E^2 \sin^2\theta + m^2}{E_0^2 \sin^2\theta_0 + m^2}. \tag{36}$$

If $\theta \ll \dfrac{m}{E}$ (the case of relativistic dipole radiation), then

$$N_E(E, \theta, t) \approx N_E^0(E_0, \theta_0)\left(\frac{E_0}{E}\right)^4 \frac{m^2}{\theta^2}\frac{\sin^2\theta_0}{E_0^2 \sin^2\theta_0 + m^2}. \tag{37}$$

On the other hand, if $\theta \gg \dfrac{m}{E}$ (the case of synchrotron radiation), then

$$N_E(E, \theta, t) \approx N_E^0(E_0, \theta_0)\left(\frac{E_0}{E}\right)^2. \tag{38}$$

The condition $\theta \gg \dfrac{m}{E}$ leads to $\theta_0 \gg \dfrac{m}{E_0}$, since both E and θ decrease with time.

Let us carry out calculations for the case of an isotropic initial angular distribution with a power-law dependence on the energy:

$$N_E^0(E_0) = KE_0^{-\alpha}, \quad m < E_0 < \infty. \tag{39}$$

We will assume that the exponent α characterizing the particle distribution is such that

$$\alpha > 1.$$

This is necessary for convergence of the integral over

$4\pi \int_{m}^{\infty} K E_0^{-\alpha} dE_0$ representing the total number of parti-

cles. When $E \gg m$ and $\theta \gg \dfrac{m}{E}$, Eq. (30) can be approximately reduced to

$$\gamma_\parallel(E, \theta) \approx \frac{1}{\sin\theta}\left[1 - \frac{1}{2}\left(\frac{m}{E\tan\theta}\right)^2\right]; \qquad (40)$$

i.e., in this limiting case, $\theta \approx$ const during the radiation process. From (33) and (35), taking into account (40), we find that, when $At\sin\theta \ll 1$,

$$E_0 \approx \frac{E}{1 - \dfrac{E}{E_{cr}}}, \qquad (41)$$

where $E_{cr} \approx \dfrac{m}{At\sin^2\theta}$. Substituting (39) and (41) into (38) yields

$$N(E, \theta, t) = \begin{cases} KE^{-\alpha}\left(1 - \dfrac{E}{E_{cr}}\right)^{\alpha-2} & \text{at} \ \ E < E_{cr}(\theta, t) \\[2mm] 0 & \text{at} \ \ E > E_{cr}(\theta, t). \end{cases} \qquad (42)$$

Formula (42) coincides with the distribution obtained in [5]; however, here, it represents only a limit of the exact formula (29), corresponding to the case of synchrotron radiation $\left(E \gg m, \theta \gg \dfrac{m}{E}\right)$. When $\theta \ll 1$ and $E \gg m$, formula (30) reduces to

$$\gamma_\parallel \approx \frac{E}{m}\left[1 - \frac{1}{2}\left(\theta\frac{E}{m}\right)^2\right] \quad \text{at} \quad \theta \ll \frac{m}{E}, \qquad (43)$$

$$\gamma_\parallel \approx \frac{1}{\theta}\left[1 + \frac{1}{6}\theta^2 - \frac{1}{2}\left(\frac{m}{E}\frac{1}{\theta}\right)^2\right] \quad \text{at} \quad \theta \gg \frac{m}{E}. \qquad (44)$$

Let us introduce the quantity

$$\eta = \frac{E}{m\gamma_\parallel} - 1. \qquad (45)$$

We then find from (43), (44), and (45) that

$$\eta \approx \frac{1}{2}\left(\theta\frac{E}{m}\right)^2 \ll 1 \quad \text{at} \quad \theta \ll \frac{m}{E}, \qquad (46)$$

$$\eta \approx \frac{E}{m}\theta \gg 1 \quad \text{at} \quad \theta \gg \frac{m}{E}. \qquad (47)$$

Let us rewrite the solution of the equations of particle motion (10) and (12) using the quantities η and η_0. It follows from (10) that

$$\operatorname{arccoth}(1 + \eta) = \frac{At}{\gamma_\parallel} + \operatorname{arccoth}(1 + \eta_0), \qquad (48)$$

and Eq. (12) leads to

$$\tan\theta = \tan\theta_0\frac{E_0}{E}\sqrt{\frac{\eta}{\eta_0}} = \tan\theta_0\frac{1 + \eta_0}{1 + \eta}\sqrt{\frac{\eta(\eta + 2)}{\eta_0(\eta_0 + 2)}}. \qquad (49)$$

Electrons satisfying the condition $\theta < \dfrac{m}{E}$ at time t could satisfy both $\theta_0 < \dfrac{m}{E_0}$ and $\theta_0 > \dfrac{m}{E_0}$ at $t = 0$. Let us consider the corresponding limiting cases.

(a) *The case of* $\theta \ll \dfrac{m}{E}$ *and* $\theta_0 \ll \dfrac{m}{E_0}$. It follows from (46) that $\eta, \eta_0 \ll 1$. Using the expansion $\operatorname{arccoth}(1 + x) \approx -\dfrac{1}{2}\ln\dfrac{x}{2} = \ln\sqrt{\dfrac{2}{x}}$ for $x \ll 1$, we can rewrite Eq. (48) in the form $\ln\sqrt{\dfrac{2}{\eta}} \approx \dfrac{At}{\gamma_\parallel} + \ln\sqrt{\dfrac{2}{\eta_0}}$, which results in

$$\eta \approx \eta_0 e^{-2\frac{At}{\gamma_\parallel}}. \qquad (50)$$

We obtain from formulas (45) and (49) with $\gamma_\parallel = $ const

$$\begin{cases} E \approx E_0\dfrac{1 + \eta}{1 + \eta_0} \approx E_0 \\[3mm] \theta \approx \theta_0\sqrt{\dfrac{\eta}{\eta_0}}. \end{cases} \qquad (51)$$

Using (50), these expressions yield

$$\begin{cases} E \approx E_0 \approx m\gamma_\parallel \\[3mm] \theta \approx \theta_0 e^{-\frac{At}{\gamma_\parallel}}. \end{cases} \qquad (52)$$

The pitch angles of electrons with initial pitch angles $\theta_0 \ll \dfrac{m}{E_0}$ decrease with time. It follows from (52) that these θ satisfy the inequality

$$\theta \ll \frac{m}{E}e^{-\frac{At}{\gamma_\parallel}}. \qquad (53)$$

Since $\theta_0 \ll \dfrac{m}{E_0}$, we can rewrite (37) using (52)

$$N_E \approx N_E^0\left(\frac{E_0}{E}\right)^4\left(\frac{\theta_0}{\theta}\right)^2. \qquad (54)$$

(b) *The case of* $\theta \ll \dfrac{m}{E}$ *and* $\theta_0 \gg \dfrac{m}{E_0}$. As follows from (46) and (47), $\eta \ll 1$ and $\eta_0 \gg 1$. We will assume

the angle θ_0 to be sufficiently small that $\tan\theta_0 \approx \theta_0$.

Using the expansion $\text{arccoth}(1 + x) \approx \text{arccoth}(x) \approx \dfrac{1}{x}$ for $x \gg 1$ and the expansion for $x \ll 1$ presented above, Eq. (48) can be rewritten $\ln\sqrt{\dfrac{2}{\eta}} \approx \dfrac{At}{\gamma_{\parallel}} + \dfrac{1}{\eta_0}$; i.e.,

$$\eta_0 \approx \frac{1}{\ln\sqrt{\dfrac{2}{\eta}} - \dfrac{At}{\gamma_{\parallel}}}. \tag{55}$$

Using (43) and (45) and taking into account the fact that $\eta_0 \gg 1$, we find

$$\frac{E_0}{E} \approx \frac{1}{\ln\sqrt{\dfrac{2}{\eta}} - \dfrac{At}{\gamma_{\parallel}}}. \tag{56}$$

In accordance with (55), the requirement $\theta_0 \gg \dfrac{m}{E_0}$, $\eta_0 \gg 1$ imposes a restriction on the current values of η and θ: $\eta \sim 2e^{-\frac{2At}{\gamma_{\parallel}}}$; i.e.,

$$\theta \sim 2\frac{m}{E}e^{-\frac{At}{\gamma_{\parallel}}}. \tag{57}$$

Since $\theta_0 \gg \dfrac{m}{E_0}$, Eq. (37) can be rewritten

$$N_E \approx N_E^0 \left(\frac{E_0}{E}\right)^4 \left(\frac{m}{\theta E_0}\right)^2. \tag{58}$$

Taking the initial distribution to be an isotropic function with a power-law dependence on the energy (39), using formulas (52), (54), (56), and (58), we obtain the following approximation for $N_E(E, \theta, t)$:

$$N(E, \theta, t)$$

$$\approx \begin{cases} KE^{-\alpha}e^{2At\frac{m}{E}} & \text{at } \theta \in \left[0, \dfrac{1}{2}\theta_1\right] \\[2ex] KE^{-\alpha}\left(\dfrac{m}{\theta E}\right)^2 \left[\ln\left(2\dfrac{m}{\theta E}\right) - At\dfrac{m}{E}\right]^{\alpha-2} \\[2ex] \text{at } \theta \in \left[\dfrac{1}{2}\theta_1, \theta_1\right], \end{cases} \tag{59}$$

where $\theta_1 = 2\dfrac{m}{E}e^{-At\frac{m}{E}}$.

5. SPECTRUM OF SYNCHROTRON RADIATION BY THE SYSTEM OF ELECTRONS

The intensity of synchrotron radiation by the system of electrons at frequency ω will be denoted Φ_ω. As is known (see, for example, [15]), synchrotron radiation is generated during the spiral motion of relativistic charged particles whose pitch angles θ satisfy the inequality $\theta \gg \dfrac{m}{E}$. Radiation by a single electron is described by the formula (see, for example, [13])

$$I_\omega(\theta, E) = \frac{\sqrt{3}}{2\pi}\frac{e^3 H_\perp}{m}P\left(\frac{\omega}{\omega_c}\right), \tag{60}$$

where

$$P(\xi) = \xi\int_\xi^\infty K_{5/3}(\eta)d\xi, \tag{61}$$

$$\omega_c = \frac{3eH_\perp}{2m}\left(\frac{E}{m}\right)^2, \quad H_\perp = H\sin\theta. \tag{62}$$

The function $P(\xi)$ possesses the asymptotics

$$P(\xi) = \begin{cases} 2^{\frac{2}{3}}\Gamma\left(\dfrac{2}{3}\right)\xi^{\frac{1}{3}}, & \xi \ll 1 \\[2ex] \sqrt{\dfrac{\pi}{2}}\xi\exp(-\xi), & \xi \gg 1. \end{cases} \tag{63}$$

The synchrotron radiation by the system at frequency ω at a specified time t is given by the integral

$$\Phi_\omega(t) = \int\left\{\int_0^\infty N(E, \theta, t)I_\omega(E, \theta)dE\right\}d\Omega, \tag{64}$$

where $d\Omega = 2\pi\sin\theta d\theta$ is the differential solid angle and $N(E, \theta, t)$ is determined by formula (42). In fact, only electrons with $E_{cr} \gg m\gamma_{\parallel}$ will contribute to Φ_ω. We can see from (33) and (34), taking into account (40), that the above condition is satisfied only when $At\theta \ll 1$. Thus, when $At \ll 1$, the integration over θ will be carried out over the limits $0 < \theta < \dfrac{\pi}{2}$; and when $At \gg 1$, over the limits $0 < \theta < \dfrac{1}{At}$.

For convenience, we will reduce the variables E, t, and ω to the dimensionless form

$$E' = \frac{E}{m}, \quad t' = At, \quad \omega' = \frac{\omega}{\dfrac{3}{2}\dfrac{eH}{m}}$$

(the primes are omitted below) and introduce the coefficient $L = \dfrac{\sqrt{3}}{2\pi}\dfrac{e^3 H}{m}$, such that $I_\omega(E, \theta) = L\sin\theta P\left(\dfrac{\omega}{\omega_c}\right)$.

Now, we must calculate the contribution to the spec-

trum by electrons whose pitch angles are in the interval $\theta \div \theta + d\theta$:

$$\phi_\omega(\sin\theta, t) = \int_0^{E_{cr}} N(E, \theta, t) I_\omega(E, \theta) dE. \qquad (65)$$

Instead of the distribution (42), we shall use the approximation

$$N(E, \theta, t)$$

$$\approx \begin{cases} KE^{-\alpha} & \text{at} \quad 0 < E < \beta E_{cr} \\ KE_{cr}^{-\alpha}\left(1 - \dfrac{E}{E_{cr}}\right)^{\alpha-2} & \text{at} \quad \beta E_{cr} < E < E_{cr} \\ 0 & \text{at} \quad E > E_{cr}, \end{cases} \qquad (66)$$

where $0 < \beta < 1$. Therefore,

$$\phi_\omega(\sin\theta, t) \approx \phi_\omega^{(1)}(\sin\theta, t) + \phi_\omega^{(2)}(\sin\theta, t), \qquad (67)$$

where

$$\phi_\omega^{(1)}(\sin\theta, t) = \int_0^{\beta E_{cr}} KE^{-\alpha} I_\omega(E, \theta) dE$$

$$= \frac{1}{2} KL\omega^{-\frac{\alpha-1}{2}} \sin^{\frac{\alpha+1}{2}} \theta \int_{\frac{1}{\beta^2}\omega t^2 \sin^3\theta}^{\infty} x^{\frac{\alpha-3}{2}} P(x) dx, \qquad (68)$$

$$\phi_\omega^{(2)}(\sin\theta, t) = \int_{\beta E_{cr}}^{E_{cr}} KE_{cr}^{-\alpha}\left(1 - \frac{E}{E_{cr}}\right)^{\alpha-2} I_\omega(E, \theta)$$

$$= \frac{1}{2} KL(\sin^2\theta t)^\alpha \sqrt{\omega\sin\theta} \qquad (69)$$

$$\times \int_{\omega t^2 \sin^3\theta}^{\frac{1}{\beta^2}\omega t^2 \sin^3\theta} \left(1 - \sqrt{\frac{\omega t^2 \sin^3\theta}{x}}\right)^{\alpha-2} x^{-\frac{3}{2}} P(x) dx.$$

Let us consider the region $\omega t^2 \sin^3\theta \ll 1$. Then,

$$\phi_\omega^{(1)}(\sin\theta, t) \approx \frac{1}{2} KLC_1(\alpha)\omega^{-\frac{\alpha-1}{2}} \sin^{\frac{\alpha+1}{2}} \theta, \qquad (70)$$

where $C_1(\alpha) = \int_0^\infty P(x) x^{\frac{\alpha-3}{2}} dx$, and

$$\phi_\omega^{(2)} \approx 2^{\frac{2}{3}} \Gamma\left(\frac{2}{3}\right) KLC_2(\alpha, \beta)(\sin^2\theta t)^\alpha \qquad (71)$$

$$\times \sqrt{\omega\sin\theta}(\omega t^2 \sin^3\theta)^{-\frac{1}{6}},$$

where $C_2(\alpha, \beta) = \int_0^{1-\beta} \dfrac{y^{\alpha-2}}{(1-y)^{\frac{2}{3}}} dy.$

Since $\dfrac{\phi_\omega^{(2)}(\sin\theta, t)}{\phi_\omega^{(1)}(\sin\theta, t)} \sim (\omega t^2 \sin^3\theta)^{\frac{3\alpha-1}{6}}$, $\phi_\omega^{(2)}(\sin\theta, t) \ll \phi_\omega^{(1)}(\sin\theta, t)$.

Next, let us consider the region $\omega t^2 \sin^3\theta \gg 1$. Then,

$$\phi_\omega^{(1)} \approx \frac{1}{2}\sqrt{\frac{\pi}{2}} KL\omega^{-\frac{\alpha-1}{2}} \sin^{\frac{\alpha+1}{2}} \theta\left(\frac{1}{\beta^2}\omega t^2 \sin^3\theta\right)^{\frac{\alpha}{2}-1}$$

$$\times \exp\left(-\frac{1}{\beta^2}\omega t^2 \sin^3\theta\right), \qquad (72)$$

$$\phi_\omega^{(2)} = \sqrt{\frac{\pi}{2}} KL(\sin^2\theta t)^\alpha \sqrt{\omega\sin\theta}\,\Xi,$$

where

$$\Xi = \int_0^{1-\beta} \frac{y^{\alpha-2}}{1-y} e^{-\frac{\omega t^2 \sin^3\theta}{(1-y)^2}} dy$$

$$\approx 2^{1-\alpha}\Gamma(\alpha-1)(\omega t^2 \sin^3\theta)^{1-\alpha} e^{-\omega t^2 \sin^3\theta}.$$

Therefore,

$$\phi_\omega^{(2)}(\sin\theta, t) \approx 2^{1-\alpha}\sqrt{\frac{\pi}{2}}\Gamma(\alpha-1) KL(\sin^2\theta t)^\alpha \qquad (73)$$

$$\times \sqrt{\omega\sin\theta}(\omega t^2 \sin^3\theta)^{1-\alpha} e^{-\omega t^2 \sin^3\theta}.$$

Since $\omega t^2 \sin^3\theta \gg 1$ and $\dfrac{1}{\beta^2} > 1$, $\phi_\omega^{(1)}(\theta, t) \ll \phi_\omega^{(2)}(\theta, t)$. Therefore,

$$\phi_\omega(\sin\theta, t)$$

$$\approx \begin{cases} S_\omega(\sin\theta, t) & \text{at} \quad \omega t^2 \sin^3\theta \ll 1 \\ Q_\omega(\sin\theta, t) & \text{at} \quad \omega t^2 \sin^3\theta \gg 1, \end{cases}$$

$$S_\omega(\sin\theta, t) = S\omega^{-\frac{\alpha-1}{2}} \sin^{\frac{\alpha+1}{2}} \theta, \qquad (74)$$

$$Q_\omega(\sin\theta, t) = Q(\sin^2\theta t)^\alpha \sqrt{\omega\sin\theta}$$

$$\times (\omega t^2 \sin^3\theta)^{1-\alpha} e^{-\omega t^2 \sin^3\theta},$$

where $S = \dfrac{1}{2} KLC_1(\alpha)$ and $Q = 2^{1-\alpha}\sqrt{\dfrac{\pi}{2}}\Gamma(\alpha-1)KL.$

Let us calculate the total radiation by the system:

$$\Phi_\omega(t) = 4\pi\int_0^{\frac{\pi}{2}} \phi_\omega(\sin\theta, t)\sin\theta d\theta \approx 4\pi\int_0^1 \phi_\omega(\theta, t)\theta d\theta.$$

We first consider the case $t \ll 1$. Then, when $\omega \ll t^{-2}$,

$$\Phi_\omega(t) \approx 4\pi \int\limits_0^1 S_\omega(\theta, t)\theta d\theta = \frac{8\pi S}{\alpha + 5}\omega^{-\frac{\alpha - 1}{2}}, \qquad (75)$$

whereas, when $\omega \gg t^{-2}$,

$$\Phi_\omega(t) \approx 4\pi \int\limits_0^{\left(\frac{1}{\omega t^2}\right)^{\frac{1}{3}}} S_\omega(\theta, t)\theta d\theta + 4\pi \int\limits_{\left(\frac{1}{\omega t^2}\right)^{\frac{1}{3}}}^1 Q_\omega(\theta, t)\theta d\theta \qquad (76)$$

$$\approx \left\{\frac{8\pi S}{\alpha + 5} + \frac{4\pi Q}{3}\Gamma\left(\frac{11 - 2\alpha}{6}, 1\right)\right\}\omega^{-\frac{\alpha - 1}{2}}(\omega t^2)^{-\frac{\alpha + 5}{6}}.$$

We next consider the case $t \gg 1$. When $\omega \ll t$, we find

$$\Phi_\omega(t) \approx 4\pi \int\limits_0^{\frac{1}{t}} S_\omega(\theta, t)\theta d\theta = \frac{8\pi S}{\alpha + 5}\omega^{-\frac{\alpha - 1}{2}} t^{-\frac{\alpha + 5}{2}}; \quad (77)$$

and when $\omega \gg t$,

$$\Phi_\omega(t) \approx 4\pi \int\limits_0^{\left(\frac{1}{\omega t^2}\right)^{\frac{1}{3}}} S_\omega(\theta, t)\theta d\theta + 4\pi \int\limits_{\left(\frac{1}{\omega t^2}\right)^{\frac{1}{3}}}^{\frac{1}{t}} Q_\omega(\theta, t)\theta d\theta \qquad (78)$$

$$\approx \left\{\frac{8\pi S}{\alpha + 5} + \frac{4\pi Q}{3}\Gamma\left(\frac{11 - 2\alpha}{6}, 1\right)\right\}\omega^{-\frac{\alpha - 1}{2}}(\omega t^2)^{-\frac{\alpha + 5}{6}}.$$

Except for the coefficients, the power-law dependences (75), (76), and (78) coincide with the corresponding expressions obtained in [5]. Note that only particles whose energy E satisfies the condition $\frac{m}{\theta} = E^* \ll E \ll E_{cr}$ contribute to the integral (64) characterizing the synchrotron radiation by the entire system. The quantity E^* increases as $\frac{1}{\theta}$ when $\theta \longrightarrow 0$, and E_{cr} increases as $\frac{1}{\theta^2}$. As a result, particles with arbitrarily large energy contribute to Φ_ω in the case of sufficiently small angles. This contribution by such high-energy particles means that, despite the exponential asymptotics of the radiation spectrum for a single particle at large frequencies, the total spectrum of the system of particles has a power-law character over the entire frequency range.

6. INTENSITY AND SPECTRUM OF RELATIVISTIC DIPOLE RADIATION BY THE SYSTEM OF ELECTRONS

Finally, we consider the contribution to the system's radiation by particles with $E \gg m$ and $\theta \ll \frac{m}{E}$. This is called relativistic dipole radiation, since it has a dipole character after transformation from the laboratory coordinate system S to the system S' in which $v'_\parallel = 0$ [15]. Indeed, since $\theta \sim \frac{v_\perp}{v_\parallel} = \frac{v'_\perp\sqrt{1 - v_\parallel^2}}{v_\parallel}$ and $\frac{m}{E} = \sqrt{1 - v^2}$, $v'_\perp \ll v_\parallel\frac{\sqrt{1 - v^2}}{\sqrt{1 - v_\parallel^2}} < v_\parallel \sim 1$; i.e.,

$$v'_\perp \ll 1. \qquad (79)$$

The motion in S' is nonrelativistic and, when $v'_\perp \ll 1$, for the most part, corresponds to the frequency [16, 17]

$$\omega_H = \frac{eH}{mc}. \qquad (80)$$

The total rate of energy loss to gyrosynchrotron radiation by a single ultrarelativistic electron is given by the formula

$$-\frac{dE}{dt} = I = G\left(\frac{E}{m}\right)^2\sin^2\theta, \quad G = \frac{2e^4H^2}{3m^2}. \qquad (81)$$

Since the characteristic size of the radiation cone in the dipole relativistic case is $\Delta\psi \sim \frac{m}{E} \gg \theta$, nearly all the radiation propagates along the magnetic field. Therefore, to first approximation, we can assume that the particle radiates along the direction of its motion (which coincides with the direction of the magnetic field) at the frequency

$$\omega = \omega_H\frac{\sqrt{1 - v_\parallel^2}}{1 - v_\parallel\cos 0} \approx 2\omega_H\gamma_\parallel \approx 2\omega_H\frac{E}{m};$$

i.e., [16, 17],

$$\frac{E}{m} \approx \frac{\omega}{2\omega_H}. \qquad (82)$$

Therefore, radiation by ultrarelativistic electrons satisfying the condition $\theta \ll \frac{m}{E}$ is described by the formula

$$\Phi = \int\Phi_\omega d\omega \approx \int dE\int N(E, \theta, t)I(E, \theta)$$

$$\times \delta\left(\omega - 2\omega_H\frac{E}{m}\right)2\pi\theta d\theta. \qquad (83)$$

We introduce the dimensionless quantities $t' = At$ and $E' = \dfrac{E}{m}$ (the primes are omitted below). Finally, the spectrum of the relativistic dipole radiation takes the form

$$\Phi_\omega = \frac{1}{2\omega_H}\int N(E, \theta, t) I(E, \theta) 2\pi\theta d\theta \bigg|_{E = \frac{\omega}{2\omega_H}}. \quad (84)$$

Using (59), we can calculate the contributions from particles with $\theta \in \left[0, \frac{1}{2}\theta_1\right]$ and $\theta \in \left[\frac{1}{2}\theta_1, \theta_1\right]$, which will be denoted $\phi_\omega^{(1)}$ and $\phi_\omega^{(2)}$, respectively:

$$\Phi_\omega^{(1)} \approx \frac{1}{2\omega_H}\int_0^{\frac{1}{2}\theta_1} KE^{-\alpha}e^{2\frac{t}{E}}GE^2\theta^2 2\pi\theta d\theta \quad (85)$$

$$= \frac{\pi KG}{4\omega_H}E^{-(\alpha+2)}e^{-2\frac{t}{E}}\bigg|_{E = \frac{\omega}{2\omega_H}},$$

$$\phi_\omega^{(2)} \approx \frac{1}{2\omega_H}\int_{\frac{1}{2}\theta_1}^{\theta_1} KE^{-\alpha}\left(\frac{1}{\theta E}\right)^2$$

$$\times \left[\ln\left(2\frac{1}{E\theta}\right) - \frac{t}{E}\right]^{\alpha-2}GE^2\theta^2 2\pi\theta d\theta \quad (86)$$

$$= \frac{2^{3-\alpha}\pi KG}{\omega_H}\gamma(\alpha-1, \ln 4)E^{-(\alpha+2)}e^{-2\frac{t}{E}}\bigg|_{E = \frac{\omega}{2\omega_H}}.$$

Therefore, the final result takes the form

$$\Phi_\omega \approx \phi_\omega^{(1)} + \phi_\omega^{(2)} \approx \frac{\pi KG}{4\omega_H}[1 + 2^{5-\alpha}\gamma(\alpha-1, \ln 4)]$$

$$\times \left(\frac{\omega}{2\omega_H}\right)^{-(\alpha+2)}e^{-4t\frac{\omega_H}{\omega}}. \quad (87)$$

7. DISCUSSION

Throughout the analysis conducted above, we assumed that the magnetic field was uniform everywhere. In real astrophysical objects, the scale of field nonuniformity R, which is equivalent to the radius of curvature of the field lines, can vary from the radius of a neutron star, $\sim 10^6$ cm, to the radius of a galaxy, $\sim 10^{23}$ cm. The formulas derived here and in most of the cited papers are valid as long as the electrons do not sense the curvature of the field lines, i.e., as long as their mean free paths satisfy the condition $l = ct \ll R$. On the other hand, real magnetic fields substantially deviate from uniformity in the course of time. From a phenomenological point of view, we can describe this effect by

introducing a minimum pitch angle for the electrons, $\theta_{min} \approx \dfrac{ct}{R} \ll 1$. Incorporating such a minimum pitch angle in the analysis changes the power-law asymptotics for the radiation spectrum for the system of relativistic electrons to an exponential spectrum at large t. If the integration in (64) is carried out from $\theta_{min} \ll 1$ rather than from 0, then $\Phi_\omega(t) \approx 0$ when $t \gg \dfrac{1}{\theta_{min}}$; when $t \ll \dfrac{1}{\theta_{min}}$, the spectra remain the same, but there is an exponential cut-off at $\omega \gg \dfrac{1}{\theta_{min}^3 t^2}$:

$$\Phi_\omega(t) \approx \frac{4\pi Q}{3}(\theta_{min}^2 t)^{\alpha+2}(\omega\theta_{min})^{\frac{3}{2}}$$

$$\times (\omega t^2\theta_{min}^3)^{-(\alpha+1)}e^{-\omega t^2\theta_{min}^3}. \quad (88)$$

Substituting $\theta_{min} = \dfrac{t}{R}$ into (88) (recall that $c = 1$), we obtain

$$\Phi_\omega(t) \approx \frac{4\pi Q}{3}\omega^{-\alpha+\frac{1}{2}}t^{-2\alpha+\frac{5}{2}}R^{\alpha-\frac{5}{2}}e^{-\frac{\omega t^5}{R^3}}. \quad (89)$$

When interpreting observations of relativistic dipole radiation, it should be borne in mind that the intensity observed along the magnetic-field direction is considerably greater than the angle-averaged intensity $J_\omega = \dfrac{\Phi_\omega}{4\pi}$, which we have calculated above using the energy-loss rate [12]. In particular, an interpretation of a hard feature in the spectra of Her X-1 and certain other X-ray pulsars in the framework of a gyrosynchrotron model for radiation by relativistic electrons was given in [17]. Note that, in contrast to the relativistic dipole case (when almost all the radiation propagates along the magnetic field), in the cyclotron limit ($\gamma_\parallel = 1$), the angular distribution changes and, at large harmonic numbers n, is concentrated near the plane of rotation of the electrons [18]. Recent observations of cyclotron lines by *BeppoSax* [19] have revealed weak variations in the radiation pattern with increasing n, up to $n = 4$. This suggests that the observed radiation is probably relativistic dipole radiation.

8. CONCLUSIONS

In the present paper, we have derived an equation for the evolution of the distribution function for electrons in a uniform magnetic field, applicable for arbitrary electron velocity. Formulas describing the evolution of the electron distribution function and the corresponding radiation spectrum were obtained for the

general case. They reduce to the well-known results of [5] in the limiting case of ultrarelativistic electrons. New asymptotics were obtained for the case of relativistic dipole radiation.

With regard to real astrophysical objects, a phenomenological allowance for the finite radius of curvature of the magnetic-field lines can be made by introducing a minimum pitch angle for the electrons. This leads to an exponential dependence for the spectrum at large energies instead of the pure power-law dependence expected for the case of a uniform magnetic field.

REFERENCES

1. G. S. Bisnovatyĭ-Kogan and A. M. Fridman, Astron. Zh. **46**, 721 (1969) [Sov. Astron. **13**, 566 (1969)].

2. Yu. N. Gnedin and R. A. Sunyaev, Astron. Astrophys. **25**, 233 (1973).

3. G. S. Bisnovatyĭ-Kogan, Astron. Zh. **50**, 902 (1973) [Sov. Astron. **17**, 574 (1973)].

4. N. S. Kardashev, A. D. Kuz'min, and S. I. Syrovatskiĭ, Astron. Zh. **39**, 216 (1962) [Sov. Astron. **6**, 167 (1962)].

5. N. S. Kardashev, Astron. Zh. **39**, 393 (1962) [Sov. Astron. **6**, 317 (1962)].

6. K. I. Kellerman, *Galactic and Extra-Galactic Radio Astronomy* (Springer, Berlin, 1974).

7. V. A. Dombrovskiĭ, Dokl. Akad. Nauk SSSR **94**, 1021 (1954).

8. M. A. Vashakidze, Astron. Tsirk., No. 147, 11 (1954).

9. N. S. Kardashev, Astron. Zh. **41**, 807 (1964) [Sov. Astron. **8**, 643 (1964)].

10. T. A. Lozinskaya, *Supernovae and Stellar Winds* [in Russian] (Nauka, Moscow, 1986).

11. A. Pacholczyk, *Radio Astrophysics. Nonthermal Processes in Galactic and Extragalactic Sources* (Freeman, San Francisco, 1970; Mir, Moscow, 1973).

12. V. L. Ginzburg and S. I. Syrovatskii, Ann. Rev. Astron. Astrophys. **7**, 375 (1969).

13. L. D. Landau and E. M. Lifshitz, *The Classical Theory of Fields* (Nauka, Moscow, 1988, 6th ed.; Pergamon Press, Oxford, 1975, 4th ed.).

14. V. L. Ginzburg, *Theoretical Physics and Astrophysics* (Nauka, Moscow, 1988; Pergamon Press, Oxford, 1979).

15. V. V. Zheleznyakov, *Radiation in Astrophysical Plasma* (Yanus-K, Moscow, 1997).

16. R. I. Epstein, Astrophys. J. **183**, 611 (1973).

17. A. V. Baushev and G. S. Bisnovatyĭ-Kogan, Astron. Zh. **76**, 283 (1999) [Astron. Rep. **43**, 241 (1999)].

18. V. A. Trubnikov, Phys. Fluids **4**, 195 (1961).

19. A. Santangelo *et al.*, Astrophys. J. Lett. **523**, L85 (1999).

Translated by Yu. Dumin

Anisotropy and Velocity of Small-Scale Irregularities in the Region of Solar-Wind Acceleration

I. V. Chasheĭ[1], A. I. Efimov[2], V. K. Rudash[2], and M. K. Bird[3]

[1]*Lebedev Physical Institute, Russian Academy of Sciences, Leninskiĭ pr. 53, Moscow, 117924 Russia*
[2]*Institute of Radio Engineering and Electronics, Russian Academy of Sciences, Mokhovaya 11, Moscow, 103907 Russia*
[3]*Institute of Radio Astronomy, Bonn University, Bonn, Germany.*
Received September 10, 1999

Abstract—We present the amplitude and frequency fluctuations of radio signals detected simultaneously at ground stations at Evpatoriya and Ussuriĭsk during experiments in which radio signals with wavelengths of 5, 8, and 32 cm emitted from the *Venera-15* and *Venera-16* spacecraft were transmitted through the solar plasma environment. Relations are obtained between the rates of amplitude scintillations (determined from the width of temporal spectra) and frequency scintillations (determined from the delay of the fluctuations between the ground stations), on the one hand, and the velocities of the solar wind and of wave-like density disturbances and the anisotropy of irregularities, on the other hand. Analysis shows that the transition of the solar-wind flow to a supersonic regime takes place at heliocentric distances of 10–15 solar radii (R_s) and that the flow becomes supersonic at distances exceeding $15R_s$. Solar-wind density inhomogeneities with scales of about 50 km are radially extended. For heliocentric distances from 10 to $20R_s$, the degree of extension is modest and, as a rule, does not exceed a factor of two. © *2000 MAIK "Nauka/Interperiodica".*

1. INTRODUCTION

The processes occurring in the acceleration region situated at heliocentric distances below $20R_s$ (R_s is the radius of the Sun) are fundamental for the physics of the solar wind. Most information on the solar wind parameters in this region, which remains inaccessible to direct measurement, is obtained by studying radio signals transmitted through it. In spite of their indirect origin, such radio data provide important qualitative conclusions and quantitative estimates. In particular, this is true of the magnetic fields, which substantially determine the structure and dynamics of the solar wind and can govern the anisotropy of the irregularities modulating the radio signals.

For example, VLA measurements of the scattering of signals from compact radio sources showed that plasma density irregularities on scales $1 \leq 35$ km are extended in the radial direction [1], apparently due to the radial orientation of the regular magnetic fields in the supercorona. At heliocentric distances $r < 6R_s$, the degree of anisotropy (axial ratio) μ is rather high ($\mu \approx 10$), though it decreases to $\mu = 2$–3 at $r > 6R_s$. Studies of fluctuations of the Faraday rotation of the plane of polarization of radio signals emitted from the *Helios-1* and *Helios-2* spacecraft showed that, at $r < 10R_s$, large-scale ($l \sim 10^5$ km) irregularities of the magnetic field are also radially extended with $\mu \approx 10$ [2], indicating strong angular anisotropy in the energy spectrum of the Alfvén waves giving rise to the Faraday-rotation fluctuations.

In addition to scattering, the plasma-density irregularities give rise to amplitude and frequency (phase) fluctuations (scintillations) in radio signals propagating through the plasma. In these scintillation effects, temporal fluctuations result from the transformation of spatial fluctuations due to motion of the irregularities relative to the line of sight. Therefore, the scintillation parameters can be sensitive to both the anisotropy and velocity of the irregularities. The effective velocity of the irregularities was determined as a function of radius from the width of the temporal energy spectra of the amplitude fluctuations for signals from the *Venera-15* and *Venera-16* spacecraft. This velocity exhibits a local minimum at heliocentric distances of about $10R_s$ [3], which has been interpreted as a region where the solar-wind velocity is close to the speed of sound—the propagation speed for the slow magnetoacoustic waves modulating the amplitudes of the radio signals in the solar-wind plasma. The location of the supersonic transition region is of considerable importance for the physics of the solar wind, since it is directly connected with the nature of sources of additional plasma acceleration.

It was established in earlier studies in which radio signals were transmitted through the equatorial regions of the outer solar corona, where streamers are usually observed, that the sonic point in these regions is 10–$14R_s$ from the photosphere [5]. Information provided since 1995 by the International Solar-Heliospheric Observatory SOHO convincingly showed that the sonic points in closed magnetic configurations are significantly further from the Sun than those in coronal holes [6].

The current work presents an analysis of the widths of temporal spectra of amplitude fluctuations for radio

signals emitted from the *Venera-15* and *Venera-16* spacecraft, based on simultaneous measurements of frequency fluctuations detected at two distantly spaced ground stations. Our objective is to determine the flow regime and anisotropy of the irregularities for heliocentric distances near $r = 10R_s$.

2. VELOCITY AND ANISOTROPY OF IRREGULARITIES IN TEMPORAL SPECTRA AND CROSS CORRELATION OF SCINTILLATIONS

Let us consider the temporal spectra of weak fluctuations of the intensity (amplitude) of radio signals propagating through a medium with wavelike, anisotropic plasma-density irregularities. We assume that the spatial energy spectrum of the density irregularities takes the power-law form

$$P_N(\mathbf{q}) = C_N[\mu^2 q_x^2 + (q_y^2 + q_z^2)]^{-\alpha/2}, \qquad (1)$$

where C_N is the structural constant; $\mathbf{q}$, the spatial frequency (wave number); μ, the anisotropy parameter ($\mu > 1$ when the irregularities are stretched along the radial direction); and α, the power-law index. We chose a reference frame such that the origin coincides with the observation point; the OZ axis is directed along the line of sight to the radio source; and the OX axis is perpendicular to the OZ axis and fixed in the plane containing the Earth, Sun, and radio source. The minimum distance R between the line of sight and the center of the Sun is called the impact parameter and is usually expressed in solar radii R_s. This distance is reached at the so-called impact point of the line of sight, located at a distance z_0 from the Earth. It is quite clear that $z_0^2 + R^2 = a^2$, where a is the distance between the Earth and the center of the Sun.

In a weak-fluctuation regime, the two-dimensional spatial energy spectrum of the amplitude scintillations $M(\mathbf{q})$ is related to the spectrum $P_N(\mathbf{q})$ given by (1) via the well-known equation [3]

$$M(q_x, q_y) = A_1 \lambda^2 \int_0^L C_N(z)(\mu^2 q_x^2 + q_y^2)^{-\alpha/2} \qquad (2)$$
$$\times \sin^2[(q_x^2 + q_y^2)(L-z)\lambda z/4\pi L]dz,$$

where $A_1 = $ const, λ is the wavelength of the radio signal, and the integration is along the line of sight from the ground observer ($z = 0$) to the spacecraft ($z = L$). To determine the temporal spectrum of the scintillations, we must know the character of the motion and time variations of the irregularities; that is, the spatial–temporal spectrum of the turbulence. Further, as in [3], we shall use the model for small-scale turbulence proposed in [4] for the region of solar-wind acceleration. In this model, density fluctuations are primarily attributed to slow magnetoacoustic waves, which are generated locally by nonlinear interactions of Alfvén waves. These magnetoacoustic waves propagate from the Sun and toward the Sun with equal probabilities through the moving solar-wind plasma. It is assumed that the magnetic field is strong, so that the Alfvén speed substantially exceeds the sound and solar-wind speeds [4]. Under these assumptions, we obtain for the temporal spectrum of the scintillations $M(\nu)$ [3, 4]

$$M(\nu) = A_1 \lambda^2 \int_0^L C_N(z)[M^+(\nu) + M^-(\nu)]dz, \qquad (3)$$

$$M^\pm(\nu) = |\nu \pm v_s|^{-1}$$
$$\times \int_{-\infty}^{+\infty} \sin^2[(q_x^2 + q_y^2)(L-z)\lambda z/4\pi L](\mu^2 q_x^2 + q_y^2)^{-\alpha/2}dq_y. \qquad (4)$$

We take the radial wave number q_x in (4) to be

$$q_x = 2\pi\nu/|\nu \pm v_s|, \qquad (5)$$

where ν is the solar-wind speed, v_s is the sound speed, and the + and − signs correspond to waves propagating from and toward the Sun, respectively. We obtained relations (3)–(5) for a spatial–temporal turbulence spectrum of the form

$$P_N(\mathbf{q}, \nu) = \frac{1}{2}P_N(\mathbf{q})[\delta(2\pi\nu - q_x|\nu + v_s|) + \delta(2\pi\nu - q_x|\nu - v_s|)]. \qquad (6)$$

In the simple model (6), the directions of the solar-wind velocity $\mathbf{v}$ and the group wave velocity $\mathbf{v}_s$ coincide with the orientation axis for elongated irregularities $0X$. This model is applicable to the problem at hand due to the fact that the regular magnetic field in the supercorona is strong and directed approximately radially.

Typical amplitude scintillation spectra have a flat section at low frequencies ν and fall off according to a power law $M_{ac} \sim \nu^{-p}$ at high ν [3]. We estimate the characteristic width ν_0 of the temporal spectrum $M(\nu)$ by matching the low-frequency and high-frequency asymptotics [3]:

$$M_{ac}(\nu_0) = M(\nu \longrightarrow 0). \qquad (7)$$

Let us make the natural assumption for inner regions of the solar wind that the scattering medium is localized in a fairly narrow layer adjacent to the impact point of the line of sight ($z = z_0$). Then, carrying out the calculations performed in [3] for isotropic irregularities, we obtain the following relation for the characteristic frequency ν_0:

$$\nu_0 = \gamma[2\pi\lambda z_0(L - z_0)/L]^{-1/2}V_{ap}. \qquad (8)$$

Here, V_{ap} is a certain (apparent) velocity of the irregularities, which, for the adopted spatial–temporal spectrum of the wave turbulence (6), is equal to

$$V_{ap}$$
$$= \frac{1}{\mu}\left[\frac{(|v + v_s|^{\alpha-2} + |v - v_s|^{\alpha-2})|v^2 - v_s^2|}{|v + v_s| + |v - v_s|}\right]^{1/(\alpha-1)}, \quad (9)$$

where γ is a numerical coefficient of the order of unity, which depends only on the power-law index α:

$$\gamma = \{2\Gamma((\alpha-1)/2)\Gamma((\alpha+1)/2)$$
$$\times \sin[\pi(\alpha-1)/4]/(\pi)^{1/2}\Gamma(\alpha/2)\}^{1/(\alpha-1)}. \quad (10)$$

Equation (8) shows that, in addition to known geometric parameters contained in the Fresnel scale, the characteristic frequency ν_0 is determined by the velocities $v \pm v_s$ and the anisotropy μ of the irregularities. Therefore, we cannot uniquely determine μ, v, and v_s using only the frequency ν_0 at the bend of the scintillation spectrum.

The possible influence of the anisotropy of the irregularities on the temporal spectra of the scintillations was noted by Erukhimov *et al.* [7], who considered a flow with a fixed velocity directed at some angle to the direction of extension of the irregularities. Relation (8) can be generalized for the case of a statistical velocity distribution. In this case, we should substitute into (8) in place of μV_{ap} (9),

$$\mu V_{ap} = (\langle v^{\alpha-2}\rangle/\langle v^{-1}\rangle)^{1/(\alpha-1)}, \quad (11)$$

with $\langle v^{\alpha-2}\rangle$ and $\langle v^{-1}\rangle$ being the corresponding moments of the velocity distribution.

Simultaneous observations of amplitude and frequency (phase) scintillations at distant receiving points can provide additional information about the motion and anisotropy of irregularities. In the experiments considered below, the frequency fluctuations of transmitted coherent radio signals were detected. To determine the correlation function for the frequency fluctuations, we should first consider the spatial–temporal spectrum $\Phi(\mathbf{q}, \nu)$ of the phase fluctuations. Similarly to (2) and (3), we can write for this spectrum

$$\Phi(\mathbf{q}, \nu) = A_2\lambda^2\int_0^L P_N(q_x, q_y, q_z = 0, \nu)dz, \quad (12)$$

where $A_2 = const$ and the density-fluctuation spectrum $P_N(\mathbf{q}, \nu)$ is determined by (6). It can easily be shown that, for the model in question, we can express the spatial–temporal correlation function of the phase fluctuations

$$B_\Phi(\rho, \tau) = B^+(\rho, \tau) + B^-(\rho, \tau). \quad (13)$$

Here, the functions $B^\pm(\rho, \tau)$ correspond to waves propagating from and toward the Sun, respectively:

$$B^\pm(\rho, \tau) = B^\pm(\eta^\pm, 0),$$
$$\eta^\pm = [x - (v \pm v_s)\tau]^2 + \mu^2 y^2, \quad (14)$$

where x is the projection of the baseline in the radial direction; y is the baseline projection in the plane of the sky, transverse to $0X$; and τ is a time shift.

The instantaneous frequency of the radio signals is the derivative of the phase φ:

$$\omega = \partial\varphi/\partial t. \quad (15)$$

For this definition, the spatial–temporal spectrum of the frequency fluctuations $\Omega(\mathbf{q}, \nu)$ is related to the phase-fluctuation spectrum (12) by the expression

$$\Omega(\mathbf{q}, \nu) = \nu^2\Phi(\mathbf{q}, \nu). \quad (16)$$

We then obtain for the spatial–temporal correlation function of the frequency fluctuations $K(\rho, \tau)$

$$K(\rho, \tau) = -\partial^2 B_\Phi(\rho, \tau)/\partial\tau^2, \quad (17)$$

where $B_\Phi(\rho, \tau)$ is determined by (13) and (14). We determine the position of the correlation maximum $\tau = \tau_0$ of the function $K(\rho, \tau)$ from the condition $\partial K/\partial\tau = 0$, which, using (13) and (14), yields

$$\{v_1^3(x - v_1\tau_0)[3B_+''(\eta_+) + 2(x - v_1\tau_0)^2 B_+'''(\eta_+)]$$
$$+ v_2^3(x - v_2\tau_0)$$
$$\times [3B_-''(\eta_-) + 2(x - v_2\tau_0)^2 B_-'''(\eta_-)]\} = 0. \quad (18)$$

$$v_1 = v + v_s, \quad v_2 = v - v_s, \quad B''(\eta) = d^2B/d\eta^2,$$
$$B'''(\eta) = d^3B/d\eta^3, \quad \eta = \eta_\pm(\tau_0).$$

In the actual experiments, the temporal frequency variations of the radio signals were measured in a finite fluctuation frequency band ν, with the maximum frequency ν_{max} corresponding to irregularities on scales significantly exceeding the spacing between the receiving points. For this case, the conditions

$$(x - v_{1,2}\tau_0)^2|B'''(\eta_\pm(\tau_0))/B''(\eta_\pm(\tau_0))| \ll 1,$$
$$B_+''(\eta_+(\tau_0)) \approx B_-''(\eta_-(\tau_0)) \approx B_+''(0) \approx B_-(0) \quad (19)$$

can be taken to be satisfied. In accordance with the definition of the rate of change of the frequency fluctuations $V_{dr} = x/\tau_0$, we obtain for V_{dr}, using (18) and (19),

$$V_{dr} = [(v + v_s)^4 + (v - v_s)^4]/[(v + v_s)^3$$
$$+ (v - v_s)^3] = (v^4 + 6v^2v_s^2 + v_s^4)/v(v^2 + 3v_s^2). \quad (20)$$

Expression V_{dr} (20) is independent of the degree of anisotropy μ, as follows from the assumed coincidence of the velocity of the irregularities and the main axis in

which they are extended. For an arbitrary relation between v and v_s, $V_{dr}(20)$ exceeds both the wind speed v and the sound speed v_s. In particular,

$$V_{dr} \approx v(1 + 3v_s^2/v^2) \quad \text{at} \quad v_s \ll v,$$
$$V_{dr} \approx v_s^2/3v \quad \text{at} \quad v_s \gg v. \tag{21}$$

Expression (20) can be generalized for a random velocity distribution:

$$V_{dr} = \langle v^4 \rangle / \langle v^3 \rangle, \tag{22}$$

where $\langle v^4 \rangle$ and $\langle v^3 \rangle$ are the corresponding moments of the velocity distribution.

Expressions (8)–(10) obtained here for the characteristic width of the temporal spectrum of the amplitude fluctuations v_0 and expression (21) for the drift rate of the frequency fluctuations V_{dr} establish relations between these parameters and the velocities and anisotropy of the irregularities. We shall use these relations below to interpret the observations.

3. OBSERVATIONS AND DATA PROCESSING

Simultaneous observations of the amplitude and frequency fluctuations were carried out in May–June 1984 at two ground stations situated near Evpatoriya and Ussuriĭsk during the setting of the *Venera-15* and *Venera-16* spacecraft behind the Sun and their subsequent emergence from behind the solar disk. The measurements were performed at 32 (L band), 8 (C1 band), and 5 cm (C2 band). Since the scintillations are strengthened as the line of sight approaches the Sun, the observational frequency was increased as the impact parameter (distance from the center of the Sun to the line of sight) R decreased, to provide a weak amplitude-fluctuation regime. We monitored the amplitude-scintillation regime by comparing the fluctuations at different frequencies. The temporal energy spectra were calculated from the measured amplitude fluctuations. For each spectrum, we determined the characteristic frequency v_0 and power-law index $p = \alpha - 1$ for the region of high fluctuation frequencies. Then, using this p and the known L and z_0 from formula (8), we calculated V_{ap} using formula (9). The typical values for our measurements yielded $p \approx 2$, corresponding to $\alpha \approx 3$.

Figures 1 and 2 present typical amplitude-fluctuation spectra for the $\lambda = 8$ and 5 cm bands, respectively. During these measurements for May 31, 1984 the line of sight passed at a distance $R = 16.1\ R_s$ from the center of the Sun. For $\lambda = 8$ cm, the scintillation index (relative fluctuation intensity $m = (\langle \Delta I^2 \rangle)^{1/2}/\langle I \rangle$) was $m = 0.35$, while for $\lambda = 5$ cm, $m = 0.22$; i.e., a weak-fluctuation regime was realized in both cases.

The apparent velocity of the irregularities—that is, the rate of change of the diffraction pattern—was deter-
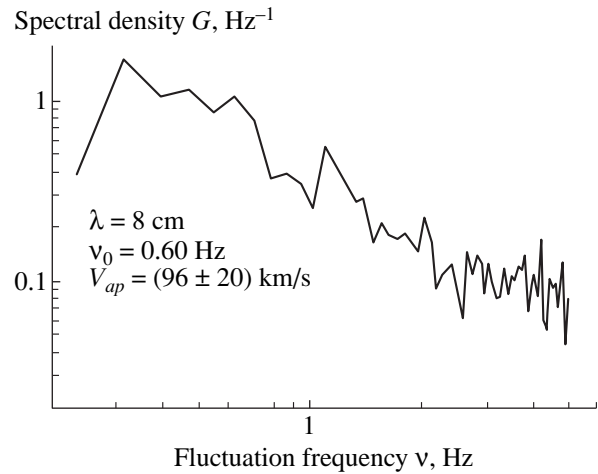

Fig. 1. Normalized amplitude-fluctuation spectrum of radio signals in the $\lambda = 8$ cm band detected on May 31, 1984, at the Evpatoriya ground station. The impact parameter was $R = 16.1 R_s$.
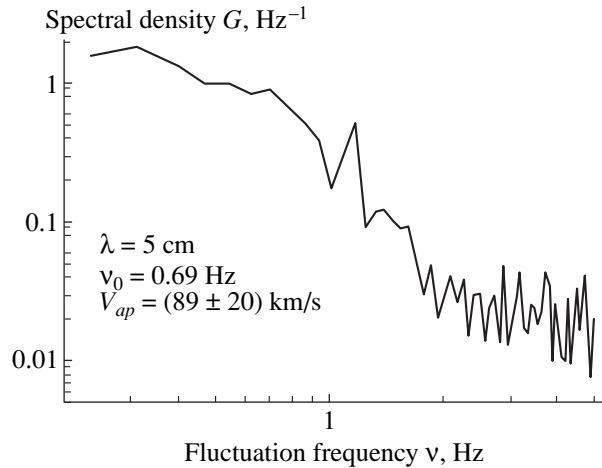

Fig. 2. Same as Fig. 1 for the $\lambda = 5$ cm band.

mined from the bend frequency v_0 of the temporal spectra of the amplitude fluctuations:

$$V_{ap} = b(\alpha) r_F v_0,$$

where r_F is the radius of the first Fresnel zone and $b(\alpha)$ is a numerical coefficient that depends on the spectral index α for the spatial spectrum of the irregularities and varies from 2.22 to 2.56 as α varies from 3.0 to 4.0. The apparent velocities of the irregularities we determined using this technique were (96 ± 20) and (89 ± 20) km/s for the measurements at $\lambda = 8$ and 5 cm, respectively, so that the average velocity was $\langle V_{ap} \rangle = 93 \pm 20$ km/s.

In addition to the amplitude fluctuations, the frequency fluctuations of the radio signals were also measured at the Evpatoriya and Ussuriĭsk stations. The distance between these points is 7700 km, and the radial
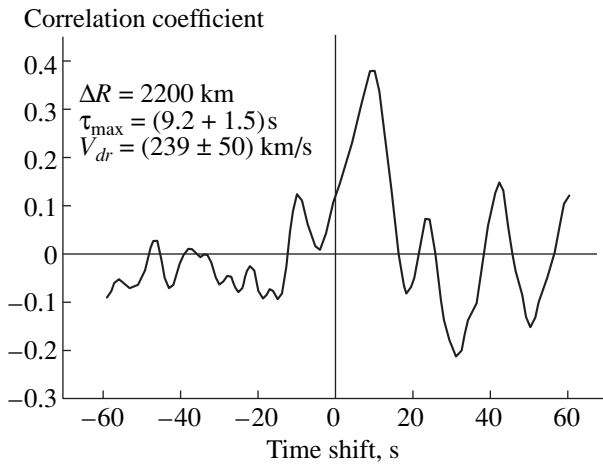
Correlation coefficient

$\Delta R = 2200$ km
$\tau_{\max} = (9.2 + 1.5)$ s
$V_{dr} = (239 \pm 50)$ km/s

Fig. 3. Cross correlation for frequency fluctuations of radio signals in the $\lambda = 32$ cm band detected by the Evpatoriya and Ussuriĭsk ground stations simultaneously with amplitude measurements.
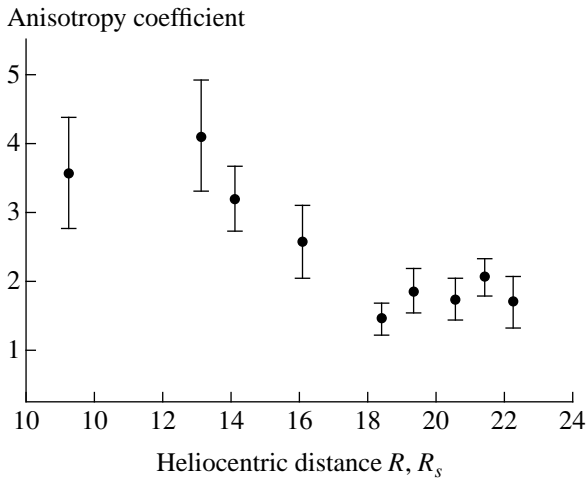
Anisotropy coefficient

Fig. 4. Anisotropy coefficient ξ as a function of heliocentric distance, according to measurements performed in May–July 1984 by the *Venera-15* and *Venera-16* spacecraft.

projection of the baseline vector (radial spacing for the impact points of the lines of sight) was $x \approx 2200$ km. For this spacing of the radio paths, the amplitude fluctuations related to small-scale irregularities (with sizes less than 100 km) become essentially uncorrelated. For this reason, we studied the propagation of the irregularities by performing a correlation analysis of the frequency fluctuations measured simultaneously at the two stations. Figure 3 shows an example of the cross-correlation function of the frequency fluctuations corresponding to the same observation runs as those in Figs. 1 and 2. This figure clearly shows that the correlation maximum is shifted, with the sign of the time delay corresponding to the irregularities moving away from the Sun. The time shift is $\tau_0 = 9.2 \pm 1.5$ s, and the corresponding velocity $V_{dr} =$

$x/\tau_0 = 239 \pm 50$ km/s. The shift of the maximum turns out to be small compared to the characteristic width of the cross-correlation function, verifying the validity of approximation (19).

The results presented in Fig. 4 were obtained over six days in May (25–29 and 31) and three days in June (2, 3, and 7) 1984. The radio signals sounded the outer corona of the Sun westward from the photosphere. During this period, the magnetic field of the Sun exhibited a two-sector structure. Comparison of the radio data with the magnetic-field configuration shows that, from May 25 to 31, the radio signals sounded regions of the outer corona with open magnetic-field lines. On two days (June 2 and 3), the line of sight intersected a heliospheric current sheet. This sheet was situated in a unipolar sector with open field lines on June 7. The available data do not enable us to draw definite conclusions about the dependence of the anisotropy coefficients on the distance to the heliospheric current sheet.

4. INTERPRETATION OF RESULTS

From the measured velocities V_{ap} (amplitude-fluctuation spectrum) and V_{dr} (mutual correlation of the frequency fluctuations), we calculated the dimensionless parameter

$$\xi = V_{dr}/V_{ap}, \qquad (23)$$

which is presented in Fig. 4 for all data for a given run as a function of the heliocentric distance to the line of sight. We can see that the parameter ξ (23) is, on average, close to $\xi = 3$–4 for heliocentric distances $R = 10$–$15R_s$ and decreases to $\xi \leq 2$ for $R > 15R_s$.

Let us consider the data in Fig. 4 in the framework of the turbulence model used above. Substituting into (23) the V_{ap} from (9) with $\alpha = 3$ and the V_{dr} from (20), we find for ξ

$$\xi = \mu(v^4 + 6v^2 v_s^2 + v_s^4)/v(v^2 + 3v_s^2)\left|v^2 - v_s^2\right|^{1/2}. \qquad (24)$$

It follows from (24) that ξ coincides with the anisotropy parameter μ only when $v_s \ll v$, that is, only in a supersonic flow. When $v_s \gg v$, $\xi \gg \mu$. The qualitative relation between ξ and μ will be the same if there is an arbitrary velocity spread. In this case, we can consider v_s to be a measure of the statistical velocity spread leading to chaotic variability of the fluctuation pattern as it drifts across the line of sight. Consequently, the data in Fig. 3 give an upper limit for the anisotropy parameter μ, $\mu \leq \xi$. We can conclude that irregularities on scales 50–100 km are extended in the radial direction, with the degree of extension being comparatively small: $\mu \leq 4$ for $R = 10$–$15R_s$ and $\mu \leq 2$ for $R > 15R_s$.

Ambiguity in estimates of the anisotropy of irregularities and velocity of the solar wind are mainly due to the fact that irregularities with a range of velocities are simultaneously present in the region modulating the

radio signals. The velocity V_{ap} determined by the width of the temporal spectra of the scintillations differs from the velocity v of the solar wind because of both the extension of the irregularities and their motion with respect to the solar-wind plasma. The anisotropy of the irregularities leads to a decrease in V_{ap}, while their proper velocities can lead to either an increase or a decrease in V_{ap} relative to the solar-wind velocity v (depending on the difference between v and v_s). The velocity V_{dr} determined by the time delay of the fluctuation pattern between the observation points differs from v only due to the motions of the irregularities, with V_{dr} always exceeding v and v_s. Since the ratio v_s/v increases, the excess of V_{dr} over v also increases when the line of sight approaches the Sun. Our data qualitatively agree with this expectation, since, as a rule, V_{ap} is smaller than V_{dr} by a factor of a few.

By virtue of the reasons noted above, our data remain insufficient for a unique determination of the velocities v and v_s and the anisotropy parameter μ. The $\xi(R)$ dependence in Fig. 4 admits two possible interpretations. If we suppose that the flow at $R > 10R_s$ is strongly supersonic, i.e., $v \gg v_s$, the decrease in ξ at $R \approx 15R_s$ will be due to a decrease in the anisotropy of the irregularities from $\mu \approx 4$ to $\mu \leq 2$. One difficulty of this interpretation is the lack of sufficiently plausible physical origins for the radical change in the turbulence if the regular flow has already formed. The second interpretation suggests that the anisotropy μ of the irregularities in the considered R interval is small ($\mu \leq 2$), so that changes in ξ are attributed to a decrease in the ratio v_s/v from $v_s/v \geq 1$ at $R < 15R_s$ to $v_s/v < 1$ at $R > 15R_s$. Since the measured ξ is not very high, the ratio v_s/v for $R = 10$–$15R_s$ should not differ much from unity. Here, ξ coincides with the true anisotropy μ of the irregularities only for $R > 15 R_s$.

This second interpretation is preferable, since it is also consistent with other data obtained by radio-sounding methods. For example, the measured correlation between the Doppler fluctuations of radio signals in paths between the Earth and the *Ulysses* spacecraft shows that the velocities of irregularities are comparatively small for $R \leq 10R_s$, so that $v \approx 100$–150 km/s, and increase to $v \approx 400$ km/s for $R > 20R_s$ [8]. In addition, according to the radio-interferometric measurements of [1], the anisotropy of irregularities on scales ≤ 35 km (close to the scales probed by our scintillation data) decreases to $\mu \leq 2$ for $R \approx 6R_s$, i.e., for a region closer to the Sun than the region $R > 10R_s$ with which we are dealing here. The estimate $\mu \leq 2$ is in good agreement with the data of [9], where μ was estimated for $R > 10R_s$ based on the best agreement between model spatial turbulence spectra and temporal amplitude-scintillation spectra of natural cosmic radio sources. In addition, it follows from the radio-interferometric data of [10] that, for irregularities on scales smaller than 100 km, $\mu \leq 2$ for $R > 10R_s$.

5. CONCLUSIONS

Based on the results obtained, we argue that the solar-wind velocity does not exceed the local sound speed at distances smaller than $10R_s$ and the transition to a supersonic regime occurs at $R = 10$–$15R_s$. A similar estimate was obtained earlier [3] by analyzing the characteristic widths of the temporal spectra of amplitude fluctuations. Since the *Venera-15* and *Venera-16* radio signals probed a region near the solar equator, strictly speaking, our conclusions about solar-plasma motions are relevant only for a slow solar wind at the minimum of solar activity.

The large distance of the critical surface of the supersonic transition provides evidence for a significant contribution from additional, noncoronal sources of energy and momentum and imposes substantial restrictions on possible models for formation of the solar wind. These additional sources are apparently associated with low-frequency Alfvén waves [11], to which the corona is transparent, so that they can supply the solar-wind plasma with energy at rather large distances from the Sun. Alfvén waves with amplitudes sufficient to accelerate the solar wind were detected in the solar plasma environment from fluctuations of the Faraday rotation of polarized radio signals transmitted through this plasma [2].

The anisotropy of the irregularities and its radial variation testify to the important role of magnetic fields in the formation and evolution of the turbulence and in the formation of the flow itself. In particular, the decrease in the degree of anisotropy of small-scale irregularities from $\mu \approx 10$ at $R < 10R_s$ to $\mu \leq 2$ at $R > 10R_s$ indicates that the turbulence regimes in the subsonic and supersonic flows differ considerably. This difference could be associated both with the development of an isotropic angular distribution for slow magnetoacoustic waves and with an increase in the relative contribution of rapid magnetoacoustic waves to small-scale plasma-density fluctuations in the transition from inner regions to the fully formed flow.

Our study shows clear promise for the simultaneous application of various radio-probing methods. In particular, one quite interesting course of investigation is studies of the velocities and anisotropy of irregularities in the solar-wind formation region at high heliolatitudes at various phases of the solar cycle.

REFERENCES

1. J. W. Armstrong, W. A. Coles, M. Kojima, and B. J. Rickett, Astrophys. J., Part 1 **358**, 685 (1990).

2. V. E. Andreev, M. Bird, A. I. Efimov, *et al.*, Astron. Zh. **74**, 263 (1997) [Astron. Rep. **41**, 227 (1997)].

3. A. I. Efimov, I. V. Chasheĭ, V. I. Shishov, and O. I. Yakovlev, Kosm. Issled. **28**, 581 (1990).

4. I. V. Chasheĭ and V. I. Shishov, Astron. Zh. **60**, 594 (1983) [Sov. Astron. **27**, 346 (1983)].

5. A. I. Efimov, Space Sci. Rev. **70**, 397 (1994).

6. E. Antonucci, *A Crossroads for European Solar and Future Missions Possibilities, Proc. ESA, IAC Conf. Puerto de la Cruz Canary Islands*, Ed. by E. R. Priest *et al.*, ESA SP-417 (1998).

7. L. M. Erukhimov, N. V. Murav'eva, and E. N. Myasnikov, Pis'ma Astron. Zh. **16**, 1118 (1990) [Sov. Astron. Lett. **16**, 481 (1990)].

8. R. Wohlmuth, D. Plettemeier, P. Edenhofer, *et al.*, Radio Sci. **32**, 617 (1997).

9. Y. Yamauchi, M. Tokumaru, M. Kojima, *et al.*, J. Geophys. Res. A **103**, 6571 (1998).

10. R. R. Grall, W. A. Coles, S. R. Spangler, *et al.*, J. Geophys. Res. A **102**, 263 (1997).

11. I. V. Chasheĭ and V. I. Shishov, Astron. Zh. **65**, 157 (1988) [Sov. Astron. **32**, 81 (1988)].

Translated by V. Badin